ABSTRACT

Title of dissertation: ONE-DIMENSIONAL ANALYTICAL MODEL DEVELOPMENT OF A PLASMA-BASED ACTUATOR

Sarah Haack Popkin, Doctor of Philosophy, 2014

Dissertation directed by: Professor Alison Flatau
Department of Aerospace Engineering

This dissertation provides a method for modeling the complex, multi-physics, multi-dimensional processes associated with a plasma-based flow control actuator, also known as the SparkJet, by using a one-dimensional analytical model derived from the Euler and thermodynamic equations, under varying assumptions. This model is compared to CFD simulations and experimental data to verify and/or modify the model where simplifying assumptions poorly represent the real actuator. The model was exercised to explore high-frequency actuation and methods of improving actuator performance. Using peak jet momentum as a performance metric, the model shows that a typical SparkJet design (1 mm orifice diameter, 84.8 mm^3 cavity volume and 0.5 J energy input) operated over a range of frequencies from 1 Hz to 10 kHz shows a decrease in peak momentum corresponding to an actuation cutoff frequency of 800 Hz. The model results show that the cutoff frequency is primarily a function of orifice diameter and cavity volume.

To further verify model accuracy, experimental testing was performed involv-

ing time-dependent, cavity pressure and arc power measurements as a function of orifice diameter, cavity volume, input energy and electrode gap. The cavity pressure measurements showed that pressure-based efficiency ranges from 20% to 40%. The arc power measurements exposed the deficiency in assuming instantaneous energy deposition and a calorically perfect gas and also showed that arc efficiency was approximately 80%. Additional comparisons between the pressure-based modeling and experimental results show that the model captures the actuator dependence on orifice diameter, cavity volume, and input energy but over-estimates the duration of the jet flow during Stage 2. The likely cause of the disagreement is an inaccurate representation of thermal heat transfer related to convective heat transfer or heat loss to the electrodes.

ONE-DIMENSIONAL ANALYTICAL MODEL DEVELOPMENT OF A PLASMA-BASED ACTUATOR

by

Sarah Haack Popkin

Dissertation submitted to the Faculty of the Graduate School of the
University of Maryland, College Park in partial fulfillment
of the requirements for the degree of
Doctor of Philosophy
2014

Advisory Committee:
Professor Alison Flatau, Chair/Advisor
Professor James Baeder
Professor Christopher Cadou
Professor Dianne O'Leary
Professor Norman Wereley

Dedication

To my past, present and future family.

Acknowledgments

I owe my deepest gratitude to all the people who have made this dissertation possible. My relationship with my advisor, Dr. Flatau, was established more than 10 years ago and I had no idea how valuable that relationship would be. Thank you, Dr. Flatau, for always being my advocate and guiding me through both my Master's and PhD and reading and editing both my thesis and this dissertation! I would also like to thank the committee members for helping finalize this dissertation to be a truly beneficial body of work for the flow control community. This work has been financially supported by AFOSR under supervision of Drs. John Schmisseur and Doug Smith through JHU/APL. Without the AFOSR support, accomplishment of this research would have been much more difficult. I would also like to thank PCB for helping me find the right pressure sensor for my volatile application and understand the techniques for protecting it in the high-temperature environment.

At JHU/APL, several people have been involved with this project. I am very grateful for the support and technical advice from Bo Cybyk, Bruce Land, Trent Taylor, John Teehan and Dave VanWie. These colleagues have helped guide the SparkJet research and helped me understand the broader picture in the field of arcs, sparks, and plasma. Bruce, I would especially like to thank you for all of the extra hours you spent designing the SparkJet circuitry and making sure I stayed safe around high voltages and high current. Bo, I would also like to thank you for acting as my advisor at JHU/APL and advocating my efforts to pursue this dissertation.

I would like to thank my colleagues at JHU/APL who have helped me along

the way providing technical and friendly advice for the last six years. In addition, pursuing this dissertation would have been impossible without the encouragement from my supervisors despite working full-time at JHU/APL. To my family and friends, thank you for never doubting my abilities and always asking me how I was doing to let me know you were thinking of me.

Finally, to my husband, Russell Popkin. I am so grateful that you put up with me despite the hundreds of hours spent away from you and the tears of frustration and doubt. In my times of need, I had you there to steer me in the right direction but also let me know you supported whichever direction I chose. I am so lucky to have you by my side.

Contents

List of Tables

List of Figures

Nomenclature

α	thermal diffusivity (m^2/s)
β	phase constant between the vortex shedding and the aoustic wave response in the cavity (unitless)
γ	ratio of specific heats (unitless)
η	efficiency (unitless)
ρ	density (kg/m^3)
ω	frequency (rad/s)
A	area (m^2)
Bi	Biot number (unitless)
C	capacitance (F)
C_v	specific heat for a constant volume (J/kgK)
C_p	specific heat for a constant volume (J/kgK)
d	diameter (m)
D	depth (m)
e	internal energy per unit mass (J/kg)
E	internal energy (J)
f	frequency (Hz)
h	convective heat transfer coefficient (W/m^2K)
H	height (m)
I	electric current (A)
k	thermal conductivity (W/mK)
K	ratio of vortex convection speed to freestream flow speed (unitless)
L	length (m)
m	mass (kg)
M	Mach number
n	mode number (unitless)
P	pressure (Pa)
P_0	total pressure (Pa)
q	input power (J/s)
Q	input energy (J)
r	radius (m)
R	specific gas constant (J/kgK)
t	time (s)
T	temperature (K)
U	velocity (m/s)
v	cavity volume (m^3)
v	orifice volume (m^3)
V	voltage (V)

Subscripts

∞	freestream condition
1	Conditions at the beginning of Stage 1
2	Conditions at the beginning of Stage 2
A	arc
c	cutoff
C	capacitance
e	exit
i	spatial discretization
j	temporal discretization
m	measured
M	Macor
n	notional
o	orifice
p	calorically perfect
P	pressure
T	thermally perfect
W	tungsten

Acronymns

600ET	600 V electrode voltage initiated with an external trigger
600PST	600 V electrode voltage initiated with a pseudo-series trigger
AFC	Active Flow Control
AFOSR	Air Force Office of Scientific Research
CFD	Computational Fluid Dynamics
COMPACT	Combustion Powered Actuator
DBD	Dielectric Barrier Discharge
DST	Digital Speckle Tomography
EMI	Electromagnetic Interference
FFT	Fast-Fourier Transform
FSU/AAPL	Florida State University Advanced Aero-Propulsion Laboratory
JHU/APL	Johns Hopkins University Applied Physics Laboratory
LAFPA	Localized Arc Filament Plasma Actuator
MHD	Magnetohydrodynamic
NASA	National Aeronautics and Space Administration
ONERA	Office National d'Etudes et de Recherches Arospatiales
PIV	Particle Image Velocimetry
REM	Resonance Enhanced Microjets
URANS	Unsteady Reynolds-Averaged Navier-Stokes
V/STOL	Vertical and/or Short Takeoff and Landing
ZNMF	Zero-net-mass-flux

Chapter 1

Introduction

The ability to ensure safe separation of a weapon from the weapons bay of a supersonic jet or reduce damaging noise from a jet engine exhaust depends on our ability to properly control the high-speed flow environment. Controlling a large-scale, high-speed flow environment requires a flow control device or array of flow control devices which can influence a large area and have the requisite control authority to manipulate high-momentum flow. The motivation for this work and any flow control work is to develop, characterize, and understand an actuator capable of improving otherwise adverse flow conditions. Specifically, this work attempts to develop a simplified, one-dimensional model of a flow control actuator, the Spark-Jet, capable of controlling high-speed flows. This model would enable simple and fast design optimization of an array of devices specifically tailored to an application such as controlling a jet exhaust or the shear layer over an open weapons bay. To provide an understanding of the flow control applications where a high-momentum flow control device would be required, the following sections describe a few of these applications. Following a description of the applications, the devices and methods of flow control for the previously mentioned applications are described.

1.1 High-Speed Flow Control Applications

The flow control challenges unique to high speed applications are primarily related to the momentum and frequency requirements. These high-speed flow applications possess high-momentum, high-frequency instabilities within the boundary layer. Before considering the appropriate flow control device and technique to efficiently control flow, the details of each flow condition need to be understood. The following sections describe some of the primary applications of interest for high-speed flow control and the details useful for applying the ideal flow control technique.

1.1.1 Flow Separation

A common flow phenomenon of concern is flow separation which adversely affects aircraft performance at low and high speeds. Over an airfoil, for example, flow is considered attached when the flow near the wall, the boundary layer, is moving in the same direction as the freestream. Flow separation occurs when an adverse pressure gradient exists along a surfaces and causes the flow to lose momentum in the boundary layer and eventually reverse direction. The adverse pressure gradient can exist for a variety of reasons including a surface contour away from the freestream, a normal shock on a transonic airfoil (Figure 1.1) or shock wave boundary layer interaction between a reflected oblique shock and a boundary layer. Flow separation is generally associated with increased drag or a loss of lift in all flows or a reattachment zone that can lead to increased heat transfer to the surface in supersonic and hypersonic flows.

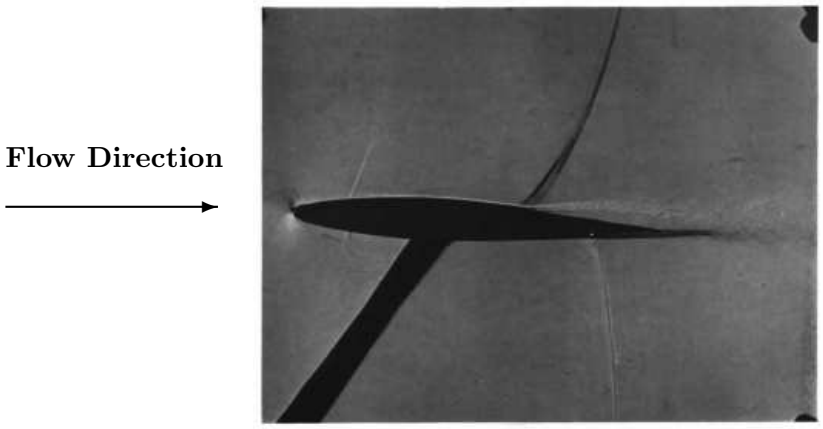

Figure 1.1: Schlieren image of shock-induced flow separation on the upper surface of an airfoil in transonic flow [1].

1.1.2 Boundary Layer Transition

Boundary layer transition is the process describing the transformation of a boundary layer from laminar to turbulent. Boundary layer transition is caused by the growth of particular instabilities in the flow near the surface. The instabilities can exist due to surface roughness, surface features, or simply the natural growth of the boundary layer. Figure 1.2 is a sketch from Schlichting [2] describing the series of instabilities that transform laminar flow to fully turbulent flow. The differences between laminar and turbulent boundary layer flow make each type desirable or undesirable. For example, the skin friction drag associated with laminar flow is lower than with turbulent flow. However, laminar flow is more susceptible to flow separation than turbulent flow because it can be influenced more easily by an adverse pressure gradient or surface features. Therefore, both inducing or delaying boundary layer transition are potential goals of flow control.

More advanced studies of boundary layer transition reveal a unique differ-

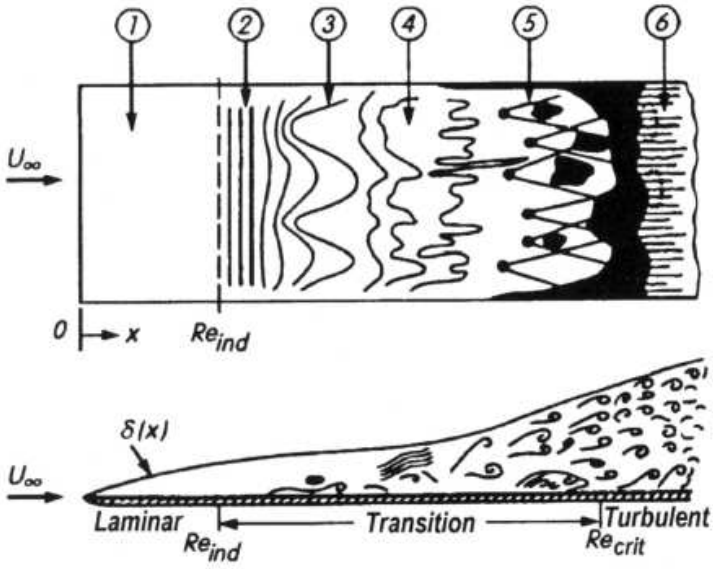

Figure 1.2: Sketch of flow over a flat plate through transition from a laminar to turbulent boundary layer. The regions of flow from 1-6 are 1) stable laminar flow, 2) unstable Tollmien-Schlichting waves, 3) three-dimensional waves and vortex formation (Λ-structures), 4) vortex decay, 5) formation of turbulent spots, and 6) fully turbulent flow, respectively [2].

ence between boundary layer development over two-dimensional, flat surfaces and three-dimensional, curved surfaces. The surface curvature allows centrifugal forces to create vortical motion within the boundary layer that introduce so-called Taylor-Görtler instabilities. These instabilities are considered *primary* and also include *secondary* instabilities each of which occur at separate frequencies. When applying flow control techniques, all modes of instability can prompt transition. Therefore, the ideal flow control technique would prevent one type of instability without perturbing another type of instability. The instability responsible for transition is also a function of velocity. For example, for Mach less than approximately four, Tollmein-Schlichting instability growth rate dominates transition. However, for Mach greater than four, the instability growth rate of higher frequency Mack modes dominate transition [3]. Such dependence on velocity requires an actuator capable of tuning the actuation frequency to the immediate flow conditions.

1.1.3 Supersonic Open Cavity Flow

Since the beginning of this dissertation research, the primary flow control application of interest has been control of supersonic open cavity flow. An example of when this type of flow condition can occur includes an aircraft flying at supersonic velocities with open bomb bay doors. Figure 1.3 shows an F-22 Raptor with open bomb bay doors and reveals the internal geometry the flow encounters when opened. Analysis of this flow field is based on a simplified representation of the open cavity with a characteristic length to depth ratio, (L/D). The primary feature of the open

Figure 1.3: F-22 Raptor flying with open bomb bay doors [5].

cavity flow is a self-sustaining, unsteady flow inside the cavity with a characteristic frequency or frequencies based on L/D and Mach. The unsteady nature of the flow can prevent reliable store separation or accelerate aircraft structural fatigue and, thus, methods of reducing the unsteadiness are desired. As a result of wind tunnel testing, the frequency, or *tone*, associated with cavity flow was first identified by Rossiter [4] and is, subsequently, known as a Rossiter tone.

The targeted cavity geometry is characterized by an L/D of 5.6 in a Mach 1.5 flow. Following Rossiter's work, Heller [6] determined that the cavity speed of sound is actually equal to the freestream stagnation speed of sound. Therefore, the frequency of the cavity tones is predicted by

$$f = \frac{U}{L}\frac{(n-\beta)}{\left(\frac{1}{K}+\frac{M}{\sqrt{1+\frac{\gamma-1}{2}M^2}}\right)} \tag{1.1}$$

and is commonly referred to in recent open cavity research. Using Equation 1.1 with $K = 0.57$ and $\beta = 0.25$, the 1st, 2nd and 3rd modes for the targeted cavity

geometry are 0.84, 1.69 and 2.53 kHz, respectively. Here, both passive and active flow control (AFC) techniques have been applied and their ability to suppress these tones is summarized in Section 1.2.

1.1.4 Jet Impingement / Jet Noise

Jet noise is the audible pressure unsteadiness that develops in a free or impinging jet. Subsonic jet noise is characterized by aperiodic bursts of noise that are hypothesized to be linked to large scale structures developing in the jet itself. A noise event is identified when the instantaneous pressure exceeds 1.5 times the root mean square (RMS) pressure. However, generation of these noise events is not well understood and attempts to understand them are primarily experimental [7, 8, 9]. As a result, without adequate understanding of the flow field, flow control techniques have not yet been applied. In supersonic jets, however, free and impinging jets exhibit both broadband and highly periodic noise. Both types of jet noise are undesirable. Far-field noise suppression is required near humans and animals. Near-field noise suppression is required to reduce the potential for structural fatigue associated with jet impingement. The mechanism behind the noise generation is similar for both broadband and tonal noise. A feedback loop consisting of disturbances emanating from the nozzle lip which interfere with the shock-cell structure create acoustic waves that propagate upstream. Once the acoustic waves interact with the receptive disturbances at the nozzle lip, the feedback loop is complete. Screech tones occur when the feedback loop frequency matches the fundamental screech frequency

[10]. Another noise generation mechanism is interaction of convective turbulence structures passing through a standing shock structure in a supersonic jet [11].

An impinging jet is similar to a free jet except that the jet interacts with a solid surface that is situated relatively close to the nozzle exit. This scenario is commonly encountered on V/STOL (vertical and/or short take-off and landing) aircraft during takeoff or landing. The noise associated with a supersonic impinging jet is also broadband with a tonal component but at a higher noise level [12]. The broadband noise is generated by eddies within the shear layer moving at supersonic velocities. The tones associated with an impinging jet are called impingement tones and the frequency of such tones are depending on the ratio of nozzle diameter to distance from the solid surface. Similar to the free jet case, the tones emerge from an acoustic feedback loop involving disturbances within the shear layer which create acoustic waves that travel upstream toward the receptive area of the shear layer near the nozzle lip. However, the proximity of a solid wall causes these disturbances to create acoustic waves at a higher intensity than a free jet. Flow control techniques have been applied to both free jet and impinging jet flows primarily targeting the receptive shear layer. The devices and exact techniques are described in Section 1.2.

The variety of adverse flow phenomenon described in this section does not encompass all areas where flow control can be used but represent the majority of the flow phenomenon targeted by high-speed flow control studies. The following section describes the flow control devices used to affect these flows and how they have been applied to the flow phenomenon described in this section.

1.2 High-Momentum Flow Control Actuators

In the broadest sense, all flow control devices can be categorized as either passive or active devices. *Passive* devices include fences, ridges, bumps, thermal bumps, or other built-in surface modifications that are designed to benefit an adverse flow feature at specific, on-design flow conditions. These devices are useful in volatile flow environments where flow enhancement is desired, but moving parts would likely fail, and weight or power requirements would not allow an active device. However, these devices can contribute to a performance penalty at off-design flow conditions. To eliminate the drag penalty associated with passive devices, a wide variety of *active* flow control devices have also been developed. For high-speed flow, these tend to involve, high-momentum jets or rapid energy deposition using arcs, plasma and magnetic fields. Devices that use rapid energy deposition include the combustion powered actuator (COMPACT), magneto-hydrodynamic (MHD) actuators, nanosecond dielectric barrier discharge (DBD) actuators, and localized arc filament plasma actuators (LAFPAs). High-momentum fluidic devices include synthetic jet actuators, microjet actuators, and resonance enhanced microjet (REM) actuators. This section focuses on the flow control devices (including references) and techniques applied to high-speed flows.

1.2.1 Passive Flow Control

Probably the most commonly used, tested, and modeled passive flow control device is the vortex generator. A vortex generator is any device that creates a

streamwise vortex near a flow surface with the primary intention of delaying or preventing flow separation. Most people have seen passive vortex generators on the upper surface of commercial aircraft wings in the form of metal rectangular tabs. This kind of vortex generator can be parallel to the flow or at a slight angle to the flow and an array of vortex generators are employed to affect a larger area of flow such as the entire span of a wing. The resulting vortices introduce high kinetic energy air into a lower kinetic energy boundary layer that usually results in laminar to turbulent flow transition and delayed or eliminated flow separation. In fact, controlling flow separation is the primary use of vortex generators. Vortex generator placement is just upstream of a potential flow separation location to ensure attached flow throughout the entire flow field. As previously mentioned, vortex generators are typically used on wings, and they are the most beneficial when the wings are at a high angle of attack when flow separation is prevalent. Vortex generators are also used in inlets where the incoming flow interacts with a highly curved transition area from the inlet to the compressor.

Figure 1.4 demonstrates the beneficial effect of using vortex generators to prevent flow separation in a supersonic inlet. Figure 1.4(a) shows a picture of the vortex generators; in this case, they are designed to be used in pairs and there is an array of three pairs that spans the wind tunnel test section. Figure 1.4(b) illustrates a large separated flow region that forms over the ramp using oil flow visualization. The flow separation is eliminated with the use of vortex generators as shown in Figure 1.4(c).

For controlling boundary layer transition, surface modifications are typically used. The surface modifications are tailored to the natural boundary layer instabil-

ities that lead to transition as shown in Figure 1.2. Research conducted by Rasheed et al. [14] evaluated the ability of surface porosity to affect transition in Mach 5 nitrogen and carbon dioxide flows. These holes, shown in Figure 1.5(a), cover a 5.06° sharp cone in a Mach 5 flow where the Mack mode dominates transition. This flow control scheme directly targets the Mack mode instability via controlled spacing between the holes. Through a comparison of schlieren images (Figure 1.5(b)) and heat transfer measurements over a smooth surface and a porous surface, the porosity clearly delayed transition.

Another type of passive flow control that is used against high-speed flow applications is fences, ridges or any other physical modification to the leading edge of an open cavity flow. Passive devices are commonly used on subsonic cavity flow but a collection of such devices were tested against *supersonic* open cavity flow by Schmit et al. [15]. Four types of passive flow control devices (spoiler, 3D backward step, ridges and a rod) were installed just upstream of the open cavity. Results showed that the rod was most effective at reducing flow unsteadiness in the cavity because the natural shedding from the rod disturbs the formation of large vortical structures. The authors concluded that while these devices generated flow improvements, the physical design should be tuned to the specific cavity flow conditions.

Contouring of jet nozzles is another passive flow control technique used to reduce jet noise. As described earlier, jet noise is caused by feedback from acoustic waves to the shear layer near the nozzle exit. Therefore, contouring the nozzle exit can be effective in reducing the feedback. This phenomenon was experimentally demonstrated in work by Andre et al. [10] by reducing the amplitude of screech

tones. Figure 1.6(b) clearly shows that using a notched nozzle exit for Mach 1.35 reduces, if not eliminates, the screech tones where the black line shows the sound pressure level (SPL) associated with the clean nozzle and the grey line shows the SPL associated with the notched nozzle.

1.2.2 Active Flow Control

Active flow control devices are another technique designed to improve otherwise adverse flow phenomenon without physically modifying the aerodynamic surface. In fact, the use of active flow control is sometimes referred to as *virtual shaping* [16, 17, 18, 19]. The most basic forms of active flow control involve steady blowing, steady suction, or unsteady blowing and suction. These techniques are typically used to control the thickness of the boundary layer and delay flow separation. A disadvantage to operating steady suction or blowing devices is the requirement of an external air supply or a vacuum chamber. Unsteady devices that draw on the external flow environment and eliminate the need for an external air supply are called zero-net-mass-flux (ZNMF) devices.

Applied specifically to high-speed flows, an actuator called a microjet has been utilized for both supersonic open cavity flow and impinging jet noise. Microjets, developed by Florida State University, are steady jets supplied with high pressure air. When arranged in an array, a single supply pressurizes a chamber and forces air through multiple orifices. Microjets have been applied to two high-speed applications: open cavity flow and jet noise. To control noise and the unsteady shear layer

motion associated with a supersonic open cavity, an array of 12 microjets with a 0.4 mm orifice diameter were placed at the leading edge of the cavity [20]. The aspect ratio of the cavity is $L/D = 5.16$ and $L/W = 5.92$ in a Mach 2.0 crossflow. Using shadowgraph, particle image velocimetry (PIV), and unsteady acoustic pressure measurements, the effect of microjets over a range of nozzle pressure ratios, results demonstrated the ability of the microjets to reduce broadband noise up to 9 dB and tonal noise up to 20 dB.

While reducing noise levels is beneficial, another purpose of controlling supersonic cavity unsteadiness is to ensure safe store separation. To that end, wind tunnel tests were conducted to determine the efficacy of microjets creating a flow environment suitable for store separation. As part of the High Frequency Excitation (HIFEX) program funded by the Defense Advanced Research Projects Agency (DARPA), wind tunnel testing was conducted to evaluate the effectiveness of microjets on a cavity flow field in Mach 2.5 flow [21]. The microjet array consisted of two rows of 150 supersonic ($M = 2.2$) jets. The upstream array operated at a momentum coefficient, C_μ, of 0.26 and the downstream array was operated at C_μ of 0.18. The results of this study showed that the microjet arrays in conjunction with a jet screen upstream of the microjet array provided the best control using the least mass flow. The combination of flow control techniques is considered a *tandem array* and was used to control store separation on a full-scale test at the high-speed track at Hollomon Air Force Base [22]. The full-scale test confirmed that safe store separation could be achieved at Mach 2 with the use of active flow control.

Combining both suction and blowing, the synthetic jet actuator is another

heavily used active flow control device also intended to control flow separation. The synthetic jet actuator is probably the earliest, most heavily tested, modeled, and characterized unsteady flow control device. A review of synthetic jets published in 2002 [23] summarizes numerous studies toward characterizing and applying synthetic jets to a wide variety of non-ideal flow conditions. The synthetic jets described are created by physical changes to the cavity volume to force air in and out of an orifice.

Synthetic jets, also known as vortex generator jets, are unsteady jets oscillating between blowing and suction at a prescribed frequency depending on the flow environment instabilities. With no external air supply, these devices are considered a ZNMF device. During the blowing phase, fluid forced through an orifice creates a jet with a vortex pair at the jet front. This vortex pair causes high momentum fluid in the freestream to interact with a lower momentum boundary layer that energizes the boundary layer leading to flow separation control. During the suction phase, the local low-momentum boundary layer fluid is removed from the surface above the synthetic jet orifice that also helps control separation and transition. Because these synthetic jets are mechanically created, they are limited in the ability to produce simultaneous high-frequency and high-momentum throughput. Therefore, other methods of creating an unsteady jet for high-speed applications have been developed.

REMs were derived from microjets but operate with an inherent unsteadiness to target natural unsteadiness in a flowfield. The REM design consists of a high pressure air supply issuing through a 1 mm diameter nozzle into a cavity with ad-

justable height and diameter to produce a desired frequency. Opposite the 1 mm nozzle, the fluid ejected into the cavity is passed through an array of orifices typically 0.4 mm in diameter. Figure 1.7(a) shows a sketch of the basic REM design with the critical sizing parameters indicated. Development of REMs is fairly recent but application oriented experimental tests have demonstrated the ability of the REMs to produce an unsteady influence on Mach 1.5 flow over a flat plate [24] and reduce overall and impingement tone noise levels [25, 26].

Another type of high-momentum flow control device is called a COMPACT, developed by Georgia Institute of Technology, which uses a small combustion process inside a chamber which ejects high-speed air through an orifice. This device ignites a mixture of air and hydrogen with a spark to increase cavity pressure (see Figure 1.8) [28]. Using a passive valve, the fuel and oxidizer flow into the cavity once the cavity pressure drops below the supply pressure. Peak cavity pressure is achieved between 1 and 3 ms after combustion is initiated and a cycle completes in approximately 4-10 ms depending on the design parameters.

The COMPACT has been used successfully to delay flow separation over a 2-D airfoil [29] and a 3-D rotorcraft fuselage [30]. To control flow separation over an airfoil, the COMPACTs were placed at 20% chord length from the leading edge. The orifice shape was rectangular with the largest dimension being spanwise and the resulting jets were normal to the airfoil surface. The study demonstrated the transient effect of a single pulse from the array of COMPACTs where the flow became momentarily attached for a duration of 8-10 convective time scales after the COMPACT was initiated. For flow separation control on the generic, ROBIN (Ro-

tor Body Interaction) fuselage, several arrays of COMPACTs were arranged on the lower surface of the transition section between the fuselage cabin and the tail boom. Again, the orifices were rectangular and oriented in the spanwise direction but the jets were configured to eject either normal or tangential to the flow surface. The COMPACT arrays successfully reduced flow separation such that the drag coefficient was reduced between 12% and 17%.

The active flow control devices described so far have involved a fluidic jet produced by a pressurized chamber of some sort. There are several techniques that involve installing a device directly on the surface of a body or depositing energy very near the surface of the body. A different type of actuation technique is the use of electromagnetic fields to produce fluid motion. For very low-speeds, a DBD actuator has been tested for multiple applications. A review of the device and the multitude of experimental and computational studies are summarized in a review by Corke et al. [31]. Since classic DBD actuators introduce only a small amount of momentum and are limited to low-speed applications, they are not discussed here in great detail. However, by actuating the DBD actuators with a nanosecond wide pulse, the actuator produces a blast wave and can affect high-momentum flows. Specifically, the nanosecond DBDs have delayed prevented flow separation over airfoils in transonic flows as demonstrated in Figure 1.9 [32].

A LAFPA involves a sudden energy deposition in the form of an arc discharge between two electrodes. The arc discharge produces significant heat via Joule heating that results in a blast wave and local heat addition to the flow [33]. This device is similar to the SparkJet except that the LAFPA arc is not enclosed in a cavity

but rather open to the flow and recessed in a groove to shield the arcs from the high-speed flow [34]. The electronics that support LAFPA actuation use a ramped voltage up to 10 kV which creates an arc that is sustained by up to 0.25 A when an array of eight LAFPAs are in use. LAFPAs have been primarily applied to jet noise mitigation [35] and high-speed jet control [36] but also to shock wave boundary layer interaction control for supersonic inlets [37].

Another unique type of flow control is through the use of MHD flow control. This type of actuation relies on the presence of a volume of ionized gas on which a magnetic field can apply a force. There are many challenges associated with MHD control including producing an ionized gas with sufficient volume and charge density while producing a strong enough magnetic field to achieve the needed Lorenz force to change the momentum of a moving fluid. Therefore, there are several computational MHD studies, but experimental studies are lacking in number and variety. An excellent summary of the challenges associated with MHD testing has been compiled by Braun [38]. Braun also conducted experimental studies using an MHD actuator array but applied to a low speed (6 - 25.6 m/s) boundary layer flow over a flat plate. The MHD actuator array did indeed affect the boundary layer profile beneficially but the energy consumed and mass of the power supplies would make this technique prohibitive on an aerospace vehicle. A recent experimental test studied the ability to control boundary layer transition in a Mach 3 flow [39].

The SparkJet actuator shares some commonalities with the above mentioned active flow control devices. Specifically, the SparkJet uses an arc discharge similar to the LAFPA actuator, it produces a fluidic jet similar to the microjets, and it pro-

duces an unsteady jet similar to a synthetic jet. However, no single device shares the same characteristics of the SparkJet such that the SparkJet represents a unique device with the ability to provide a unique input to high-speed flow applications.

1.3 Dissertation Goals

This chapter presented the need and requirements for high-speed flow control and the devices attempting to fulfill those needs. This dissertation introduces an actuator, the SparkJet, capable of fulfilling several high-speed flow control needs with the unique ability to produce simultaneous high-frequency and high-momentum jet flow. The primary goal of this dissertation is to contribute a powerful, yet simple, numerical model of the SparkJet actuator supported by experimental measurement and prior existing CFD modeling. Previous work toward understanding the SparkJet experimentally and numerically are described in Chapter 2. The modeling efforts described in Chapter 3 are used to understand how various design parameters affect actuator performance during a single actuation cycle and while operating at high frequency. The modeling results are supported through experimental testing described in Chapters 4 through 6 where current and voltage measurements are used to determine power draw from the SparkJet. Internal cavity pressure measurements were collected to determine the amount of useful energy produced by the arc discharge. Analysis of these results are used to determine any inefficiencies associated with the SparkJet actuation process and support adjustments to the numerical model to capture these inefficiencies.

(a) Picture of vortex generators.

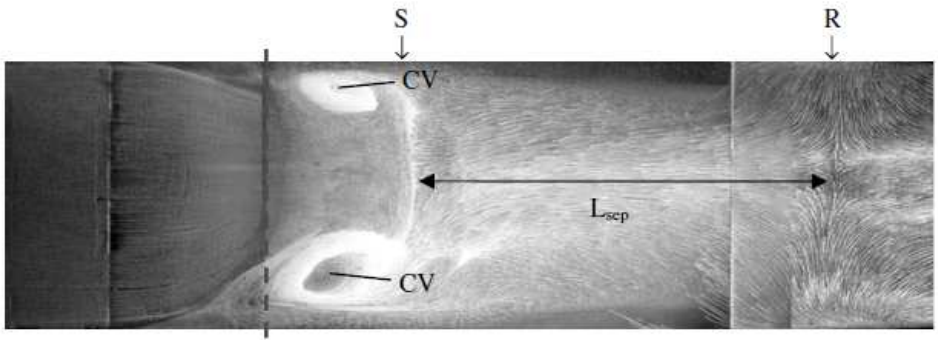

(b) Oil flow visualization of separated supersonic flow without flow control.

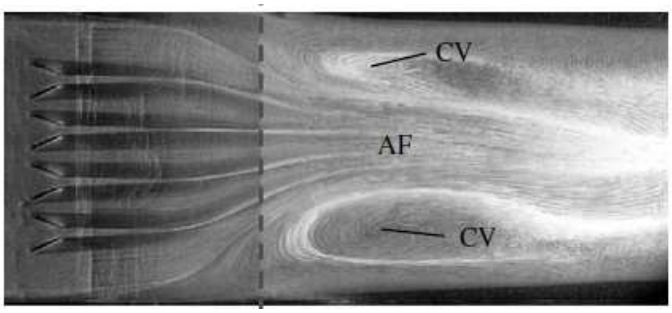

(c) Oil flow visualization of attached supersonic flow with vortex generator control.

Figure 1.4: Demonstration of flow separation control in supersonic flow using passive vortex generators [13].

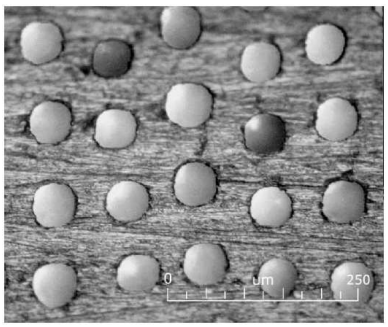

(a) Surface porosity

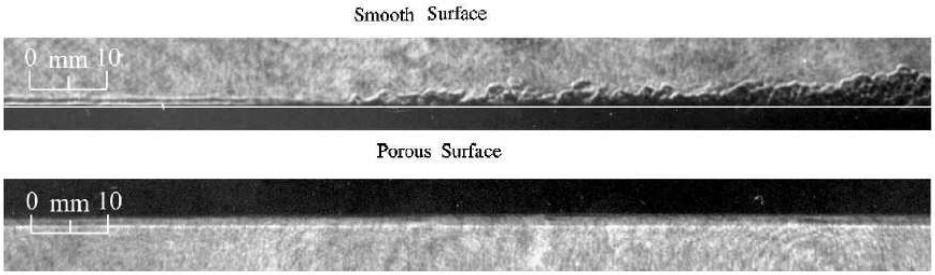

(b) Schlieren images of delayed transition.

Figure 1.5: Picture of surface porosity demonstrating the hole size and distribution for delaying boundary layer transition in hypersonic flow [14].

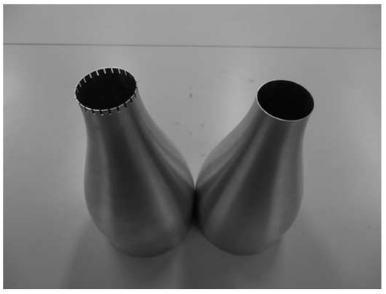

(a) Clean vs. Notched Nozzle Exit.

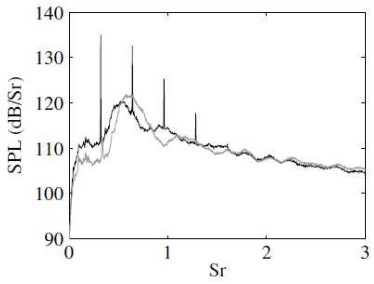

(b) Sound pressure levels associated with a clean nozzle and a notched nozzle.

Figure 1.6: Effect of a notched nozzle exit on the sound pressure levels versus Strouhal number (Sr) associated with screech tones [10].

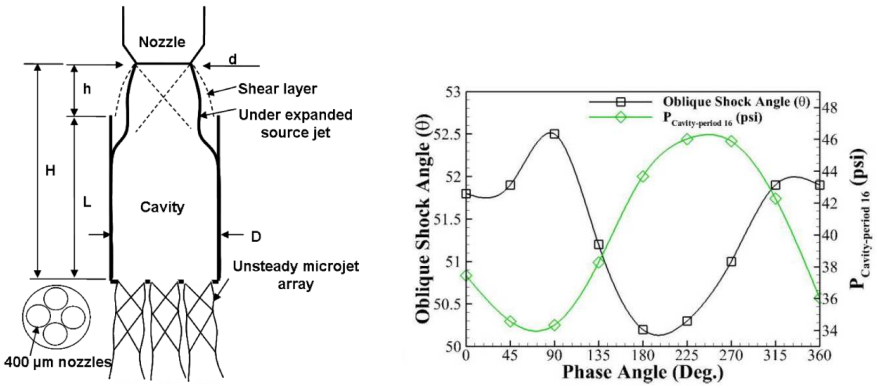

(a) Sketch of REM design sizing parameters [27].

(b) Phase-averaged cavity pressure and corresponding effect on supersonic crossflow [24].

Figure 1.7: Design requirements and output for unsteady REM actuation.

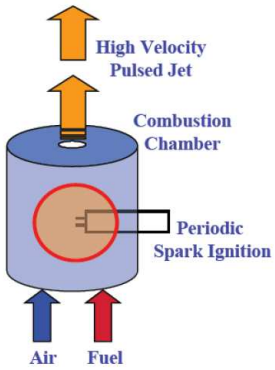

Figure 1.8: Sketch of the COMPACT [28].

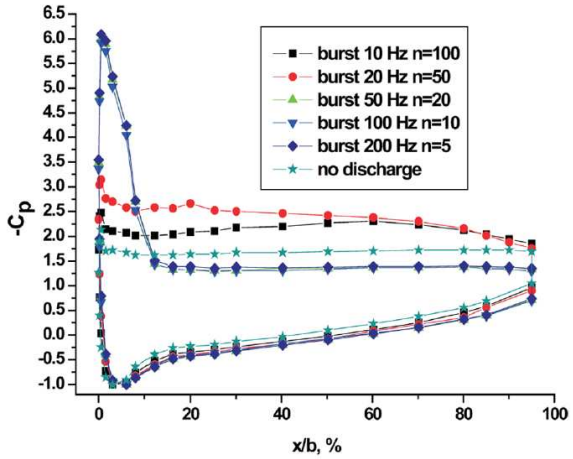

Figure 1.9: Effect of nanosecond discharge on the coefficient of pressure (C_p) distribution versus the percentage of the chord length (x/b, %) over an airfoil in transonic flow [32].

Chapter 2

SparkJet Actuator

This chapter describes the basic operating principles of the SparkJet actuator based on a three stage cycle. In addition, work conducted prior to, and outside of, this dissertation is discussed to illustrate the state of the art. Through this discussion, the need to further develop a simplified model and acquire additional experimental data to support 1-D modeling is highlighted.

2.1 Device Description

The SparkJet is a solid-state device containing no moving parts and has no external air supply making it a ZNMF device. It consists of a small cavity with embedded electrodes and an orifice through which air can pass freely. The operation of the SparkJet is illustrated in Figure 2.1 as a series of stages. Stage 1 is characterized by a brief arc discharge within the cavity to produce hot, high-pressure plasma and air. Stage 2 involves venting the high-pressure plasma and air through the orifice, which converts the thermal energy of the discharge into kinetic energy. Stage 3 involves a cooling/refresh phase (Stage 3) prior to the beginning of the next arc discharge (Stage 1).

The basic SparkJet cycle is dependent on a multitude of parameters including the magnitude of input energy; actuation frequency; orifice area and shape; cavity

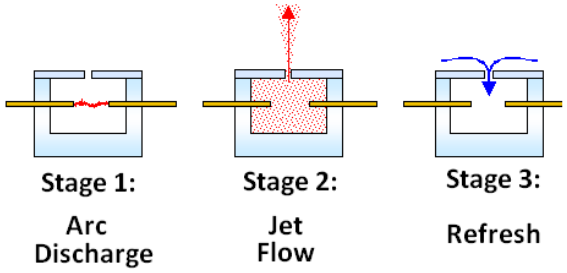

Figure 2.1: Basic schematic of the three stages of SparkJet operation.

volume and shape; electrode spacing, diameter, and shape; and cavity wall thermal properties. When considering flow applications, an array of SparkJets interacting with external flow conditions will be dependent on external flow conditions (pressure, temperature, velocity, inherent instability frequency). In addition, the number of and spacing between collocated SparkJets would affect spatial and temporal interactions between devices. The physics and other details pertaining to each stage are described in the following sections.

2.1.1 Stage 1 - Arc Discharge

The primary goal of Stage 1 is to raise the cavity air temperature and pressure quickly and with maximum efficiency. The method of accomplishing this goal is by the use of a brief, high-current, arc discharge sustained by a charged capacitance parallel to the anode (high-voltage) and cathode (ground). The maximum amount of input energy, Q_C, is predicted by

$$Q_C = \frac{1}{2}CV^2, \tag{2.1}$$

where C is the capacitance and V is the voltage. Another parameter important to understanding Stage 1 is the internal cavity energy, E, just before the arc discharge

given by

$$E = mC_vT. \tag{2.2}$$

At this point, a valuable parameter Q_C/E can also be defined as

$$\frac{Q_C}{E} = \frac{1/2CV^2}{mC_vT}, \tag{2.3}$$

which provides a sense of the amount of energy stored in the SparkJet cavity prior to Stage 2. This parameter is simply the ratio of input energy to the internal cavity energy.

Currently, the method of initiating the arc discharge is through a high-voltage, low-current trigger spark. In the very first SparkJet device [40], Stage 1 was initiated by increasing the voltage across the anode and cathode until the breakdown voltage between the electrode tips was exceeded and the trigger spark was initiated. However, this technique posed problems when attempting to acquire characterization data because the time between the voltage increase and the arc discharge would vary, making data difficult to capture experimentally. Therefore, the initiation technique changed to the use of a trigger spark between a trigger electrode and the cathode that was achieved using an external trigger circuit. Further triggering details are discussed in Chapter 4 including an improved triggering technique.

Regardless of the exact trigger setup, once the trigger mechanism induces the capacitive arc breakdown, the rest of Stage 1 involves the conversion of capacitor energy into Joule heat causing the cavity pressure to rise. The energy which increases the temperature and, therefore, pressure in the SparkJet cavity is of most interest to SparkJet performance. However, experimental results presented in Chapter 5 expose

some inefficiencies based on comparison between experimental data and modeling solutions. Analysis of the arc power in Chapter 6 helps identify the cause of the energy losses. Once the arc discharge is complete and the temperature and pressure of the air in the cavity have reached their maximum values, Stage 1 is complete.

2.1.2 Stage 2 - Jet Flow

The SparkJet jet formation and flow is a very unsteady process initiated by the sudden pressure differential across the orifice face generated by high-temperature and high-pressure cavity air from Stage 1. As the cavity air is forced through the orifice, the cavity pressure decreases due primarily to the decrease in cavity density and secondarily to the thermal losses through forced and free convection. Collaborative efforts outside this dissertation work with Florida State University (FSU) have enabled the acquisition of microschlieren imagery of the early jet development. Figures 2.2(a) and 2.2(b) show microschlieren images of the SparkJet flow 12 μs and 100 μs, respectively, after Stage 1 was initiated. These images show that the first evidence of the SparkJet formation is a blast wave (called a precursor shock by other researchers [41]) which appears only 6 μs after the Stage 1 initiates. Immediately following the blast wave is the jet front which, over the course of 100 μs develops into a fully turbulent jet. By phase-averaging multiple images, evidence of locally supersonic flow is apparent [42].

The duration of Stage 2 is primarily controlled by the cavity volume, orifice area, and heat transfer. In general, decreasing orifice area and cavity volume in-

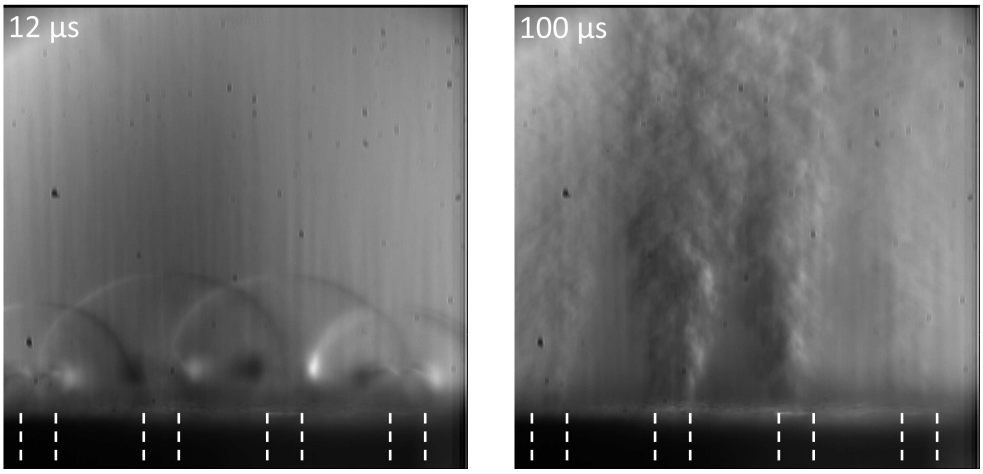

(a) 12 μs (b) 100 μs

Figure 2.2: Microschlieren images at two time delays after Stage 1 initiation showing the a) blast wave and b) turbulent jet formation in the early portion of Stage 2 [42].

crease the duration of Stage 2. The jet flow can also be affected by contouring the orifice throat. The studies presented in this dissertation only involve a constant area throat but other studies have investigated a converging orifice [41] and a converging-diverging orifice [43] to increase jet Mach number. At the very end of Stage 2, the cavity pressure decreases to ambient pressure but the momentum of the flow passing through the orifice further decreases the cavity pressure below ambient pressure extending Stage 2 until the adverse pressure gradient decreases the jet momentum to zero.

2.1.3 Stage 3 - Refresh

Finally, once the fluid momentum is zero, the decreased pressure in the cavity forces the flow to reverse and increase the pressure and density of the cavity air. In addition, the ingested relatively cool external flow mixes with the high-temperature cavity air thereby reducing the overall cavity temperature. Further reduction in cavity temperature occurs due to free convection of the air to the cooling cavity walls and electrodes. The primary parameters that affect the duration of Stage 3 are again cavity volume, orifice diameter, and thermal conductivity of the walls and electrodes.

Stage 3 typically lasts long enough to raise concerns about SparkJet frequency limitation. For example, if the time from Stage 1 to the end of Stage 3 exceeds 1 ms and an actuation frequency of 1 kHz is desired, the arc discharge will occur when the cavity density is lower and the temperature is higher than the first actuation event. While this leads to a higher Q_C/E value due to a lower E value, the lack of cavity density and mass leads to a lower momentum output during Stage 2 and a decreased ability to affect the external flow. This dissertation uses the modeling results to learn the design parameters that control high-frequency performance.

2.2 Previous Work

Prior to the work presented in this dissertation, previous studies had taken place at JHU/APL to study the SparkJet and its performance. In addition, several other organizations have begun conducting independent evaluations of SparkJet de-

vice (or similar) performance. These previous studies are outlined in the following paragraphs which describe analytical modeling, numerical modeling, and experimental testing efforts by JHU/APL and other organizations.

2.2.1 Analytical Modeling

The desire to simplify the complexities of the SparkJet process is evident by the efforts outlined in this section to produce an analytical model. The development of the SparkJet originated at JHU/APL and, therefore, the first experimental studies and modeling of the device was also performed by JHU/APL. Initial SparkJet analysis debuted with a simplified, first-order, one-dimensional analytical model, a limited collection of schlieren images and CFD simulations of a SparkJet issuing into quiescent flow [40]. The analytical model was based on the conservation of energy equation,

$$\frac{d}{dt}\left(\rho e v\right) = \dot{Q} - \dot{m} h_t - \dot{Q}' A_{SURFACE}, \tag{2.4}$$

which equates the time dependent change in energy to the summation of three terms that are separately independent of time but represent the three stages of SparkJet operation. The primary assumptions in this model include an instantaneous energy deposition during Stage 1 with negligible heat loss and the cavity air is calorically perfect.

The first term on the right-hand side of Equation 2.4 represents the energy gain during Stage 1 due to the arc discharge. The second term represents the energy loss during Stage 2 due to enthalpy loss as the high-temperature and high-

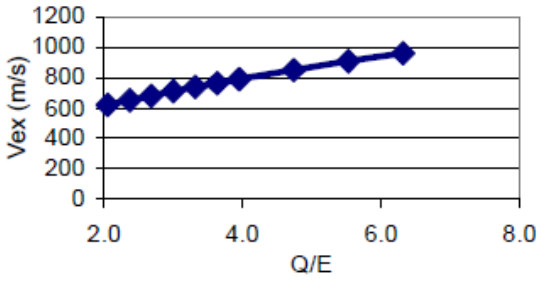

Figure 2.3: SparkJet flow velocity at the orifice based on a simplified, one-dimensional, analytical model developed by Grossman, et al. [40].

pressure cavity air exits the control volume through the orifice. The third term represents the final energy loss through heat transfer to the surface while the control volume temperature, pressure, and density return to equilibrium. Calculation of the three terms led to a physics-based understanding of the SparkJet operation and the influence of various parameters on SparkJet performance. Figure 2.3 shows the predicted maximum exit velocity of the SparkJet during Stage 2 which increases with Q/E, the ratio of input energy to internal cavity energy. This quantity, Q/E was first identified in this paper as an important non-dimensional parameter for understanding SparkJet performance and is continuously used throughout follow-on papers. In this dissertation, several energy sources are identified; therefore, Q_C in this dissertation is equivalent to Q in previous papers. No further modifications to this first analytical model were made; however, other simplified modeling efforts have emerged from other organizations.

In 2012, Anderson and Knight at Rutgers University documented a one-dimensional, analytical model which included an in-depth dimensional analysis [44]. Anderson's model and the early JHU/APL modeling efforts are similar in that they

simplify the SparkJet to a 1-D representation, assume calorically perfect gas, inviscid flow, adiabatic walls and prescribed, instantaneous energy input. Based on these assumptions, the models seek to quantify several performance parameters based on fluidics. Both of these studies consider a single cycle with limited discussion of Stage 3 operation. Therefore, these models are not capable of capturing high-frequency actuation.

2.2.2 Computational Modeling

Higher-fidelity simulations of the SparkJet actuator involve CFD analysis. Several organizations have conducted CFD studies of the SparkJet actuator including JHU/APL, Rutgers University and the Office National d'Etudes et de Recherches Arospatiales (ONERA). For analysis of a single SparkJet with a single orifice, the simulations are two-dimensional taking advantage of the axisymmetric properties of the basic SparkJet design. Initial CFD studies began at JHU/APL simulating a SparkJet firing into quiescent flow using unsteady Reynolds-Averaged Navier-Stokes (URANS) simulations. Computational studies using CFD++ were used understand the SparkJet influence of a quiescent flow and then to determine of the SparkJet concept was capable of influencing the boundary layer of a Mach 3 flat plate cross-flow [45]. Computational results showed that not only did the SparkJet influence the supersonic boundary layer but also penetrated into the freestream crossflow. Follow-on computational efforts were made to allow for analysis of a SparkJet actuator array on a large-scale application such as a missile body [46].

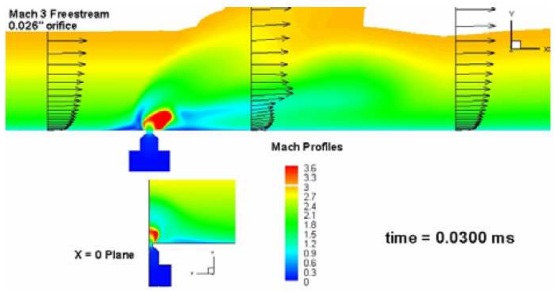

Figure 2.4: First CFD simulation of SparkJet interaction with a Mach 3 crossflow over a flat plate [45].

At Rutgers University, Anderson and Knight used a finite volume code called GASPex (export version of GASP) to simulate the SparkJet flow [47]. The simulation efforts considered a single SparkJet (called *plasma jet* in the paper) interacting with both a quiescent flow and a Mach 3 turbulent boundary layer over a flat plate. The quiescent flow cases considered the SparkJet performance for a range of input energy levels, Q_C, while the flat plate simulations considered the effect of orifice diameter, d_o, on the SparkJet impulse. Comparisons were made between the computational simulations and the Rutgers-developed analytical model. Results showed that the analytical model and computational simulation agree very well for interactions with a quiescent flow. The Mach 3 flat plate cases show that the impulse generated by the SparkJet is significantly affected by the flow environment. For example, the impulse generated in quiescent flow was compared to the impulse generated in the flat plate flow and results showed that the impulse is significantly lower for the quiescent flow than the flat plate flow case. While the simulations showed that the jet velocity at the orifice is lower for the flat plate flow case than the qui-

escent case, the difference in impulse is primarily due to the longer jet duration in the flat plate flow case.

ONERA has also conducted a two-dimensional, axisymmetric, URANS simulation of the SparkJet (called a plasma synthetic jet) interaction with a quiescent flow and a crossflow assuming a prescribed energy input using their in-house CFD code called CEDRE CFD [43]. Follow-on work also included simulation of the arc discharge [48]. The fluidic simulations of the quiescent flow interactions track the cavity pressure and temperature as well as the orifice velocity and mass flow rate. The CFD analysis was used to study the effect of shaping the SparkJet orifice and cavity shape for a fixed volume. Results showed, not surprisingly, that a converging-diverging nozzle provides the best SparkJet performance based on exit Mach number. The parametric cavity shape simulations showed that the height to diameter ratio of the cavity primarily affect the influence of viscous effects. For example, a tall, narrow cavity results in a relatively longer jet duration but lower total mass ejection than a short, wide cavity. This is due to the fact that viscous losses on the cavity walls are more dominant in the tall, narrow cavity. However, viscous effects are prevalent on the walls of the orifice for the short, wide cavity shape because the streamlines are highly curved as the fluid leaves the cavity through the orifice leading to a thicker boundary layer. Finally, the simulations also show that walls with high conductive heat transfer lead to shorter refresh durations. Three-dimensional, URANS simulations of the SparkJet interacting with a relatively low speed (21.5 m/s) crossflow and preliminary comparisons to experimental data verified that the simulation captures the pair of vortices surrounding the jet orifice and

the jet penetration of the boundary layer.

2.2.3 Experimental Characterization

While simulations and modeling have estimated the potential strength and usefulness of the SparkJet actuator, experimental tests were conducted to confirm the modeling results. At JHU/APL, the first experimental results were acquired using schlieren with a continuous light source and a camera featuring a fast shutter speed [40]. The qualitative schlieren images provided visualization of the SparkJet jet flow and a sense of the operation. Quantitative data acquired from the schlieren imagery was limited to jet duration and an initial estimation of the jet front velocity.

To acquire more quantitative data, particle image velocimetry (PIV) was used to analyze the local velocity within the core of the SparkJet jet flow [49]. At this time, verification of supersonic flow features in the SparkJet jet flow was of interest. However, the seed particles used for the PIV studies were too large to follow the highest velocity flow in the core of the SparkJet jet flow and the maximum velocity measured was only 100 m/s and 50 m/s in a separate PIV measurement attempt [50]. The flow velocities captured by the PIV were of the entrained flow rather than the jet flow.

In a collaborative effort between JHU/APL and JHU, improved experimental results were found using a completely non-intrusive, optical technique called digital speckle tomography (DST) [50]. This technique relies on density or temperature gradients in the SparkJet jet flow altering a speckled background image. The opti-

cal movement of the speckles is calibrated such that a density or temperature can be quantified along a line that intersects the jet flow. This study captured the temperature profile across the SparkJet 1.8 mm above the orifice as a function of time. These results showed that for an input energy of 0.03 J, the maximum temperature measured was 1600 K which aligned well with computational results.

Another attempt to quantify SparkJet performance was using a custom-built thrust stand to measure impulse [49]. The thrust stand results showed that the SparkJet impulse varied linearly with the amount of energy deposition. Specifically, the impulse varied from 1.5 μN-s at 0.03 J and 2.7 μN-s at 0.9 J.

As seen with the analytical and computational modeling efforts, several other organizations have experimentally tested the SparkJet including the University of Texas at Austin, ONERA, the University of Illinois, the National Aeronautics and Space Administration (NASA) Langley Research Center, and the University of Florida. At the University of Texas at Austin, the actuator (called a *pulsed plasma jet* (PSJ)) design was similar to the SparkJet in that an arc within the cavity initiated the jet flow. However, the PSJ actuator was only evaluated at very low pressures (45 torr). The actuator design consisted of a 5 mm electrode gap and the arc current was controlled such that it was maintained for $20 - 50$ μs at 1.1-3.9 A [51]. Experimental testing was primarily based on schlieren imagery in addition to planar laser scattering (PLS) of flow interactions with quiescent and a Mach 3 flow over a 30° corner. While significant differences in design and operating conditions exist between the SparkJet and the PSJ actuator, the experimental results demonstrated important flow interactions. To summarize the highlight of the results, the

flow responsiveness was directly related to the frequency of the actuator and the actuator had the most effect on the separation bubble at the compression corner when placed upstream of the separation bubble. These results demonstrated the ability of such an actuator to control the frequency of fluid structures at Mach 3 flow conditions.

At the University of Illinois, both quiescent and Mach 3 crossflow experiments were conducted. The actuator design used for these studies was very similar to the SparkJet but the researchers refer to the actuator as a *pulsed plasma jet actuator* (PPJA). For the quiescent flow studies [41], schlieren, and PIV images were used to characterize the PPJA flow over a wide range of input energy values controlled by the capacitance values of 0.25 μF, 2 μF, 25 μF and 68 μF. The results show that the PPJA flow starts with a blast wave referred to as a precursor shock with a velocity independent of the energy deposition level. The contact surface (i.e. jet front) velocity varies with input energy as seen in Figure 2.5.

The PIV images obtained from the quiescent experiments at University of Illinois are very revealing of the PPJA flow and their ability to seed the ambient flow is a clear improvement over previous PIV efforts by JHU/APL. Figure 2.6 shows the velocity field contours of the PPJA flow at 30 μs, 50 μs, 70 μs and 90 μs delay times for a capacitance of 25 μF. The maximum flow velocity easily exceeds the speed of sound based on ambient temperature; however, shock cells are not visible because the local temperature in the jet is higher than the ambient temperature such that the local Mach number is below unity. Further data processing of the PIV images show that beyond 90 μs, the jet velocity gradually decreases. The magnitude of

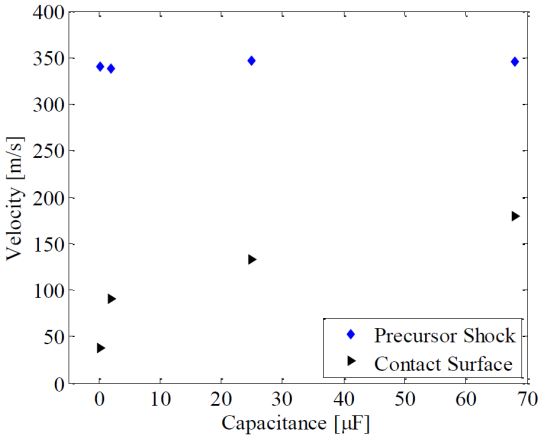

Figure 2.5: Variation in velocities determined from schlieren images for the pulsed plasma jet for various capacitive energy depositions [41].

the velocity is proportional to the magnitude of input energy. The axial velocity profiles also show that the velocity across the jet is fairly uniform even at an early time delay of 30 μs. Only the low energy deposition case shows non-uniformity but that is likely due to the strong presence of vortices. The transverse velocity profiles show that the jet has an influence on the flow three orifice diameters wide.

The Mach 3 crossflow studies conducted by Illinois used PIV and schlieren to investigate the interaction between a single SparkJet in a Mach 3 crossflow [52]. The results showed that the SparkJet, using 2 μF across the anode and cathode weakly affected the crossflow. The PIV results showed that the maximum velocity perpendicular to the crossflow from the SparkJet was 60 m/s. The primary conclusion from this work was that further investigation is needed to understand the weak influence.

Extensive experimental work related to the SparkJet (called a *plasma synthetic jet* (PSJ)) has occurred at ONERA [43, 53]. First experimental tests characterized

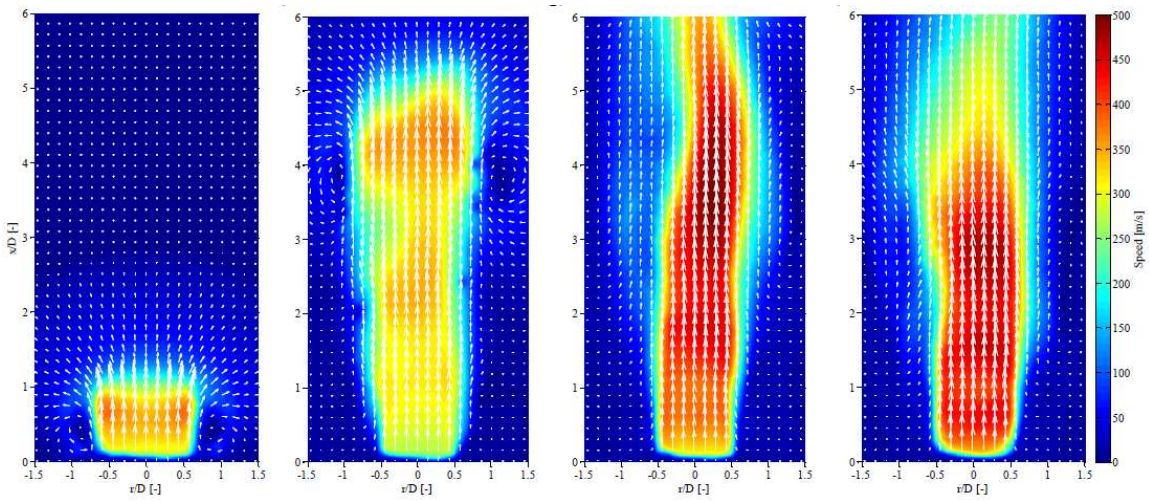

Figure 2.6: Average velocity field contours and vectors for the 25 μF discharge at 30 μs, 50 μs, 70 μs and 90 μs delay times [41].

the PSJ design as a function of cavity wall thermal conductivity, orifice diameter, frequency, and input energy. The PSJ design was very similar to the first SparkJet design by JHU/APL that contained a center anode and used a metal lid as the cathode. The experiments examined the effect of the orifice diameter, lid material, and frequency on the pressure rise in the cavity. The results showed that as orifice diameter decreases and actuation frequency increases, the pressure rise in the chamber decreases. They also show that as actuation frequency increases and lid thermal conductivity decreases, the pressure rise decreases. These results suggest that maintenance of a prescribed pressure rise in the cavity at high actuation frequencies requires an increase in thermal heat transfer through the actuator materials. ONERA also experimentally tested a single PSJ in a wind tunnel to examine interactions between a pitched and skewed PSJ and a 40 m/s crossflow. Results showed that the PSJ influences the flow much like a synthetic jet or vortex gen-

erator. Experimental testing was also conducted to study the interaction between a PSJ and a high subsonic jet (Mach 0.6 and 0.9). Based on schlieren imagery, the PSJ clearly affects the jet shear layer and demonstrates potential to control jet noise.

Only very recently, NASA Langley Research Center (in collaboration with Rutgers University) has begun testing the SparkJet actuator in quiescent flow [54]. The purpose of the experiments was to measure the impulse (and efficiency) provided by the SparkJet by fixing the SparkJet to the end of a pendulum and measuring the displacement due to SparkJet operation. The measured displacement was converted to an impulse and then compared to an analytical model created by Rutgers University. The specific dimensions of the SparkJet actuator used in these studies include a cavity volume of 214.9 mm^3, an orifice diameter of 1 mm, a capacitance of 3-40 μF, a charging voltage of 550 V, and an electrode gap of 1 mm. The results showed that the actuator design used for this study provided an angular deflection up to 0.015° which corresponded to an efficiency of only 8%. This low efficiency value is most likely due to the small electrode gap coupled with voltage potential drops in the long cables connecting the actuator to the power supply.

The prior work presented in this chapter illustrates the need for further exploration of SparkJet. For example, modeling of Stage 3 of the SparkJet cycle is needed for high-frequency actuation modeling. In addition, several organizations have studied the resulting jet flow during Stage 2 but the internal cavity conditions are still largely unknown experimentally. Chapter 3 of this dissertation presents a simplified 1-D model which includes Stage 3 modeling and, therefore, the effect

of design parameters on high-frequency actuation performance is explored. Additionally, Chapters 5 and 6 present experimentally acquired cavity pressure and arc power data. These experimental results answer questions pertaining to actuator efficiency and the sources of inefficiency in actuator design.

Chapter 3

1-D Analytical Model

The goal of this chapter is to present and demonstrate a one-dimensional numerical model to describe the SparkJet operation. Through variation of several design and operating parameters, methods to optimize the design for high-frequency operation are understood. In addition, a comparative study is included between a SparkJet CFD simulation previously conducted [55] and the 1-D model presented in this chapter to gain confidence in the 1-D model.

3.1 Description of the Problem

The development of a 1-D model of the SparkJet actuator cycle began in 2003 [40]. The work presented in 2003 presented a three-stage model for the initial energy deposition, isentropic choked jet flow followed by unchoked jet flow, and refresh stage. A similar approach is used in this chapter by modeling the SparkJet according to the three stages of actuation. Each stage of the SparkJet cycle (shown in Figure 2.1) is analyzed separately. To one-dimensionalize the problem, pressure, temperature, and density are assumed averaged over the entire cavity volume and the jet velocity is assumed significant only at the throat of the orifice and zero in the cavity. Figure 3.1 shows a sketch of the control volume used to analyze the SparkJet; the larger volume represents the cavity and smaller volume represents the

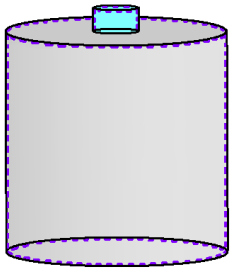

Figure 3.1: Sketch of the assumed control volume where the larger volume represents the cavity volume, the smaller volume represents the orifice volume.

throat. The dashed lines surrounding the control volume represent the walls of the SparkJet actuator. The orifice, at the top of the throat volume, is the only surface area through which air is able to pass.

3.2 Governing Equations

The governing equations used to model the SparkJet cycle involve basic thermodynamics and fluid dynamics. The plasma chemistry involved in the arc formation and resulting heat generation is modeled using simple thermodynamics. The fluid dynamics are represented by a 1-D derivation of the Euler equations combined with a thermal model of heat loss to the internal SparkJet actuator surfaces.

3.2.1 Stage 1

To initiate Stage 1 of the SparkJet cycle, an instantaneous energy input, Q_C, of an assumed value from the capacitive arc discharge is used to determine the temperature rise from T_1, the temperature prior to the arc discharge, to T_2, the

temperature after the arc discharge. The generic thermodynamic equation used to determine a temperature rise due to an energy input is given by

$$\Delta T = \frac{q}{mC_v}. \tag{3.1}$$

Defining the temperature rise $\Delta T = T_2 - T_2$, $q = Q_C$, and recalling Equation 2.2,

$$T_2 = T_1 \left(1 + \frac{Q_C}{E}\right) \tag{3.2}$$

is used to calculate the peak temperature at the beginning of Stage 2. Using the ideal gas law and under the assumption that no mass has exited the cavity during this instantaneous energy deposition, the peak pressure, P_2, is determined by

$$P_2 = \rho R T_2 = \rho R T_1 \left(1 + \frac{Q_C}{E}\right). \tag{3.3}$$

Several assumptions were made to simplify modeling Stage 1. The real arc discharge process for the SparkJet actuator takes place over hundreds of nanoseconds. The temperatures within the arc column vary from 5000 to 30000 K during a single discharge. During the discharge, a thermal and pressure wave emanate from the arc column at a speed near 500 m/s [42]. When considering a real arc discharge, one realizes that the process is highly time and space dependent. However, a goal of this dissertation is to simplify such complex processes using various assumptions and also to determine the validity of such assumptions for evaluating the SparkJet cycle. In addition to the complexities of the arc discharge itself, transferring the capacitive discharge energy, Q_C, to thermal energy is known to be an inefficient process [56]. These inefficiencies are explored in Chapters 5 and 6.

3.2.2 Stage 2

To initiate Stage 2, T_2 and P_2 from Stage 1 are used as initial conditions and no more energy is added to the system. The Euler equations, separately identified as the conservation of mass, momentum, and energy equations, are used to describe the change in cavity conditions for Stage 2 as a function of time. The complete, integral form of the conservation equations are given by

$$\frac{\partial}{\partial t}\iiint_v \rho dv + \iint_S \rho \mathbf{U}\cdot\mathbf{dS} = 0, \tag{3.4}$$

$$\frac{\partial}{\partial t}\iiint_v \rho \mathbf{U} dv + \iint_S (\rho \mathbf{U}\cdot\mathbf{dS})\,\mathbf{U} = -\iint_S p\mathbf{dS} + \iiint_v \rho \mathbf{f} dv + \mathbf{F}_{viscous}, \tag{3.5}$$

and

$$\begin{aligned}&\frac{\partial}{\partial t}\iiint_v \rho\left(e+\frac{U^2}{2}\right)dv + \iint_S \rho\left(e+\frac{U^2}{2}\right)\mathbf{U}\cdot\mathbf{dS}\\ &= \iiint_v \dot{q}\rho dv + \dot{Q}_{viscous} - \iint_s p\mathbf{U}\cdot\mathbf{ds} + \iiint_v \rho\,(\mathbf{f}\cdot\mathbf{U})\,dv + \dot{W}_{viscous}.\end{aligned} \tag{3.6}$$

The assumptions used to simplify Equations 3.4-3.6 are consolidated below followed by the derivations corresponding to these assumptions.

1. Body forces are negligible
2. Inviscid flow
3. Velocity is negligible in the cavity volume and significant through the throat volume
4. Velocity, pressure, temperature, and density across the orifice are uniform and represented by scalar values

5. Pressure, temperature, and density are uniform inside the cavity volume (1-D)

6. Stages 2 and 3 are calorically perfect

The first assumption used to simplify these equations is assuming that viscous effects and body forces, $\mathbf{f}$, are negligible. Body forces include forces due to gravity, electromagnetism and other forces which "act at a distance" [57] and are small compared to pressure forces. Viscous effects are considered negligible due primarily to the small scale of the cavity and the small throat length to diameter ratio. If the throat were long and narrow, viscous forces would need to be considered. The resulting inviscid, integral form of the conservation equations are given by

$$\frac{\partial}{\partial t}\iiint_v \rho dv + \iint_S \rho \mathbf{U}\cdot\mathbf{dS} = 0, \tag{3.7}$$

$$\frac{\partial}{\partial t}\iiint_v \rho \mathbf{U} dv + \iint_S (\rho \mathbf{U}\cdot\mathbf{dS})\,\mathbf{U} = -\iint_S p\mathbf{dS}, \tag{3.8}$$

and

$$\frac{\partial}{\partial t}\iiint_v \rho\left(e+\frac{U^2}{2}\right)dv + \iint_S \left(\rho\left(e+\frac{U^2}{2}\right)\mathbf{U}\cdot\mathbf{dS}\right) = \iiint_v \dot{q}\rho dv - \iint_s p\mathbf{U}\cdot\mathbf{ds}. \tag{3.9}$$

To simplify the surface integrals, the control volume shown in Figure 3.1 is considered. The only surface area through which fluid can pass or a pressure gradient can act upon the fluid is at the interface between the orifice and the external flow, A_o. Furthermore, the pressure, temperature, density, and velocity across the orifice interface are assumed constant. The velocity through the orifice is assumed exactly parallel to the surface normal vector and is converted to a scalar rather than a vector. The pressure term, p, at the orifice interface is equivalent to the difference

between the cavity pressure, P, and the exit pressure, P_e, such that $p = P - P_e$. The equations showing the effect of applying these assumptions are given as

$$\frac{\partial}{\partial t}\iiint_v \rho dv + \rho U A_o = 0, \tag{3.10}$$

$$\frac{\partial}{\partial t}\iiint_v \rho \mathbf{U} dv + \rho U^2 A_o = -\left(P - P_e\right) A_o, \tag{3.11}$$

and

$$\frac{\partial}{\partial t}\iiint_v \left(\rho e\right) dv + \frac{\partial}{\partial t}\iiint_v \rho\frac{U^2}{2} dv + \rho\left(e + \frac{U^2}{2}\right) U A_o = \iiint_v \dot{q}\rho dv - \left(P - P_e\right) U A_o. \tag{3.12}$$

In preparation for simplifying the volume integrals, the unsteady terms are also expanded in the energy equation.

The next assumption to simplify the equations is that the density, pressure, and temperature inside the cavity are uniform and that the only significant velocity values are uniform in the orifice volume only. Therefore, any volume integrals with a velocity term are integrated over the orifice volume whereas volume integrals without a velocity term are integrated over the cavity volume. Acknowledging that the cavity and orifice volumes are independent of time, the equations resulting from these simplifications are

$$v\frac{\partial \rho}{\partial t} + \rho U A_o = 0, \tag{3.13}$$

$$v_o\frac{\partial\left(\rho U\right)}{\partial t} + \rho U^2 A_o = -\left(P - P_e\right) A_o, \tag{3.14}$$

and

$$v\frac{\partial\left(\rho e\right)}{\partial t} + v_o\frac{\partial\left(\rho\frac{U^2}{2}\right)}{\partial t} + \rho\left(e + \frac{U^2}{2}\right) U A_o = \dot{q}\rho v - \left(P - P_e\right) U A_o. \tag{3.15}$$

All terms in Equations 3.13-3.15 not included in the time derivative are moved to the right-hand side. The conservation of mass equation then becomes

$$v\frac{\partial \rho}{\partial t} = -\rho U A_o. \tag{3.16}$$

Additionally, using the product rule for derivatives, the time derivatives in the momentum (Equation 3.14) and energy (Equation 3.15) equations are expanded into

$$v_o\left(\rho\frac{\partial U}{\partial t} + U\frac{\partial \rho}{\partial t}\right) = -\left(P - P_e\right)A_o - \rho U^2 A_o \tag{3.17}$$

and

$$v\frac{\partial\left(\rho e\right)}{\partial t} + v_o\left(2\rho U\frac{\partial U}{\partial t} + U^2\frac{\partial \rho}{\partial t}\right) = \dot{q}\rho v - \left(P - P_e\right)UA_o - \rho\left(e + \frac{U^2}{2}\right)UA_o, \tag{3.18}$$

respectively.

Assuming that the equations are solved in sequence starting with the continuity equation, $\partial\rho/\partial t$ and $\partial U/\partial t$ are considered knowns in Equations 3.17 and 3.18 and are also moved to the right-hand side. At this point, the derivation of the conservation of mass,

$$\frac{\partial \rho}{\partial t} = -\left(\frac{\rho U A_o}{v}\right), \tag{3.19}$$

and momentum,

$$\frac{\partial U}{\partial t} = \frac{1}{\rho}\left(\frac{-\left(P - P_e\right)A_o - \rho U^2 A_o}{v_o} - U\frac{\partial \rho}{\partial t}\right), \tag{3.20}$$

equations is complete. However, for the energy equation,

$$v\frac{\partial\left(\rho e\right)}{\partial t} = \dot{q}\rho v - \left(P - P_e\right)UA_o - \rho\left(e + \frac{U^2}{2}\right)UA_o - v_o\left(2\rho U\frac{\partial U}{\partial t} + U^2\frac{\partial \rho}{\partial t}\right), \tag{3.21}$$

we need to assume a calorically perfect gas and that Stage 2 is a constant volume process, such that the internal energy can be defined as $e = C_v T$. Applying this

definition of internal energy to Equation 3.21 allows the energy equation to be given as

$$v\frac{\partial\left(\rho C_v T\right)}{\partial t} = \dot{q}\rho v - \left(P - P_e\right) U A_o - \rho\left(C_v T + \frac{U^2}{2}\right) U A_o - v_o\left(2\rho U\frac{\partial U}{\partial t} + U^2\frac{\partial \rho}{\partial t}\right). \tag{3.22}$$

Applying the ideal gas law to the left-hand side of Equation 3.22, the temperature derivative can be converted to a pressure derivative as shown by the equality

$$v\frac{\partial\left(\rho C_v T\right)}{\partial t} = v\frac{\partial\left(\rho C_v \frac{P}{\rho R}\right)}{\partial t}. \tag{3.23}$$

By removing the constants C_v and R from the time derivative,

$$\frac{vC_v}{R}\frac{\partial P}{\partial t} \tag{3.24}$$

is the resulting term on the left hand side of Equation 3.22. Finally, the energy equation is given by

$$\frac{dP}{dt} = \frac{\left(\dot{q}\rho v - \left(P - P_e\right) U A_o - \rho\left(C_v T + \frac{1}{2}U^2\right) U A_o - v_o\left(2\rho U\frac{dU}{dt} + U^2\frac{d\rho}{dt}\right)\right)}{\left(\frac{vC_v}{R}\right)} \tag{3.25}$$

and represented as the time derivative of pressure. While it is very likely that the temperatures reached in the cavity exceed that which allows us to make the assumption that C_v is constant, this assumption is made during this first model development iteration.

During Stage 2, the pressure ratio between the cavity and outside leads to the need for a choked and unchoked flow condition. The isentropic pressure ratio equation at Mach 1,

$$\frac{P}{P_\infty} = \left(1 + \frac{\gamma - 1}{2}M^2\right)^{\frac{\gamma}{\gamma - 1}} = \left(1 + \frac{\gamma - 1}{2}\right)^{\frac{\gamma}{\gamma - 1}} = 1.893, \tag{3.26}$$

which corresponds to the onset of choked flow, is used to determine when each condition exists. Therefore, Stage 2 is segmented into a choked flow condition followed by an unchoked flow condition that depends on the pressure ratio between the cavity pressure and the external pressure. Assuming a specific heat ratio for air, $\gamma = 1.4$, the solution at Mach 1 shows that if the pressure inside the cavity is above $1.893P_\infty$, the flow is considered choked and the pressure boundary condition at the orifice is set to $P_e = P/1.893$. Otherwise, the pressure at the orifice is equal to the ambient pressure for unchoked flow ($P_e = P_\infty$). Stage 2 ends with zero orifice velocity and high temperature, low density and slightly below atmospheric pressure air inside the cavity.

3.2.3 Stage 3

During Stage 3, the cavity is refreshed with relatively cool, high-density, ambient air due to the slight pressure gradient across the orifice which is maintained by the continued heat transfer to the internal cavity surfaces. As heat transfers to the Macor walls and electrodes, the air loses heat and is cooled which maintains a slight pressure gradient and continues to draw in air to bring the density up to ambient. Since the flow velocity is low throughout Stage 3, no choked flow conditions are experienced. The derivation and equations described for Stage 2 are identical to those used to simulate Stage 3 except where the equations describe the flow passing through the orifice. Therefore, the surface integrals in the original conservation equations involve ambient conditions rather than cavity conditions. Stage 3

modeling is accomplished using

$$\frac{d\rho}{dt} = -\left(\frac{\rho_\infty A_o U}{v}\right), \tag{3.27}$$

$$\frac{dU}{dt} = \frac{1}{\rho_\infty}\left(\frac{(P - P_\infty)\, A_o - \rho_\infty U^2 A_o}{v_o} - U\frac{d\rho}{dt}\right), \tag{3.28}$$

and

$$\frac{dP}{dt} = \frac{\left(\dot{q}\rho v - (P - P_\infty)\, U A_o - \rho_\infty \left(C_v T_\infty + \frac{1}{2}U^2\right) U A_o - v_o \left(2\rho_\infty U \frac{dU}{dt} + U^2 \frac{d\rho}{dt}\right)\right)}{\left(\frac{vC_v}{R}\right)} \tag{3.29}$$

to solve for the conservation of mass, momentum, and energy, respectively.

3.2.4 Thermal Modeling

As mentioned in Section 3.2.3, thermal heat transfer drives Stage 3, and therefore, cannot be ignored. Heat transfer is also present in Stages 1 and 2 such that a wide variety of heat transfer scenarios are considered here. This section considers the significance of each heat transfer mechanism (radiation, convection, and conduction) during a single SparkJet cycle and, as a result, considers two thermal modeling techniques: a combined lumped capacitance and thermal resistance model; and a model based on finite-difference discretization of the heat equation. These models are applied to identical thermal scenarios to determine which method accomplishes a suitable balance of simplicity and accuracy.

Based on arc discharge literature, the typical plasma temperatures reached for an arc in local thermal equilibrium at 1 atm are on the order of 5000-30000 K.

At such high temperatures, radiative heat effects require attention. The time constant associated with radiative heat transfer corresponds to the speed of light (299,792 mm/μs). Therefore, if radiative heat transfer is significant, the cavity air and surrounding Macor walls would increase temperature almost immediately.

According to Section 10.9.5 in Raizer [58], in air at a pressure of 1 atm, "radiative losses make up from one to several percent of the power input." The primary reason for the relatively low radiative energy output is because most of the radiative energy generated by the highest temperature plasma is absorbed by the surrounding plasma such that only a small amount of radiative energy is emitted by the arc column. With the intention of investigating an arc discharge such as that utilized during Stage 1, both ONERA [48] and UT Austin [59] have also provided numerical results based on a 2-D axisymmetric grid supporting the low losses due to radiative heat transfer. Therefore, radiative heat transfer in air at 1 atm is considered negligible for this thermal modeling. If operated at high pressure ($\approx$ 10 atm) radiative losses should be included in the thermal model.

Assuming the radiative losses are not significant, the remaining heat transfer mechanisms are conduction and convection. During the initial arc discharge, the primary mechanism is thermal conduction to the surrounding air and the electrodes. As the air is rapidly heated, an expanding, cylindrical blast wave emanates from the nearly cylindrical arc column. In the case of the SparkJet, the thermally conducting blast wave expands until it reaches the Macor walls. Based on the experimental cavity pressure measurements presented in Chapter 5, the blast wave takes approximately 5 μs to reach the walls. This relatively long delay until a pressure rise is

measured also supports the assumption of negligible radiative heat transfer. If radiative heat transfer was significant, a pressure rise would have begun immediately after the arc discharge initiated. Since the SparkJet cavity is shaped such that the cavity height and diameter are equivalent, the blast wave reaches all Macor walls at approximately the same instant neglecting the added time required to reach the cavity corners.

The subsequent pressure waves interact with the Macor walls resulting in an unsteady heat transfer to the walls. The frequency of this heat transfer primarily depends on the cavity dimensions. Also, because the cavity geometry (cylindrical) does not match the blast wave geometry (spherical), areas of the walls impacted by the blast wave at an angle will also experience convective heat transfer as the fluid "slips" along the surface of the walls. As heat is convectively transferred to the walls, conductive heat transfer transports the thermal energy through the SparkJet walls. Therefore, the thermal heat transfer during the SparkJet cycle includes concurrent conductive and convective heat transfer.

To properly model the thermal heat transfer process, the thermal energy transferred to the walls needs to be calculated from the beginning of Stage 2. There are a variety of thermal models available depending on the assumptions that can be made. Balancing simplicity and unsteady thermal effects, the lumped capacitance model is appealing. This model first uses the Biot number,

$$Bi = \frac{hL}{k} \tag{3.30}$$

to determine the validity of using this method where h is the convective heat transfer coefficient, L is the characteristic length, and k is the conductive heat transfer coefficient. If the Biot number is less than 0.1, the lumped capacitance method is considered valid. Physically, a low Biot number means that the spatial temperature distribution across the wall is constant such that conductive heat transfer is far more significant than convective heat transfer. Since the SparkJet walls offer two thermal heat transfer paths corresponding to each material, Macor walls and tungsten electrodes, two values for the Biot number are determined and both should be less than 0.1 to have confidence in the lumped capacitance method alone. The Biot number is approximately 0.34 for Macor and 0.003 for tungsten assuming h is 125 W/m^2; the wall thickness, L, is 4 mm; and thermal conductivity of Macor, k_M, and tungsten, k_W, are 1.46 W/mK and 173 W/mK, respectively. The low thermal conductivity of Macor, 1.46 W/mK, leads to a more substantial Biot number. Despite the Biot number of Macor exceeding 0.1, this method will be evaluated in a hybrid approach explained later. Additionally, the hybrid approach, which includes several simplifying assumptions, will be compared against higher-fidelity method that includes fewer assumptions.

Another commonly used thermal modeling method is based on thermal resistance. This method assumes that the system has reached a thermal steady-state condition and that the spatial thermal distribution is linear through the walls. While the SparkJet thermal condition is not steady-state, the modeling solution can be solved for every time step such that within each time step, the system is considered in a steady-state condition. The wall temperature values from the previous time

step can be carried over to the next step to determine new heat transfer values.

Both the lumped capacitance and thermal resistance methods include features of interest for modeling SparkJet heat transfer. Therefore, these techniques are combined and a representative thermal circuit is used to model the thermal heat transfer and monitor the wall temperature. The general sequence of heat transfer begins with convection from the cavity air to the interior cavity surfaces. Convective heat transfer is then followed by parallel thermal conduction through the cavity materials and completed by thermal convection from the exterior SparkJet surfaces to the ambient air temperature. The thermal energy source is represented electrically by an ideal voltage source.

The cavity air temperature is represented by the equivalent voltage, T_A. This value will be used to link the thermal model to the fluid dynamic model described in the previous sections. The only means of heat transfer from the air to the Macor and tungsten is through thermal convection, which is represented by a resistor, $R_{h,in}$. The voltage labeled as $T_{w,in}$ represents the interior wall temperature, assuming the wall temperature of the Macor and tungsten are equivalent. The Macor has a thermal capacitance represented as C_M. The thermal conduction through the Macor and tungsten is represented by two parallel thermal resistances, R_M and R_W, respectively. The voltage labeled as $T_{w,out}$ represents the exterior wall temperature. With the exterior wall temperature and ambient air temperature known, the final thermal heat transfer mechanism, thermal convection, is represented as a resistor, $R_{h,out}$. All thermal heat transfer mechanisms ultimately reach electrical ground or, T_∞, the ambient air temperature.

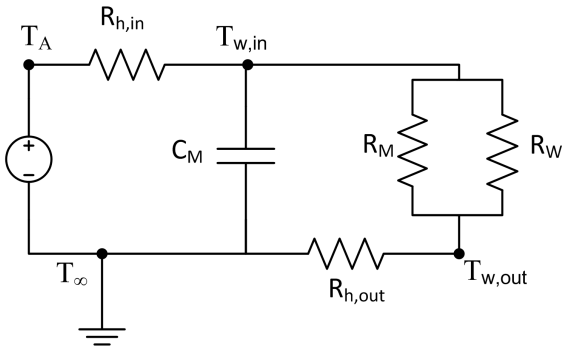

Figure 3.2: Electrical representation of the thermal heat transfer process for the SparkJet actuator.

Once the thermal circuit has been defined, the equivalent thermal resistance and capacitance of the Macor and tungsten need to be determined. The thermal resistance of Macor and tungsten are given by

$$R_M = \frac{L_M}{k_M A_M} \tag{3.31}$$

and

$$R_W = \frac{L_W}{k_W A_W}, \tag{3.32}$$

respectively. The thermal resistances associated with convective heat transfer on the inside and outside of the SparkJet device are given by

$$R_{h,in} = \frac{1}{h_{in} A_{in}} \tag{3.33}$$

and

$$R_{h,out} = \frac{1}{h_{out} A_{out}}, \tag{3.34}$$

respectively. The ability of a material to store thermal energy is represented by an equivalent capacitance. Here, only the thermal capacitance of the Macor, given by

$$C_M = \rho_M v_M C_p, \tag{3.35}$$

is considered as the thermal capacitance of the tungsten electrodes is small due to their small volume. With all of the circuit components defined,

$$\frac{T_A - T_{w,in}}{R_{h,in}} = C_M \frac{dT_{w,in}}{dt} + \frac{T_{w,in} - T_\infty}{R_{h,out} + \frac{1}{\frac{1}{R_M} + \frac{1}{R_W}}} \tag{3.36}$$

is used to solve for the wall temperature.

Another separate method for estimating SparkJet heat transfer is representing the differential form of the heat equation with finite difference equations. This method provides the most spatially and temporally accurate representation of the thermal effects involving the SparkJet cycle. However, this method can be more computationally time consuming. To maintain some level of simplicity the exact SparkJet Macor shape is not modeled but a single line through a side wall is analyzed. Due to the cylindrical shape of the SparkJet cavity and surrounding walls, the heat equation is analyzed in cylindrical coordinates as given by

$$\frac{\partial T}{\partial t} = \alpha \frac{\partial^2 T}{\partial x^2} = \frac{\alpha}{r} \frac{\partial}{\partial r} \left(r \frac{\partial T}{\partial r} \right) = \alpha \frac{\partial^2 T}{\partial r^2} + \frac{\alpha}{r} \frac{\partial T}{\partial r}, \tag{3.37}$$

where

$$\alpha = \frac{k_M}{\rho_M C_{p,M}} \tag{3.38}$$

represents the thermal diffusivity.

For this work, discretization of the partial differential heat equation is accomplished by using explicit first-order, forward-difference discretization in time and second-order, central-difference discretization in space. The discretized time rate of change in temperature is given by

$$\frac{\partial T}{\partial t} = \frac{T_i^{j+1} - T_i^j}{\Delta t} \tag{3.39}$$

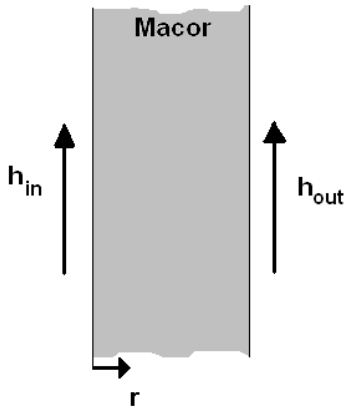

Figure 3.3: Sketch of the thermal heat transfer modeled using finite difference equations

and the discretized radial rate of change in temperature is given by

$$\alpha\frac{\partial^2 T}{\partial r^2}+\frac{\alpha}{r}\frac{\partial T}{\partial r}\approx\alpha\frac{T_{i+1}^{j}-2T_{i}^{j}+T_{i-1}^{j}}{\Delta r^2}+\frac{\alpha}{r_i}\frac{T_{i+1}^{j}-T_{i}^{j}}{\Delta r}. \tag{3.40}$$

This discretization solves for the conductive heat transfer through the interior of the SparkJet walls at time step j and mesh point i. Separate equations are used to approximate the heat equation at the boundaries which involve the convective heat transfer as well.

To solve for the internal mesh points, the above equations are combined into

$$\frac{T_{i}^{j+1}-T_{i}^{j}}{\Delta t}=\alpha\frac{T_{i+1}^{j}-2T_{i}^{j}+T_{i-1}^{j}}{\Delta r^2}+\frac{\alpha}{r_i}\frac{T_{i+1}^{j}-T_{i}^{j}}{\Delta r}, \tag{3.41}$$

which is the discretized form of the cylindrical heat equation. At the boundaries, however, the effects of convection are taken into account. The internal boundary condition is given by

$$hA\left(T_{A}^{j}-T_{i=1}^{j}\right)+kA\frac{T_{i=2}^{j}-T_{i=1}^{j}}{\Delta r}=\rho AC\frac{\Delta r}{2}\frac{T_{i=1}^{j+1}-T_{i=1}^{j}}{\Delta t} \tag{3.42}$$

and the external boundary condition is given by

$$hA\left(T_{\infty}^{j}-T_{i=M}^{j}\right)+kA\frac{T_{i=M}^{j}-T_{i=M-1}^{j}}{\Delta r}=\rho AC\frac{\Delta r}{2}\frac{T_{i=M}^{j+1}-T_{M}^{j}}{\Delta t}. \tag{3.43}$$

The highly unsteady nature of the SparkJet thermal heat transfer requires very small time steps in this simulation. In general, small time steps require small grid spacing to maintain numerical stability, especially when using an explicit method. To perform the stability analysis, all terms in Equation 3.41 at time step j and mesh point i are collected and set to be greater than or equal to zero, which results in the inequality

$$1-2\alpha\frac{\Delta t}{\Delta r^{2}}-\alpha\frac{\Delta t}{\Delta r^{2}}\frac{\Delta r}{r_{i}}\geq 0. \tag{3.44}$$

Solving for Δt,

$$\Delta t\leq\frac{1}{\alpha\Delta r\left(\frac{2}{\Delta r}+\frac{1}{r_{i}}\right)} \tag{3.45}$$

gives the maximum allowable time step for numerical stability. The mesh spacing, Δr, is given while the radius of each mesh point, r_i, is chosen to minimize Δt which corresponds to the radius of the SparkJet cavity.

To compare the two thermal modeling methods for the SparkJet cycle, a notional temperature profile, T_n, was applied to the internal wall. A negative exponential function of a magnitude of 2000 K,

$$T_{n}=\left(2000-T_{\infty}\right)e^{-2000t}+T_{\infty}, \tag{3.46}$$

mimics a typical SparkJet cavity air temperature profile. For comparison, the internal wall temperature, $T_{w,in}$, was monitored using both methods. Figure 3.4 shows the notional temperature profile as a function of time. Also for comparative pur-

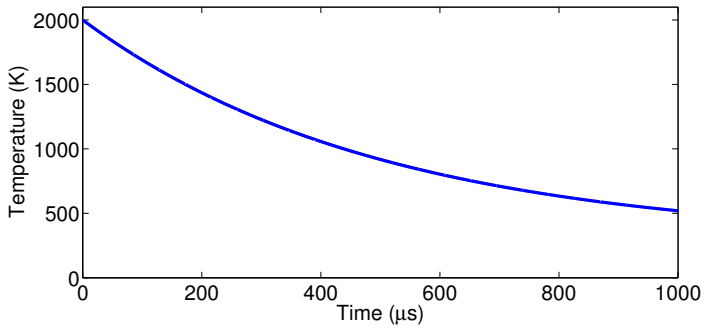

Figure 3.4: Temperature profile used to compare the combined thermal resistance and capacitance method and the discretization method

poses, both thermal modeling methods model heat transfer though an infinitely long hollow Macor tube.

Figure 3.5 shows the wall temperature response to the notional temperature profile shown in Figure 3.4 over 1000 μs. Initially, the wall temperature, $T_{w,in}$, rises quickly and then reaches an asymptotic value of 288.01 K. Surprisingly, the peak wall temperature is not significantly above the initial wall temperature of 288 K. Based on these results, an isothermal wall condition at 288 K may be sufficient for modeling the thermal heat transfer during a single SparkJet cycle. However, when considering multiple SparkJet cycles, recall that the wall temperature does not equal the ambient wall temperature at 1000 μs. When modeling high-frequency actuation, the wall temperature rise can become more significant. Figure 3.6 shows the wall temperature response over 50 cycles at 1 kHz. The wall temperature steadily increases with each cycle but the total temperature rise is still less than 1 K such that an isothermal wall condition may still be sufficient.

Figure 3.7 shows the spatial and temporal response of the cylindrical Macor

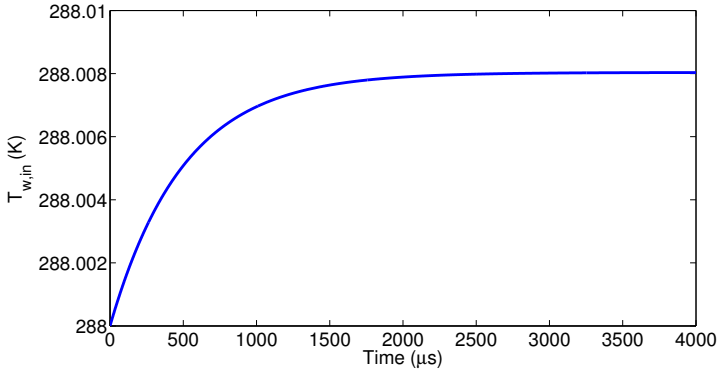

Figure 3.5: Wall temperature response to the notional temperature profile using the combined thermal capacitive and resistive model.

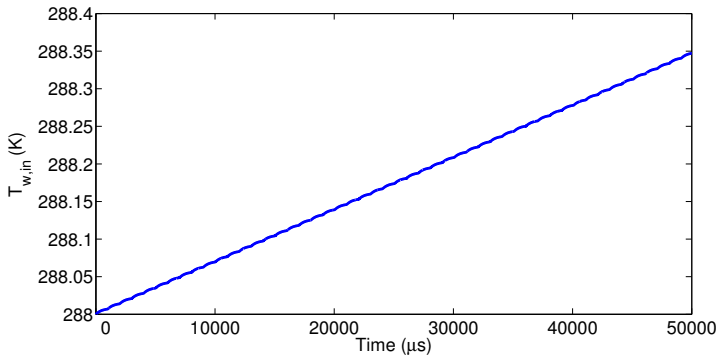

Figure 3.6: Wall temperature response to the notional temperature profile simulating 1 kHz actuation over 50 cycles.

walls to the notional temperature profile using the finite-difference equations. During a single cycle, the temperature at the surface rises quickly and then more slowly decreases toward room temperature. Note, however, that the wall temperature only rises to a couple degrees above room temperature which compares well with the simplified thermal model. As time increases, the wall temperature decays but the interior temperature distribution rises as the thermal energy diffuses into the Macor. Also note that the thermal diffusion does not penetrate far into the Macor. In fact, the outer wall temperature rise is negligible and external thermal convection is irrelevant.

When considering the thermal effects over several SparkJet cycles, the internal wall temperature remains above the atmospheric temperature. Therefore, subsequent cycles will gradually raise the internal wall temperature such that prolonged cycles will result in a significant temperature rise as seen in Figure 3.8. Specifically, Figure 3.8(a) shows the wall temperature as a function of time and Figure 3.8(b) shows the internal Macor temperature at several instances. Together, these plots show that the Macor at the wall and internally increase with each SparkJet cycle. However, the total temperature rise is only 14 K. Based on these results, a single SparkJet cycle can be modeled with an isothermal wall boundary condition without sacrificing modeling fidelity. However, for high-frequency actuation, detailed thermal modeling is recommended.

Regardless of the method used to model heat transfer, defining the convective heat transfer coefficient remains a challenge. Inside the SparkJet cavity, unsteady pressure waves generate a forced convection condition while free convection exists

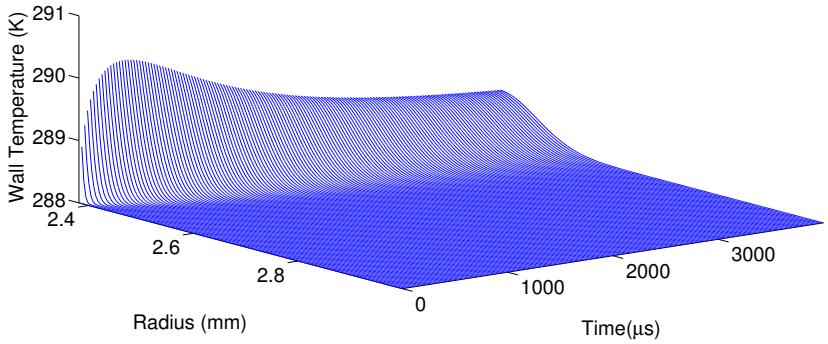

Figure 3.7: Time and space dependent thermal response of the Macor material to the notional temperature profile applied to the internal wall of the Macor during a single cycle.

outside the SparkJet walls. The convective heat transfer coefficient can be estimated based on Reynolds number, Prandtl number, and Nusselt number. However, these estimations describe convective heat transfer in relatively steady flows, which is not the case inside the SparkJet cavity where unsteady pressure oscillations exist. As a result, a convective heat transfer coefficient of 125 W/m^2 is used based on comparison to the CFD simulation discussed in the next section [55].

Considering the original thermal modeling goal of balancing fidelity with simplicity, the thermal model selected to be used with the fluid dynamic portion of the SparkJet 1-D model is the combined capacitive and resistive model. Both models show a wall temperature increases of less than 10 K even over several cycles, which is a small temperature rise compared to the expected cavity temperature rise. The following sections will show that the SparkJet momentum throughput reaches a steady-state value over 3-30 cycles. The previous plots showed that over 50 cycles,

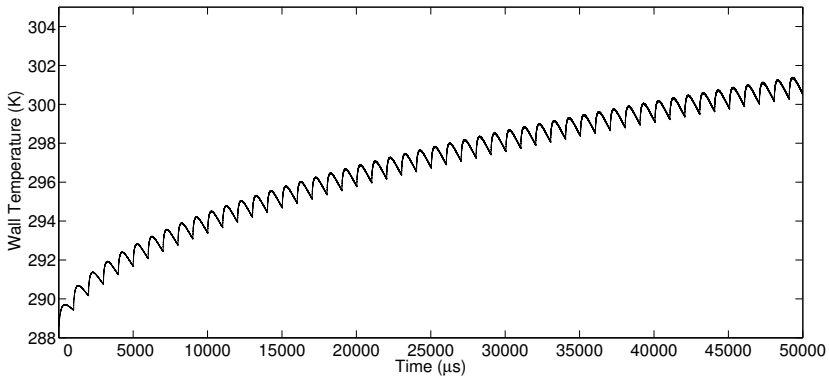

(a) Wall temperature versus time.

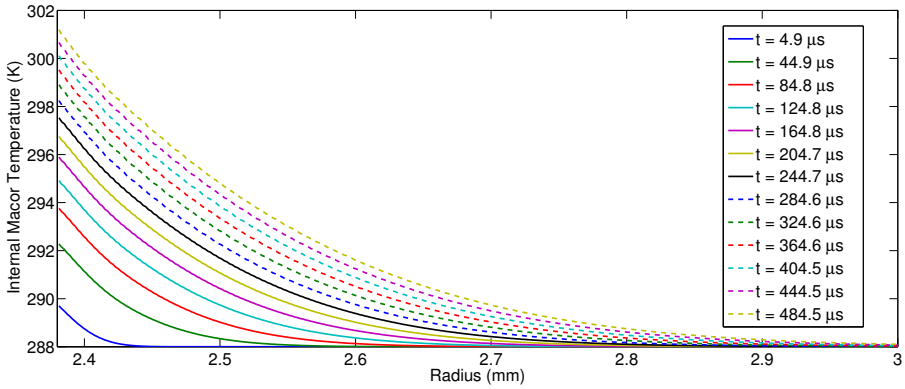

(b) Sample internal temperature distribution versus radius at various time steps.

Figure 3.8: Time and space dependent thermal response of the Macor material to the notional cavity air temperature profile applied at a frequency of 1 kHz over 50 cycles.

the wall temperature rises to only a few degrees above 288 K. While the finite difference modeling reveals some interesting thermal trends and phenomena, the simpler method best satisfies the modeling goal of this dissertation.

3.3 Single Cycle Simulation

The system of equations described in the previous sections were solved using the initial value problem solver in MATLAB called ode45. The MATLAB code used to run the simulations is presented in the Appendix. The ode45 solver is based on the explicit Runge-Kutta numerical approximation method designed to solve a set of variables as a function of a single variable, time in this case. The simulation requires multiple input parameters to properly represent an actual SparkJet cycle and its physical design. These parameters include ambient pressure, temperature, and density; cavity volume (excluding orifice volume); orifice diameter and height; stored capacitor energy; specific heat capacity for a fixed volume of air; and the gas constant of air. If considering the conductive thermal losses, thermal properties of the SparkJet cavity materials and electrodes are also required. To demonstrate this 1-D analytical model, Table 1 provides values for the required inputs. These values were specifically chosen for comparison with pre-existing CFD simulations of the SparkJet actuator interacting with quiescent flow [60]. The CFD simulation only modeled convective heat transfer to an isothermal wall so the physical properties of Macor and tungsten are not included in Table 3.1.

Figure 3.9 shows the time history of the cavity pressure, temperature, and den-

sity as well as the orifice velocity during Stages 1 and 2 and the beginning of Stage 3. The cavity pressure and temperature is instantly increased as a result of Stage 1. During Stage 2, the pressure and temperature start to decrease toward ambient conditions and the cavity density decreases as mass exits the orifice. The velocity of the flow through the orifice remains fairly constant when the flow is choked. The slight decrease in choked flow velocity is due to the decreasing temperature and, therefore, speed of sound. The slope of the velocity curve changes near 200 μs when the flow becomes unchoked. As cavity pressure nears ambient pressure, the velocity decreases toward zero and the cavity density reaches a minimum. Stage 3 starts when the velocity reaches zero. During Stage 3, the flow velocity through the orifice is negative indicating the external flow is being drawn into the cavity. As a result, the cavity density starts to increases and the cavity temperature decreases more rapidly reaches ambient temperature. Figure 3.10 shows the full cycle ending when all cavity conditions have returned to ambient conditions.

To support the modeling assumptions related to viscosity, convective heat transfer, choked jet flow, and one-dimensionality of pressure, temperature, density and velocity, the numerical modeling results are compared to the CFD simulation results previously shown in Figure 3.12. For the specific case of a SparkJet under the conditions given in Table 3.1. The details of the CFD simulation are described in Reference [55] and are, therefore, only summarized here.

The CFD++, URANS simulation was run axisymmetric and 2nd order accurate in time and space using a thermally perfect single air species. A cubic k-ϵ turbulence model was used with an isothermal 288 K solve-to-the-wall boundary

Table 3.1: Design parameters for numerical model used for comparison to CFD results.

Parameter	Value	Units
P_∞	101325	Pa
T_∞	288	K
R	287.15	J/kg-K
C_v	716.85	J/kg-K
v	42.4	mm^3
d_o	1.0	mm
h_o	0.5	mm
Q	0.089	J
h_{in}	125	W/m^2K

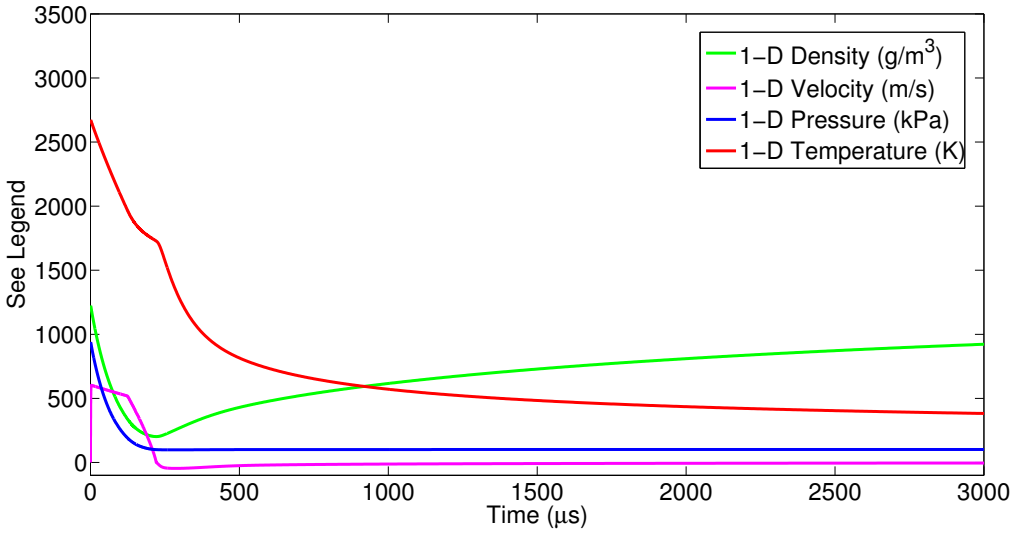

Figure 3.9: Simulation of the time-dependent variation in the cavity pressure, cavity temperature, cavity density, and the velocity through the orifice during early portion of the SparkJet cycle.

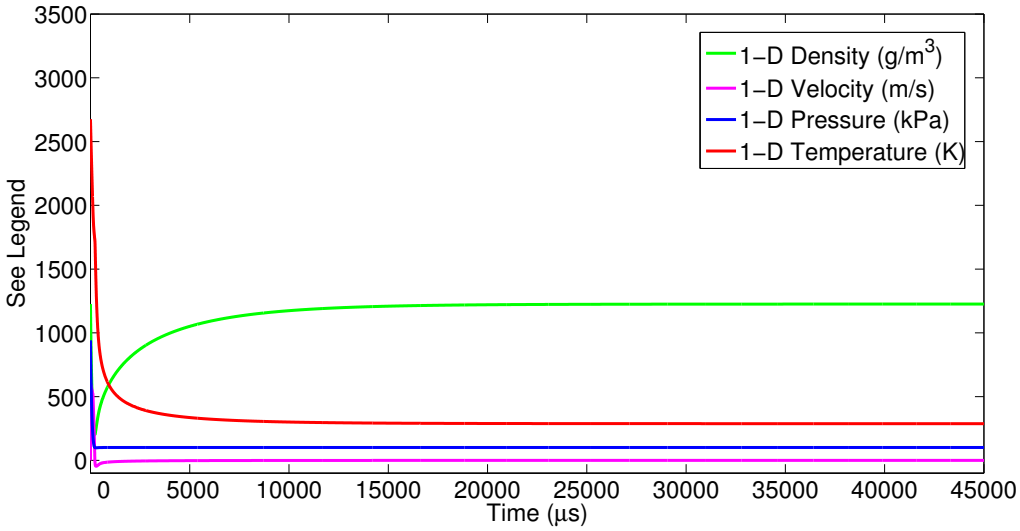

Figure 3.10: Simulation of the time-dependent variation in cavity pressure, cavity temperature, cavity density, and the velocity through the orifice for the entire SparkJet cycle. Note that cavity temperature, pressure, and density have returned to original ambient conditions as given in Table 3.1.

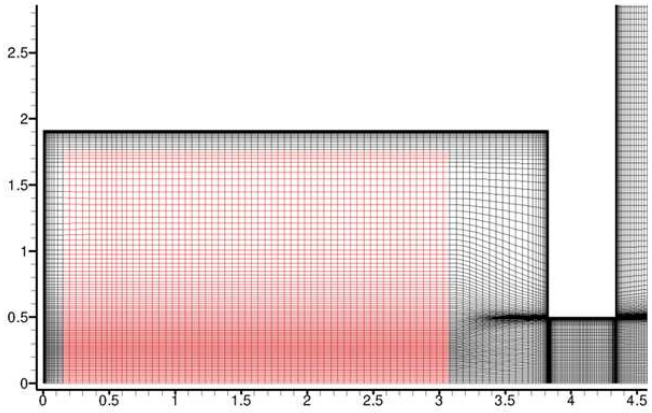

Figure 3.11: Structured, axi-symmetric grid representation of the SparkJet internal geometry with grid axis units in millimeters. The red section represents the grid cells raised to an elevated temperature and pressure to represent the energy deposition in Stage 1.

condition. Figure 3.11 shows a zoomed view of the grid in the SparkJet cavity, throat and external flow.

Relatively short duration ($\approx 500\ \mu s$) simulations, focused on the initial pressure rise, were conducted over a range of energy deposition efficiencies and ended near the start of the refresh cycle. The red section of the grid in Figure 3.11 was initialized separately from the rest of the flow-field and it is about 65% of the cavity volume. The flow was initialized at rest, a temperature of 288 K and a pressure of 101325 Pa. The red section of the grid was kept at the same density and at rest but was increased in pressure and temperature to model Stage 1 of the SparkJet actuation cycle. Once the initial conditions were defined, the solution was run time-accurate. A separate boundary condition family was created at the base of the cavity that was the width of the experimental dynamic pressure sensor to be described in

Chapter 4. Comparisons to the experimental data are discussed in Chapter 5.

Comparison to the 1-D model is also achieved by calculating the volume-averaged pressure, temperature, and density in the cavity as well as the area-averaged velocity in the throat. Figure 3.12 shows these time-dependent values as a result of the CFD simulation. After the initial pressure and temperature rise, the orifice velocity increases, which leads to the decrease in cavity density. As the jet flow continues, the pressure and temperature also decrease. The slope change in the velocity around 120 μs, is indicative of the transition from choked to unchoked flow through the orifice. Once the velocity reaches zero, the refresh stage starts as is visible by the gradual increase in cavity density. As the density increases, the relatively cool air is drawn into the cavity, which quickly decreases the cavity temperature. The cavity pressure remains just below ambient pressure which forces the refresh stage to continue. The pressure gradient is primarily maintained by the continued convective heat transfer at the walls.

The 1-D model and CFD results are compared in Figure 3.13. This figure shows that the overall comparison between the pressure, temperature, density, and velocity curves are quite good. The largest disparities occur at the beginning of the SparkJet cycle and are likely due to the highly unsteady flow present in the cavity and orifice as the jet formation begins. However, as the cycle continues, the two modeling solutions merge. This comparison does not necessarily prove the assumptions but certainly supports them. With this level of support in the initial 1-D model development, the model is expanded to high-frequency actuation.

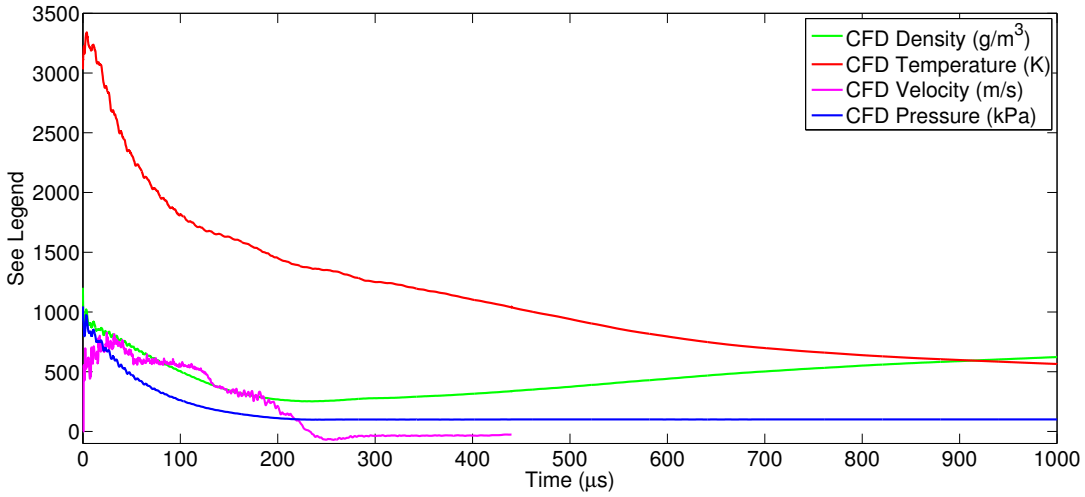

Figure 3.12: Time-dependent CFD simulation of the volume-averaged cavity pressure, temperature, and density and area-averaged jet velocity through the orifice.

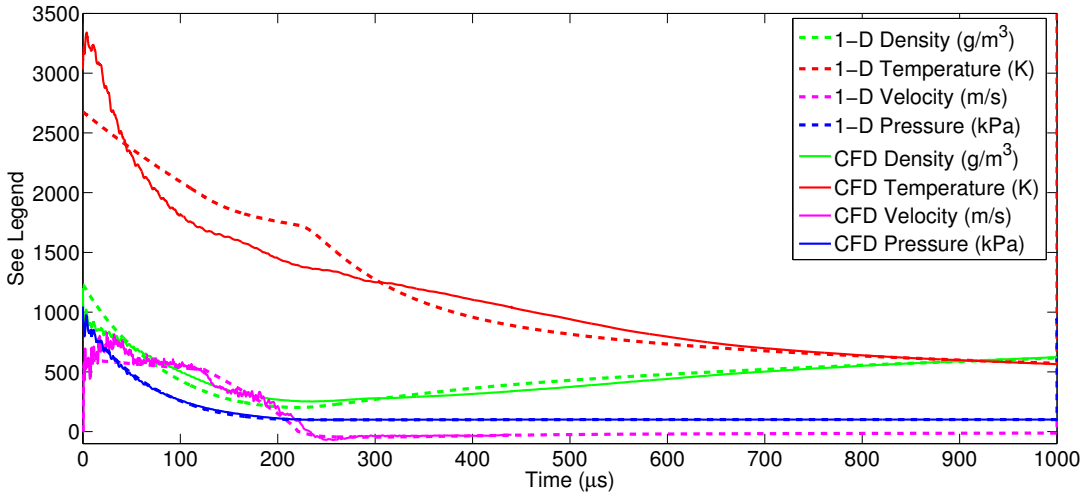

Figure 3.13: Comparison of the cavity pressure, temperature, and density and orifice velocity versus time based on the CFD simulations and the simplified numerical model.

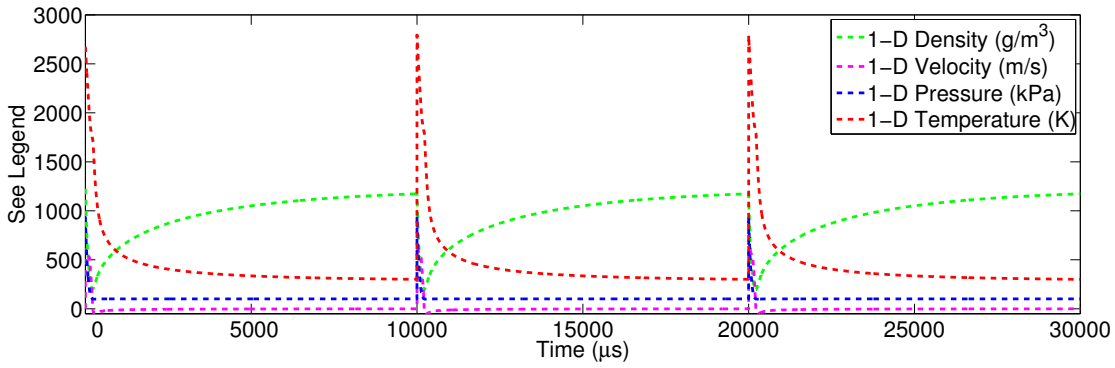

Figure 3.14: Simulation of the time dependent variation in cavity pressure, temperature, and density and the velocity through the orifice for three SparkJet cycles at 100 Hz.

3.4 Simulating High-Frequency Actuation

As discussed in Chapter 1, most AFC techniques involve actuation at frequencies matching, or at a harmonic of, a natural instability in the flow. This model was modified to study the effect of high-frequency actuation on SparkJet performance. Based on a prescribed actuation frequency, the ODE solver is exited at the time step corresponding to the beginning of the next actuation cycle. The cavity pressure, temperature, density, and orifice velocity become the initial conditions for the next cycle and the ODE solver is restarted. Each cycle is initiated with the same value of Q_C. Figure 3.14 shows the variation in cavity pressure, temperature, and density and the velocity through the orifice when the SparkJet is actuated under the same conditions listed in Table 1 at 100 Hz. Figure 3.14 demonstrates the effect of high-frequency actuation on SparkJet performance. Even at 100 Hz, the model shows that the second cycle encroaches on the end of Stage 3 of the first cycle such that

the peak temperature for the second cycle is slightly higher than that of the first cycle. This increase in peak temperature is indicative of the effect of a very slow, unassisted refresh cycle. Because momentum is an important performance parameter for AFC devices, Figure 3.15(a) shows that the effect on momentum is visible but not significant for an actuation frequency of 100 Hz. However, as frequency is increased, this effect is even more evident as shown in Figure 3.15(b) when the SparkJet actuation frequency is modeled at 1 kHz and 5 kHz. When the simulation is run over a range of frequencies from 1 Hz to 10 kHz, the steady-state momentum, normalized by the peak momentum of the first cycle, can be plotted as a function of frequency as shown in Figure 3.16. The normalized steady-state momentum output remains constant until approximately 100 Hz and decreases as frequency increases above 100 Hz.

The dependence of the normalized, steady-state momentum due to design parameters such as orifice diameter, cavity volume, and Q_C are analyzed using the model. Figure 3.16 shows that increasing the orifice diameter allows for higher momentum throughput as frequency increases. However, all three diameters are subject to a decrease in momentum throughput around 100 Hz. Figure 3.17 shows that increasing the input energy does not affect the high-frequency, normalized, momentum-based performance. As Q_C increases, the pressure gradient across the orifice face during Stage 2 increases, which drives the jet velocity up. Additionally, the increased cavity temperature allows for a higher jet velocity associated with choked flow. During the transition from Stage 2 to Stage 3, the increased jet velocity results in a larger decrease in the cavity pressure as jet momentum over-exhausts

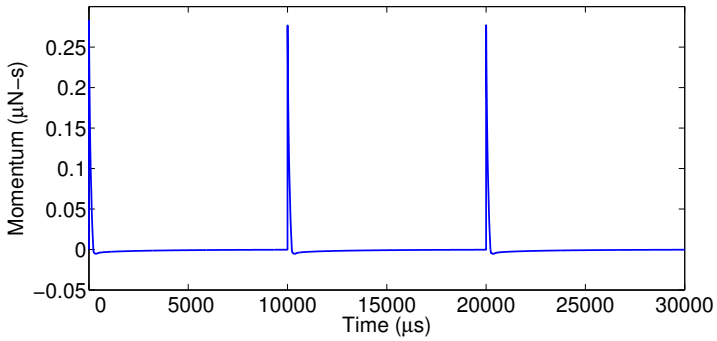

(a) 100 Hz.

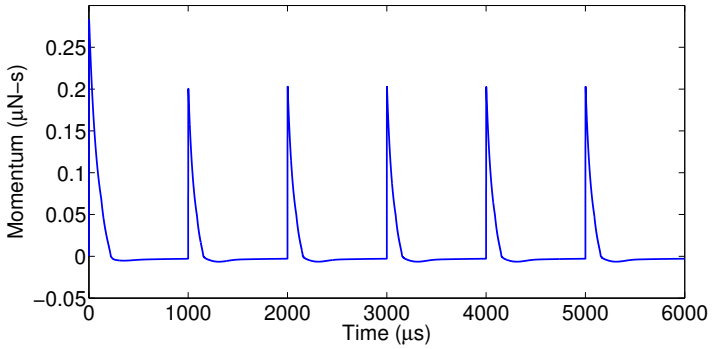

(b) 1000 Hz.

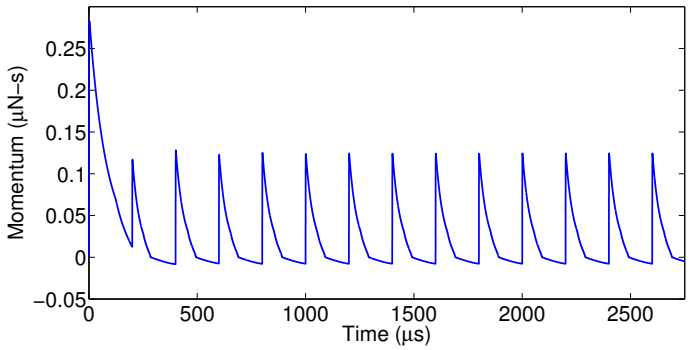

(c) 5000 Hz.

Figure 3.15: Simulation of the momentum through the SparkJet orifice as a function of time when operated at 100, 1000 and 5000 Hz.

the cavity. Again, a relatively larger pressure gradient across the orifice at the beginning of Stage 3 leads to a higher intake velocity. As a result of these phenomena, the durations of Stage 2 and Stage 3 are not significantly influenced by variation in Q_C. Only the magnitudes of the cavity pressure, temperature, density, jet velocity and jet momentum are affected. Figure 3.18 shows that increasing the cavity volume decreases the high-frequency momentum-based performance of the actuator. Taking each of these trends into consideration, the high-frequency performance is improved by design parameter changes that essentially shorten the duration of the complete SparkJet cycle. Unfortunately, the high-frequency results are not validated against CFD or experimental results and future work toward validation is desired. Therefore, the quantitative rollover frequencies shown in Figures 3.16-3.18 require further support.

3.5 Summary

This chapter defined the control volume of interest for SparkJet analysis and presented the governing equations utilized to develop the 1-D model of the SparkJet cycle. Several assumptions were made in the development of the model and the validity of most of the assumptions is considered. The model first simulated a complete single SparkJet cycle and was compared to CFD analysis under the same conditions to support several modeling assumptions. The comparison to CFD supported the assumptions that the flow through the orifice can be assumed inviscid, the 2-D axisymmetric flow can be simplified by volume averaging, the process is non-adiabatic

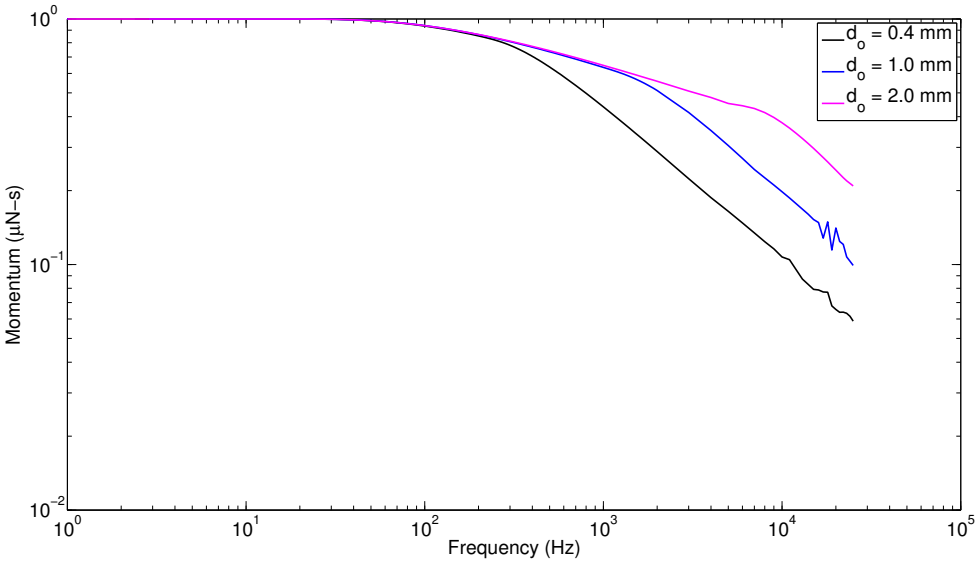

Figure 3.16: Magnitude plot of the normalized, steady-state momentum throughput from the SparkJet actuator operated from 1 Hz to 10 kHz for orifice diameters of 0.4, 1.0 and 2.0 mm, $Q_C = 0.45$ J, and $v = 84.8$ mm^3 as predicted by the 1-D model.

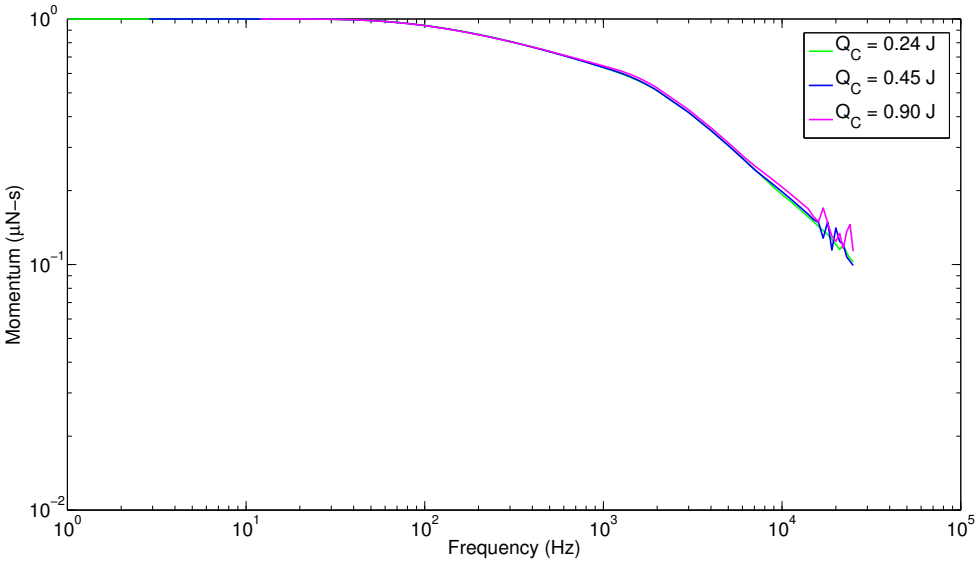

Figure 3.17: Magnitude plot of the normalized, steady-state momentum throughput from the SparkJet actuator operated from 1 Hz to 10 kHz for energy deposition values of 0.24, 0.45 and 0.90 J, $d_o = 1$ mm, and $v = 84.8$ mm^3 as predicted by the 1-D model.

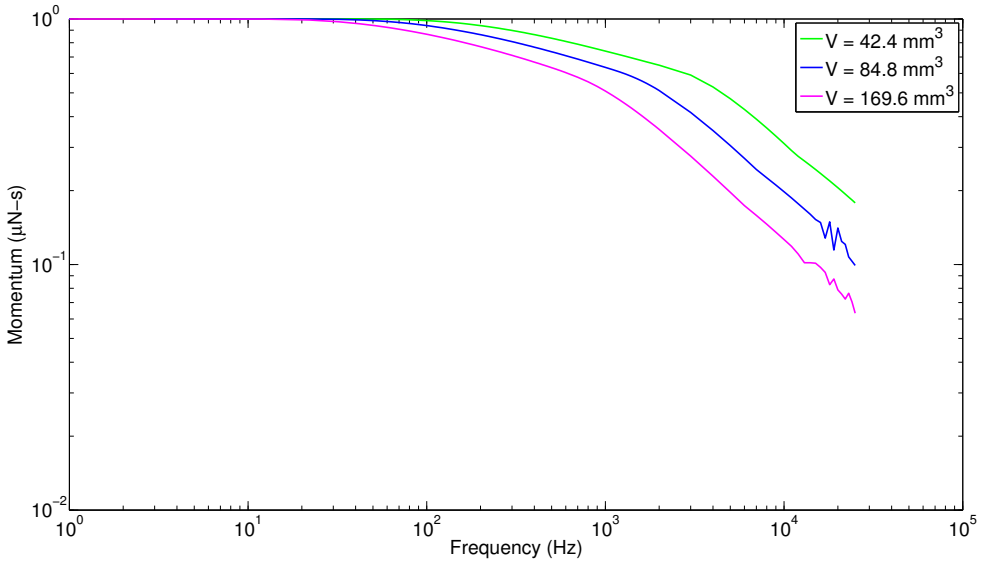

Figure 3.18: Magnitude plot of the normalized, steady-state momentum throughput from the SparkJet actuator operated from 1 Hz to 10 kHz for cavity volumes of 42.4, 84.8 and 169.6 mm^3, $Q_C = 0.45$ J, and $d_o = 1$ mm as predicted by the 1-D model.

and the choked flow condition can be defined with isentropic relations. This model is unique from previous efforts primarily due to the addition of heat transfer which enabled modeling of Stage 3 and high-frequency actuation.

With modest confidence in the SparkJet model, the model was exercised to explore performance at high-frequency actuation. The results illustrate well that, as frequency increases, performance generally suffers when quantified using jet momentum. As the high-frequency actuation demands increase, investigation into improving performance at high-frequency is required. For the SparkJet actuator, this is primarily controlled by reducing the duration of Stages 2 and 3. This can be achieved by reducing cavity volume, or increasing orifice diameter. However, while peak mass flow rate and momentum may be increased, the duration of high-momentum flow is decreased. Another technique is to increase heat transfer from the cavity by using wall materials of a higher thermal conductivity such that the duration of Stages 2 and 3 are decreased.

The following chapters focus on experimental data to determine the validity of the remaining assumptions primarily related to Stage 1. The peak cavity pressure and power drawn by the arc during Stage 1 are used to determine an energy transfer efficiency. Further analysis considers failures in the assumptions to explain the energy losses and changes in efficiency as certain design parameters change.

Chapter 4

Experimental Details and Data Acquisition

While comparison to CFD supports assumptions related to fluid dynamics, the assumptions for energy transfer modeling during Stage 1 require experimental support. A description of the equipment used to power the SparkJet and to acquire data are described in this chapter and an overview of the experimental setup is shown in Figure 4.1. Further details regarding this setup are discussed throughout this chapter. Experimental measurements were primarily acquired to understand the plasma-physics, support Stage 1 modeling, and to examine Stage 2. The design parameters varied to understand the effects on SparkJet performance include cavity volume, orifice diameter, capacitance, and electrode gap. As these parameters were varied, the SparkJet actuator was characterized with simultaneous internal cavity pressure measurements and arc power measurements to quantify SparkJet operation and efficiency.

Prior to this work, experimental efforts were limited and did not provide information on internal SparkJet cavity conditions necessary to support Stage 1 modeling. Therefore, attention was turned to measuring the pressure inside the SparkJet cavity in addition to arc power measurements. The pressure measurements were completed using a high-frequency response, dynamic pressure transducer. The arc power was calculated using the product of current and voltage measurements. These

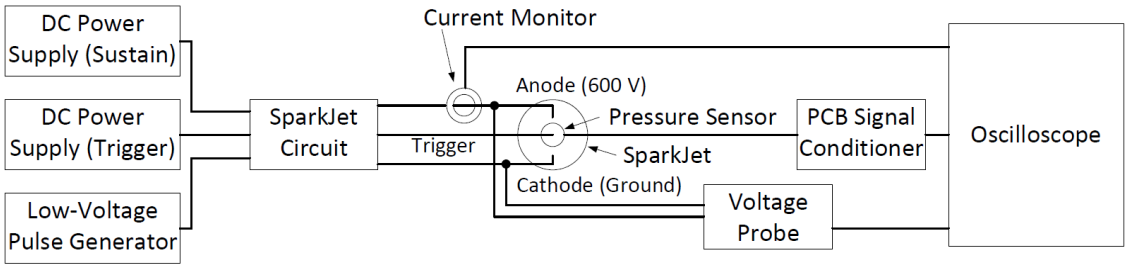

Figure 4.1: Diagram showing the basic electrical connections and equipment used to acquire experimental data and power the SparkJet power supplies.

experiments led to a demonstration of SparkJet performance and estimation of the operating efficiency. This new knowledge led to modifications to Stage 1 modeling and exposed a disparity related to Stage 2 modeling.

4.1 SparkJet Actuator Device

The SparkJet actuator design used to support this dissertation included the use of a Macor housing, tungsten anode and cathode, and a copper trigger electrode. The SparkJet actuator was assembled from two Macor parts identified as a lid and a base. Figures 4.2 and 4.3 show dimensional drawings of the lid and base for a cavity volume of 84.8 mm^3 and orifice diameter of 1 mm. The lids were designed with three slots into which the electrodes could be placed. To characterize the SparkJet operation, several design parameters were varied to analyze the effect on the peak pressure rise in the cavity. These parameters include the orifice diameter, cavity volume, capacitance across the electrodes, and electrode gap.

Figure 4.4 shows a photograph of the variety of Macor SparkJet bases and lids

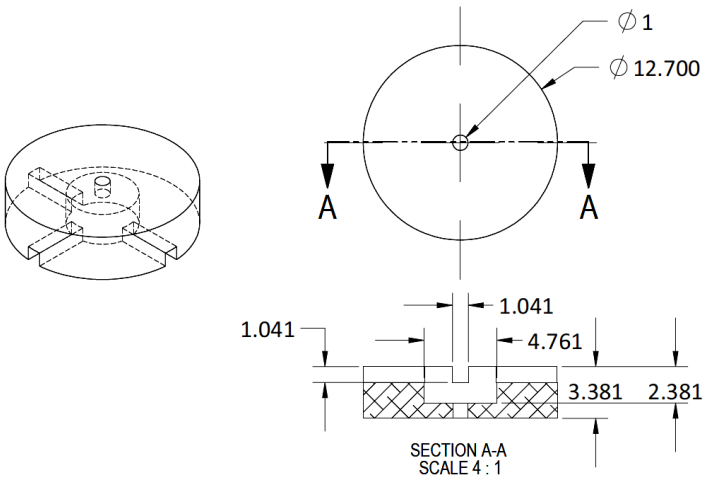

Figure 4.2: Drawing of the SparkJet Macor lid with a 1 mm orifice diameter and 84.8 mm^3 cavity volume.

corresponding to variations in cavity volume (42.4, 84.8, and 169.6 mm^3) and orifice diameter (0.4, 1.0, and 2.0 mm). The top row of white components are the bases and the white components below the bases are the lids compatible with each cavity volume. For a cavity volume of 84.8 mm^3, all three orifice diameters were evaluated. For cavity volumes of 42.4 mm^3 and 169.6 mm^3, an orifice diameter of 1 mm was evaluated. Also, at the top of this image, the metal housing that was inserted into the bottom of the SparkJet base with the pressure sensor installed (small circle in the center of the metal face) are visible. Further details on the sensor and installation are discussed in Section 4.5 in this chapter.

The remaining design parameters were functions of the electrodes or the electronics. The electrode spacing was controlled during the assembly process and measured using a digital micrometer. The electrodes are placed in the pre-machined slots shown in Figure 4.2 and adhered to the Macor using 5-minute epoxy such that

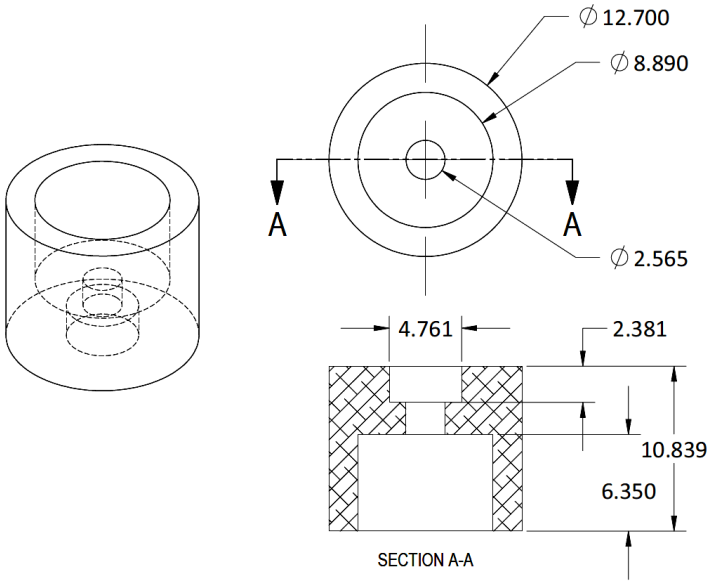

Figure 4.3: Drawing of the base component of the SparkJet for a cavity volume of 84.8 mm^3.

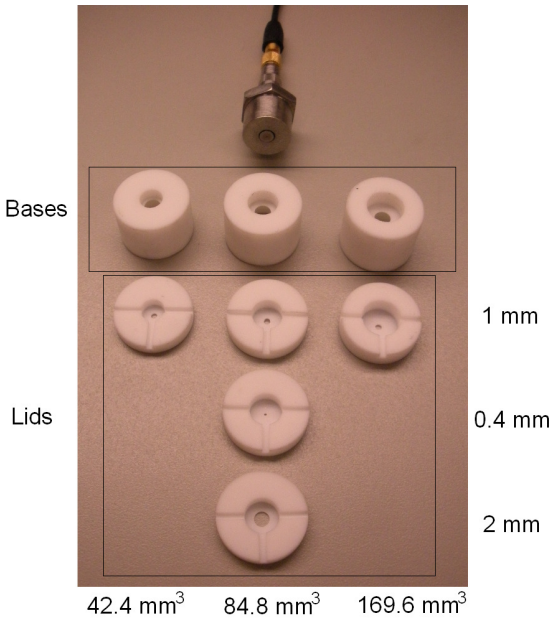

Figure 4.4: Photograph of the SparkJet cavities and lids used to characterize the effect of cavity volume and orifice diameter on SparkJet cavity pressure rise and the pressure sensor used to acquire cavity pressure data.

the anode and cathode tips were approximately equidistant from the center of the SparkJet cavity. This electrode gap was carefully selected to be small enough to ensure SparkJet reliability but large enough to maximize efficiency. The voltage across the electrodes was controlled by an external power supply, but was typically set near 600 V for maximum output energy. The capacitance across the electrodes was controlled by adding or subtracting individual ceramic capacitors (Vishay 820 nF, 630 V) from a bank of capacitors as seen in Figure 4.5. Also note in this photograph that the wires from the capacitor bank to the SparkJet are approximately 0.2 m long. The wires were kept relatively short to help minimize power losses that would otherwise exist in unnecessarily long wires. While the resistance of wires is low, the high current flowing through during the arc discharge results in a voltage drop that reduces the actual voltage potential across the electrode tips and, therefore, the power available to the arc.

4.2 SparkJet Power Supplies

As the SparkJet operation became better understood over the duration of this work, the SparkJet electronics evolved to meet high-frequency demands and improve SparkJet performance. Two circuit designs were used to operate the SparkJet actuator involving an external trigger and pseudo-series trigger. The generic circuit used to generate the majority of the experimental results is shown in Figure 4.6. This circuit is based on an externally triggered arc discharge concept that is rated to 600 V. For the remainder of this dissertation, this circuit is referred to as 600ET.

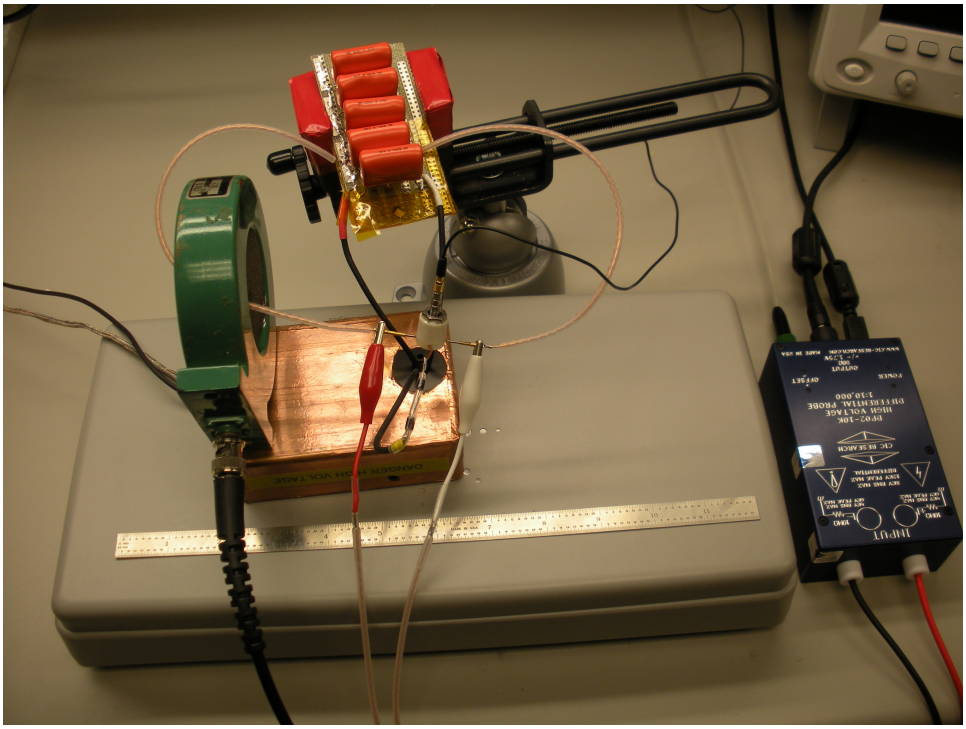

Figure 4.5: Photograph of the SparkJet setup showing the Pearson current monitor, differential voltage probe, installed pressure sensor, the SparkJet actuator, SparkJet power supply, and a 12 inch ruler for scaling.

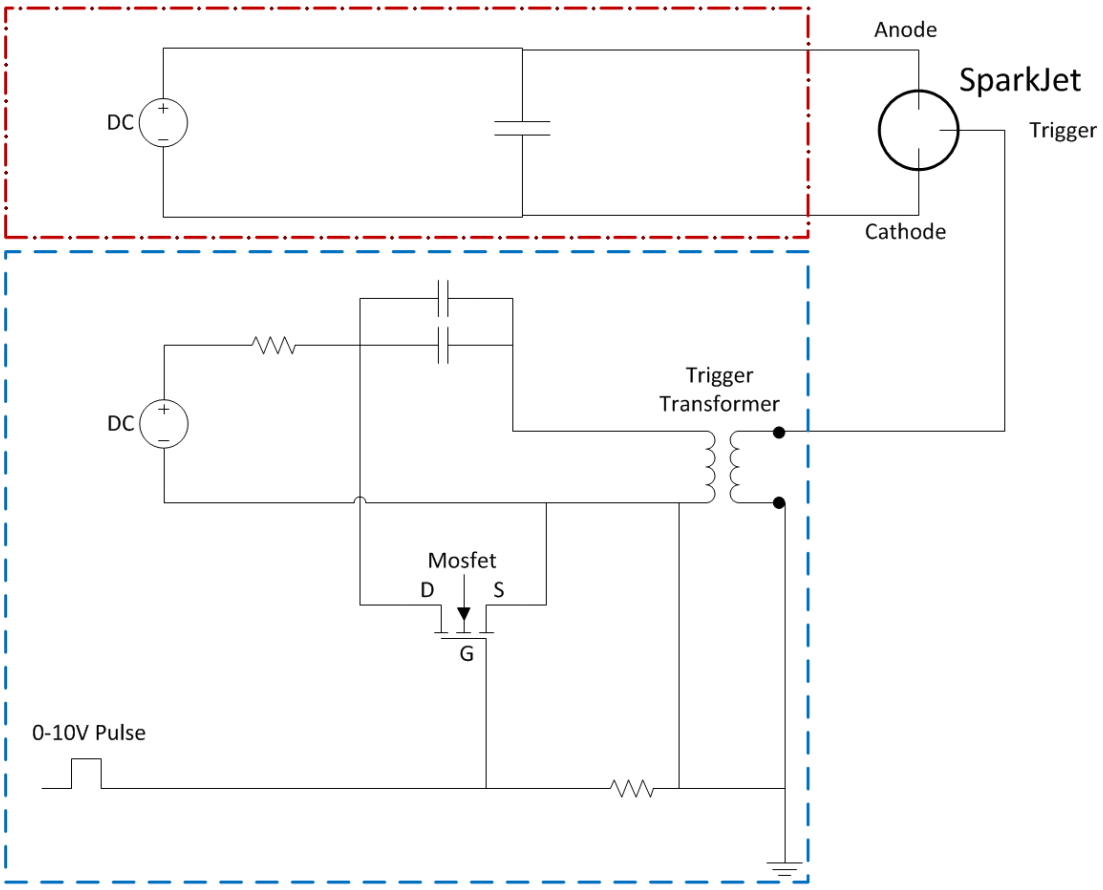

Figure 4.6: Circuit diagram of the 600 V external trigger SparkJet power supply.

The maximum voltage rating of 600 V for the 600ET circuit was chosen for practicality because electrical components rated to 600 V are less expensive and are readily available. A photograph of this power supply is shown in Figure 4.7 to demonstrate the small size of this circuit which is beneficial for aircraft installation.

Based on further understanding of SparkJet performance, the generic circuit shown in Figure 4.8 corresponds to the pseudo-series trigger SparkJet power supply also with a maximum capacitor voltage of 600 V. For the remainder of this dissertation, this circuit is identified as 600PST. Transition to this circuit was motivated by reliability issues. With the intention of improving SparkJet reliability, results

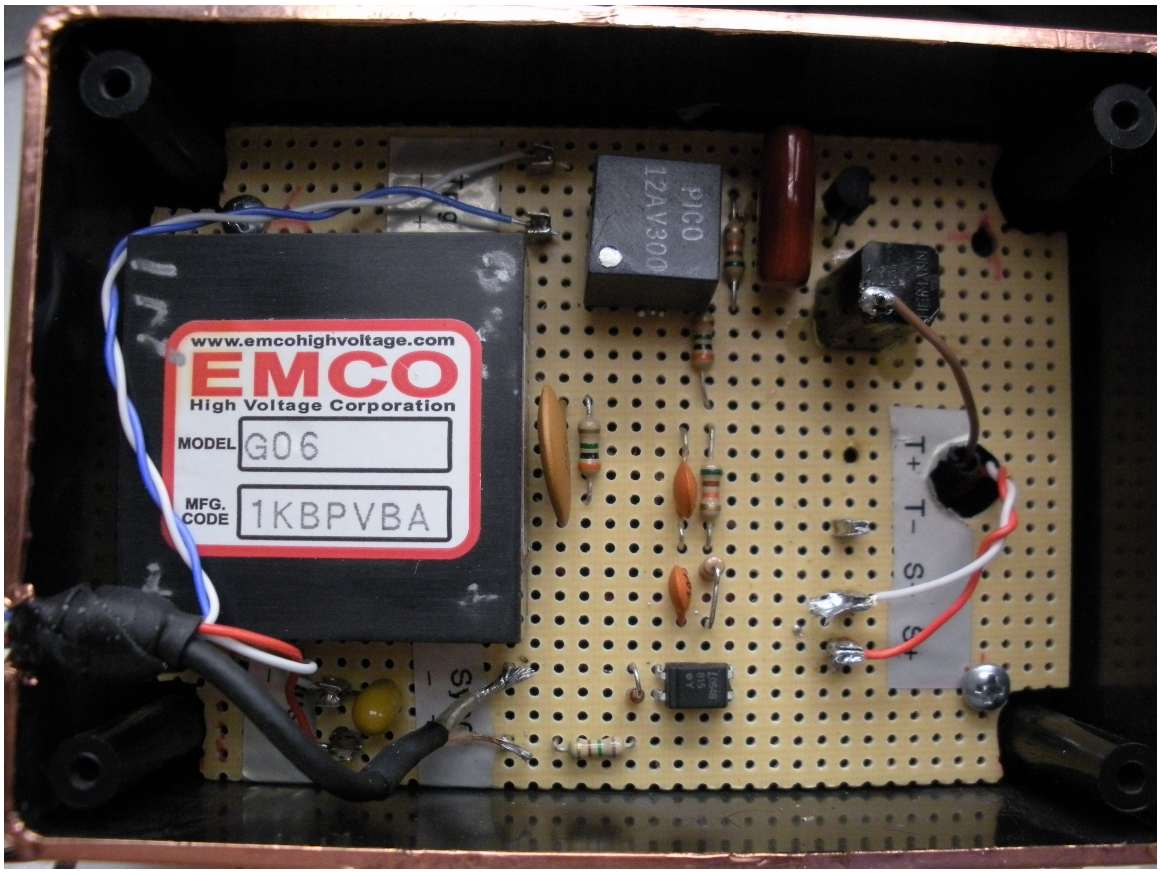

Figure 4.7: Photograph of the 600ET SparkJet power supply circuit box with dimensions of 110 mm x 79 mm x 38 mm.

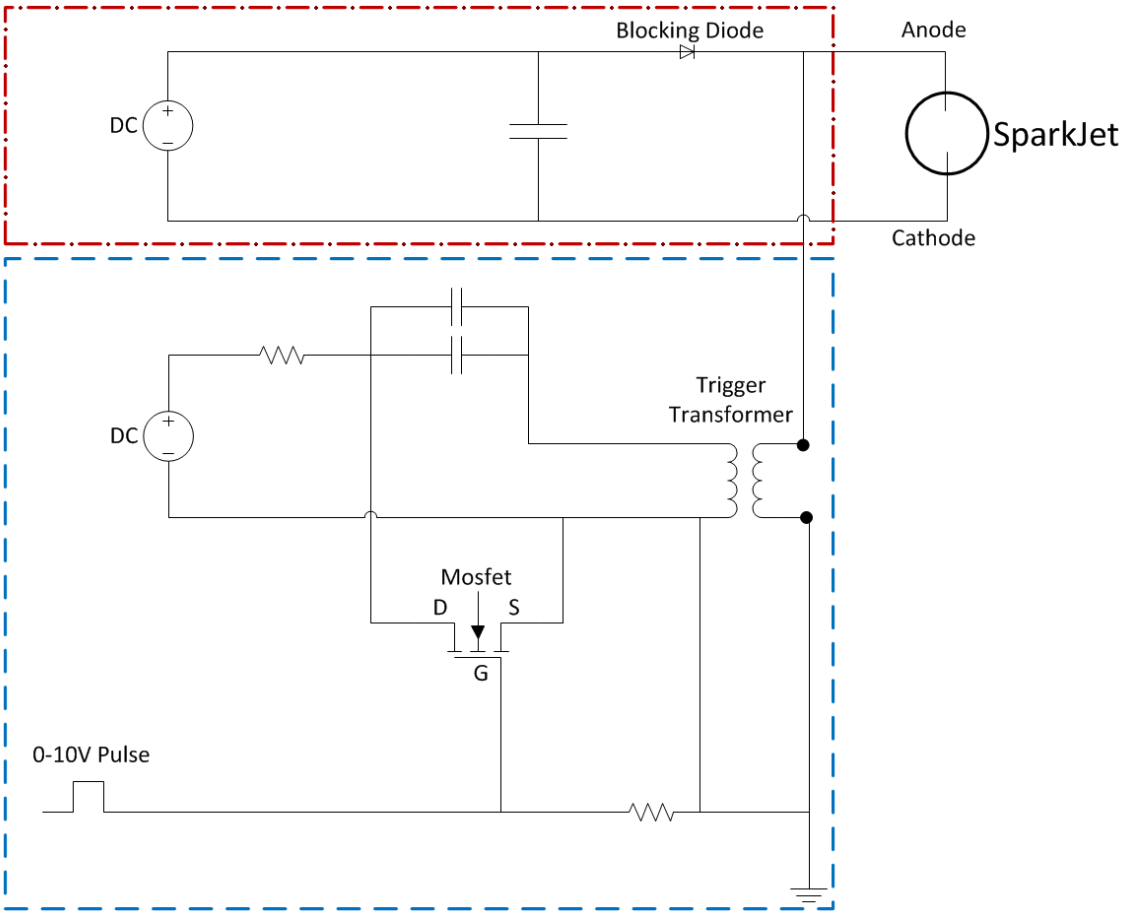

Figure 4.8: Circuit diagram of the 600 V pseudo-series trigger SparkJet power supply.

discussed in Chapter 5 will show that the 600PST circuit had additional efficiency benefits. A photograph of this power supply is shown in Figure 4.9 to demonstrate the small size of this circuit as well.

Basic operation of both of the power supplies is very similar. The SparkJet operates on a triggered capacitive arc discharge; therefore, each SparkJet power supply includes a means of triggering the discharge (trigger circuit) and a bank of capacitors parallel to the SparkJet anode and cathode, which sustains the trigger arc (sustain circuit). The sustain and trigger circuits are identified in Figures 4.6 and 4.8 by a red, dash-dot rectangle surrounding the sustain circuit and a blue, dash

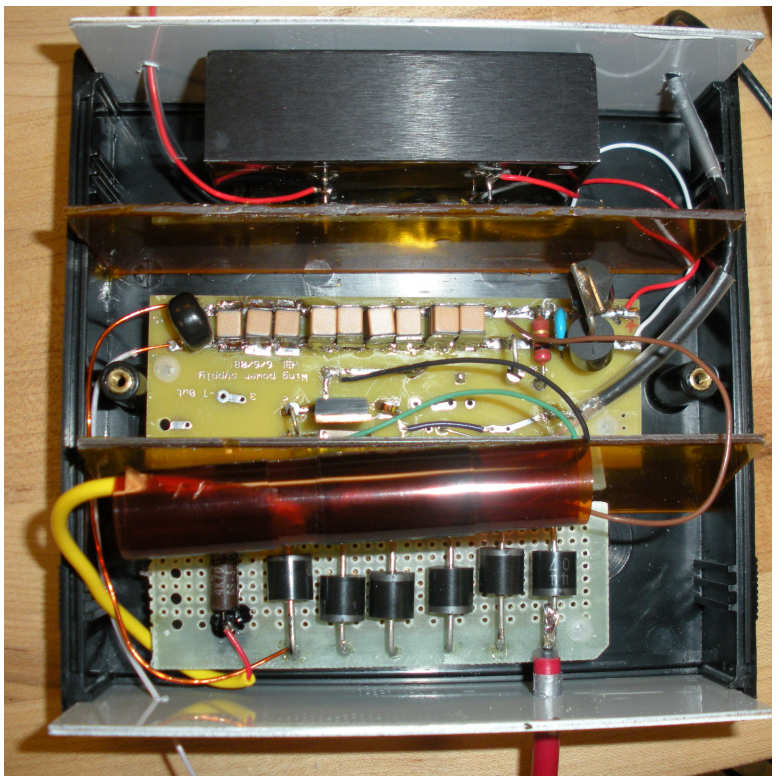

Figure 4.9: Photograph of the 600PST SparkJet power supply circuit box with dimensions of 133 mm x 133 mm x 55 mm.

rectangle surrounding the trigger circuit. Separate DC power sources are typically used to provide power to each section of the SparkJet power supply. An external DC power supply is used to charge the capacitor bank to a set voltage (typically near 600 V). The output current limit of the power supply determines the time required to charge the capacitor bank. Therefore, one determining factor in the frequency limit of the SparkJet is due to the DC power supply current limit. Additional, non-essential electrical components are also placed in parallel with the capacitors such as a resistor for operator safety, a surge suppressor to encourage a "clean" discharge, and diodes immediately before the trigger electrode to prevent an arc discharge from the anode to the trigger electrode.

Separate from the sustain circuit is the trigger circuit. A capacitor is charged by an additional DC power supply and the charging rate is regulated by a resistor. When the SparkJet is triggered, a low-voltage square pulse activates a transistor such that current can flow across it. Once the transistor gate is open, the trigger circuit capacitor begins to discharge across a high-voltage transformer that quickly (≈ 0.5 μs) raises the voltage potential at the trigger electrode tip. If the breakdown voltage between the trigger electrode and cathode is less than the peak trigger voltage (near 10 kV), a trigger spark will form between the trigger electrode and cathode. Subsequently, if the resulting trigger spark locally reduces the breakdown voltage below the electrode voltage, Stage 1 begins as the main capacitor bank discharges across the anode and cathode in the form of an arc. In the case of the pseudo-series circuit, the high-voltage transformer output is connected to the anode but high-voltage, high-current, blocking diodes prevent the high voltage from inter-

acting with the capacitor bank portion of the circuit. Further detail explaining the difference between the external and pseudo-series triggers is provided in the following paragraphs.

The purpose of the trigger spark is to momentarily reduce the local breakdown voltage between the anode and cathode. While using the external trigger circuit, maximizing the triggering reliability resulted in the ideal trigger electrode tip placement as close to the anode as possible without the trigger spark occurring between the trigger electrode and anode. Therefore, the trigger electrode tip was placed approximately half way between the anode and cathode. In addition, the trigger spark only ionizes a portion of the electrode gap. As the gap between the anode and cathode increases, placement of the trigger electrode becomes a delicate and time-consuming process. Because the exact placement varied from SparkJet to SparkJet, the trigger electrode had to be a flexible metal such that copper was typically used. Because copper does not survive the arc environment well, the trigger electrode tip would frequently need to be cleaned and repositioned which further added to the time consumption associated with using an external trigger circuit. In addition, the maximum achievable gap using the external trigger mechanism while maintaining moderately reliable arc breakdown was approximately 1.75 mm. The problems associated with reliability prompted an effort to change the trigger mechanism.

The trigger circuit design change was based on online documentation by Amglo [61] and Perkin Elmer [62] describing methods of causing an arc breakdown for arc lamps. Trigger circuits can be categorized into three types: external, series and pseudo-series. All of these circuit types contain a triggering circuit and a sustain

circuit but differ in the portions of the circuits which overlap. The external trigger circuit, which is used in the 600ET circuit, only overlaps at the electrode gap by sharing a common cathode. The sustain and trigger circuits each have a separate anode. The electrical components in the trigger circuit are rated to tolerate the high-voltage associated with the trigger spark but not the high-current associated with the sustain circuit and vice versa.

In a series trigger circuit, several portions of the circuit overlap such that many of the electrical components in the trigger and sustain circuits experience both high-voltage and high-current including the transformer in the trigger circuit. The most costly consequence of the series trigger circuit is due to the transformer requirement for low gauge wiring making the transformer heavy and bulky. Also, using components tolerant of high-voltage and high-current are more difficult to procure and are generally more costly. Finally, the pseudo-series trigger circuit is a compromise between the external and series trigger circuits such that the sustain and trigger circuits only overlap at the anode and cathode. Sharing the anode requires that high-voltage blocking diodes force the trigger voltage to pass between the anode and cathode rather than into the sustain circuit.

Utilizing the pseudo-series trigger circuit offers both electrical and physical performance benefits over the external trigger circuit. With the pseudo-series trigger circuit, the electrode configuration reduces to two electrodes while maintaining the ability to synchronize with data acquisition equipment. In this design, the trigger spark occurs between the anode and cathode thus reducing the breakdown voltage of the entire gap rather than a portion of it as with the external trigger circuit.

This design feature also increases reliability in producing an arc breakdown and, thus, operating the SparkJet actuator. In addition, removing the dedicated trigger electrode eliminates the time consumption associated with placement. The pseudo-series trigger circuit also allows for flexibility in selecting the electrode gap without sacrificing reliability. In Chapter 5, efficiency benefits as a function of electrode gap are made apparent when measuring the cavity pressure.

4.3 External Supplies

Figure 4.1 shows the basic experimental setup including the equipment used to operate the SparkJet and instruments used to acquire pressure, voltage, and current data. This section describes the external power or voltage supplies in detail. For this work, operating the SparkJet requires a low voltage (0-10 V) square pulse with a pulse width of approximately 40 μs. For the work utilizing the 600ET circuit, a TENMA-72-6860 pulse generator was used to provide this pulse. The pulse generator can operate at a set frequency or using a manual trigger. Because only single pulse data acquisition was acquired from these power supplies, the manual push-button trigger function was used. When triggered, the low voltage pulse is applied to the custom trigger circuit as shown in Figure 4.6. For improved control of high-frequency actuation, the low-voltage pulse controlling the circuit in Figure 4.8 was generated by an Agilent 33521A Function/Arbitrary Waveform Generator. Transition to the function generator resulted from the ability of the function generator to generate a burst of pulses at a desired frequency, which was helpful for high-frequency actuation

on the benchtop. This equipment was used with the 600PST circuit with the purpose of performing high-frequency actuation tests. However, for the tests described in this dissertation, only single pulses were applied to the SparkJet circuits.

Each SparkJet circuit requires DC power sources for charging the capacitors parallel to the SparkJet electrodes and for the high-voltage trigger circuit. The 600ET circuit used a TENMA-72-7245 Dual Channel Bench DC Power Supply to provide power to the trigger and sustain circuits. The TENMA power supply is capable of outputting up to 30 VDC and 3 A per channel. The 600PST SparkJet circuit is powered by a TDK Lambda GEN600-2.6 DC power supply to charge the capacitors and an Acopian U275Y20M Power Supply Module to power the trigger circuit. The TDK power supply is capable of outputting up to 600 VDC and 3 A and the Acopian power supply is capable of outputting up to 275 V and 0.2 A. The high voltage and current output of the TDK power supply was used for the ability to support high-frequency actuation. The output from the Lambda power supply is controlled with two, high-wattage, parallel resistors that also isolate the capacitance within the Lambda power supply from the SparkJet power supply.

4.4 Data Acquisition

The primary instrument used to collect data was an Agilent AT-DSO5014A - 100MHz 4CH portable oscilloscope which monitored the voltage across the electrodes, the pressure sensor output, and the current through the arc at a sampling frequency of 250 MHz. Depending on other required diagnostic testing through the

Figure 4.10: Photograph of the TENMA-72-6860 Pulse Generator used to trigger the 600ET SparkJet circuit.

Figure 4.11: Photograph of the TENMA-72-7245 Dual Channel Bench DC Power Supply used to power the 600ET SparkJet circuit.

Figure 4.12: Photograph of the Agilent Function Generator used to initialize the Spark-Jet cycle for the 600PST circuit.

Figure 4.13: Photograph of the Lambda GEN600-2.6 DC Power Supply and the custom electronics box containing the Acopian power supply that are used to power the 600PST SparkJet circuit.

course of this dissertation work, the fourth channel was used for the low-voltage pulse, a photodetector, trigger voltage measurements, or a single-ended voltage probe.

To evaluate SparkJet operation and efficiency, the pressure sensor, current, voltage, and capacitance measurements were of primary interest. The pressure sensor output illustrated in Figure 4.1 passes through a PCB Model 482C Signal Conditioner designed for PCB pressure sensors before reaching the oscilloscope. Further details on the pressure sensor itself are provided in the next section. A CIC Research Model DP02-10K high-voltage differential probe was used to monitor the voltage difference across the anode and cathode. Current measurements were made using a Pearson Model 110 monitor and a Pearson Model A10 x10 attenuator to capture peak currents above 500 A. The capacitance parallel to the sustain electrodes was measured before each test using a Fluke Model 179 True RMS multimeter.

A variety of diagnostic measurements were also acquired. Monitoring the low-voltage pulse was through a BNC cable from the pulse generator to the oscilloscope. A BK Precision Model PR2000 200 MHz Oscilloscope High-Voltage, Single-Ended Probe with x100 attenuation and rated to 2 kV was used to measure the voltage across the electrodes on the 600ET circuits. To monitor the trigger voltage which typically exceeds 5 kV, a Tektronics P6015A 1000x high voltage passive test probe rated to 20 kV DC was used. Due to the design of the 600PST circuit, this probe also measured the voltage across the capacitors on the 600PST circuit. With simultaneous current and voltage measurements, the power drawn by the arc was directly calculated using Ohm's Law. The photodetector, an Electro Optics

Technology Biased Silicon Detector ET-2040, was used to diagnose the voltage and current waveforms. These waveforms tend to oscillate during the arc discharge and questions about how the oscillations correspond to the arc discharge prompted the use of the photodetector. The results of this diagnostic technique are discussed later in Chapter 6.

4.5 Cavity Pressure Sensor

The high-frequency pressure data was obtained using a PCB 105C12 dynamic pressure sensor (Figure 4.14) installed in the bottom of the SparkJet cavity, opposite the orifice. The sensor design includes threads for installation and a brass ring to provide a pressure seal. The force from the sensor threads due to the recommended torque (1.69 Nm) exceeds the strength of the Macor. Therefore, a stainless steel component was inserted into the Macor in order to support the sensor installation. The stainless steel component was secured to the Macor using 5-min epoxy. A detailed drawing of the metal insert is shown in Figure 4.15. The Macor and stainless steel are dimensioned such that the face of the pressure sensor is recessed from the bottom of the cavity. The recessed depth was chosen to allow for a stack of six 10 mil thick layers of electrical tape discs sized to match the diameter of the pressure sensor. A cross-sectional view of the assembled SparkJet actuator, metal insert, electrodes, pressure sensor, and tape is shown in Figure 4.16. The PCB 105C12 pressure sensor was chosen for its small size (2.5 mm sensing diameter), fast response time (< 2 μs), and high flash temperature tolerance (1922 K). An additional benefit of using this

Figure 4.14: Photograph of the uninstalled PCB 105C12 dynamic pressure sensor.

sensor is the low sensitivity to electromagnetic interference (EMI) because the sensor is connected to the PCB Model 482C signal conditioner via a shielded BNC cable.

The PCB sensing technology includes a preloaded quartz crystal surrounded by a stainless steel housing. The loading on the quartz determines the output signal. Ideally, only pressure changes at the sensor face affect the output signal. However, thermal loads can also affect the output signal due to the small size of the sensor and the proximity to the hot arc. To reduce the effects of the thermal shock associated with the initial blast wave, the initial test configurations involved coating the exposed face of the sensor with a layer of black RTV (Room Temperature Vulcanized) sealant. However, the long-term effects of the high-temperature air inside of the chamber expands the stainless steel housing and reduces the output signal such that the apparent pressure signal is more negative than the predicted chamber pressure. This thermal expansion hypothesis has been supported based on discussions with PCB technical engineers and a positive adjustment in the long-term pressure signal when more thermal insulation covers the sensor face. In addition, fast-Fourier transform (FFT) analysis of the pressure signal output indicated the sensor housing resonant frequency was being excited. As a result, the test configuration was

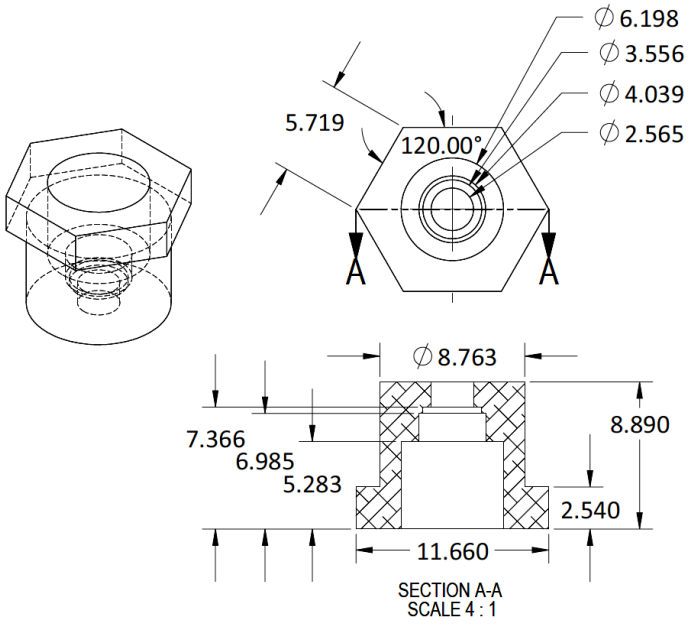

Figure 4.15: Drawing of the metal insert used to mate the SparkJet Macor housing to the PCB pressure transducer.

altered.

Based on conversations with PCB engineers, resonating the sensor housing can lead to nonlinear sensor output, signal attenuation, and significant signal uncertainty. PCB engineers suggested covering the sensor face with layers of electrical tape to dampen the initial shock wave effects exciting the resonance and protect the sensor from subsequent large thermal loads. This method, of course, raised concerns about the effect on sensor output. Therefore, tests were conducted to specifically understand the impact of using tape on the sensor face.

The goal of this comparison testing (tape vs. no-tape) was to show that covering the sensor with tape did not affect the ultimate efficiency measurement (peak filtered pressure). The expected differences in these testing configurations include

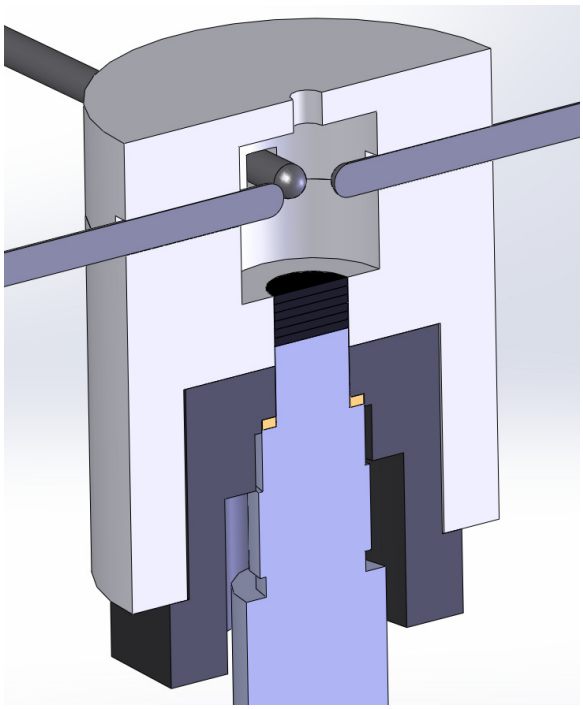

Figure 4.16: Cross section view of the SparkJet cavity, electrodes (configured for an external trigger), installed pressure sensor, metal insert, brass ring, and six layers of electrical tape.

a delayed initial pressure rise (time-of-arrival data), a reduction in thermal expansion of the sensor housing, and the elimination of excitation of the sensor housing resonance. The latter two effects are desired outcomes of using tape while the first effect is not desired. However, a goal of these comparative tests was to show that a delayed pressure response does not affect the peak pressure measurements required for efficiency estimation. The test conditions under which this comparative study was conducted were also carefully considered.

The SparkJet design used for this test included the largest of the three volumes (169.6 mm^3) in the test matrix and the 1 mm orifice diameter. The largest volume was chosen because a low Q_C/E was desired to avoid the thermal effects on the sensor housing. Therefore, E was maximized and, correspondingly, Q_C was minimized until the ultimate efficiency measurements were within a few percent of each other. At such a low Q_C/E, thermal effects become insignificant and the long term thermal effects were also insignificant. These conditions were met at a capacitance of 0.33 μF charged to approximately 300 V for value of $Q_C = 14.9$ mJ and $Q_C/E = 0.35$.

Figure 4.17 shows a comparison between tape vs. no-tape output over a long time frame (4.17(a), output over a short time frame (4.17(b)), and the FFT (4.17(c)) of the pressure signal. The pressure comparison over a large time frame shows that using the tape to protect the pressure sensor does not affect the magnitude of the output significantly, and the overall shape of the pressure oscillation bounds are similar. In addition, at the end of the pressure signal, both test configurations settle near 101 kPa which indicates that long term thermal effects are also not significant.

When focusing on the initial pressure sensor output in Figure 4.17(b), the first pressure rise occurs sooner for the no-tape configuration than for the tape configuration. This effect was expected as the force from the initial blast wave must travel through the six layers of 10 mil thick tape to impact the pressure sensor face. From this figure, it appears the time delay is approximately 1 μs.

Finally, the comparison between the FFT of the two test configurations shows that the frequency content is similar in the low frequency range (below 100 kHz). At 310 kHz, however, there is a large peak. According to the PCB 105C12 data specifications, the sensor resonance frequency occurs at or above 250 kHz. The peak at 310 kHz is the resonant frequency for this sensor which is evident in the no-tape testing configuration. However, the resonant peak is not visible in the tape configuration demonstrating the successful reduction of sensor housing resonance due to the pressure waves. The magnitude of the frequency content, however, is generally lower for the no-tape configuration than for the tape configuration. Based on conversations with PCB engineers, excitation of the sensor housing resonant frequency can cause signal attenuation across all frequencies. The ultimate goal of this comparison of the test configurations was to verify that the use of the tape does not affect the efficiency estimation value. Since the estimation involves filtering the raw pressure data, a discussion of the pressure signal post-processing is important.

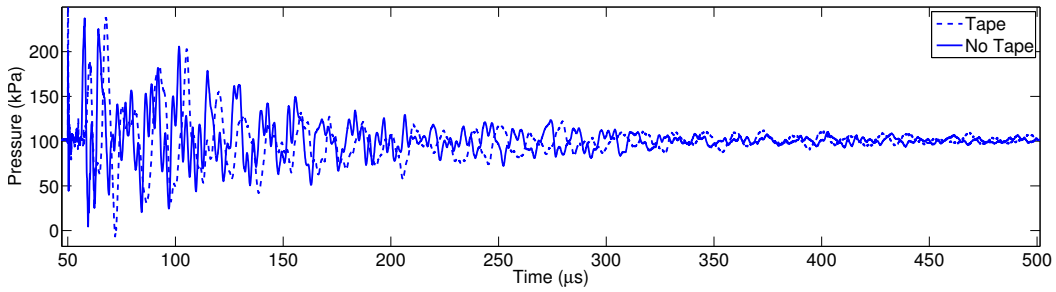

(a) Pressure output over large time frame

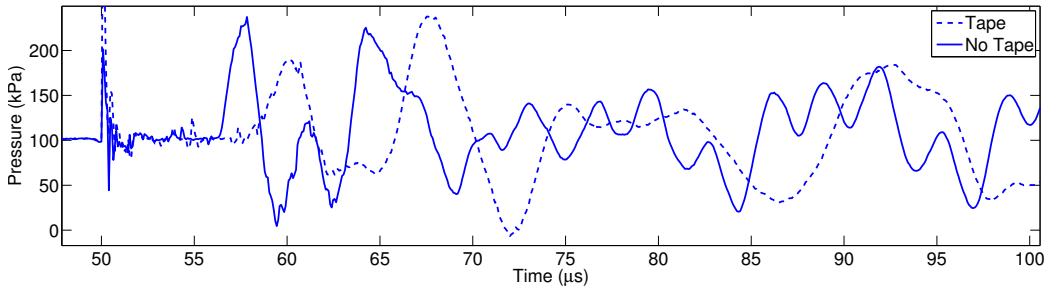

(b) Pressure output over small time frame

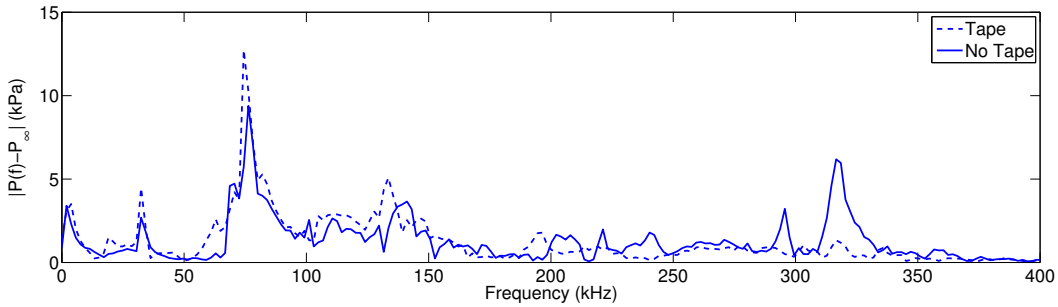

(c) FFT comparison

Figure 4.17: Comparison plots corresponding to the tape and no-tape test configurations including the a) ensemble averaged pressure over 500 μs, b) ensemble averaged pressure over 55 μs, and c) the FFTs of the ensemble averaged pressure signals.

4.5.1 Signal Post-Processing

For each SparkJet design, the voltage, current and pressure were acquired five times such that each signal could be ensemble averaged to reduce measurement uncertainty. The uncertainty for the differential voltage, current, and pressure measurements are ±10 V, ±10 A and ±50 kPa, respectively, based on the steady state oscillations before each arc discharge. Through ensemble averaging, these uncertainties were reduced to ±5 V ±3 A, and ±25 kPa, respectively. Uncertainty associated with the capacitance measurement before each discharge was 0.01 μF. For the voltage and current signals, this level of post-processing was sufficient to obtain a reliable signal with an improved signal-to-noise ratio. The unsteadiness observed in the pressure data is very repeatable; however, for efficiency analysis, unsteadiness obscures the volume-averaged peak pressure measurement. Therefore, the pressure output was low-pass filtered.

The cavity pressure data acquired is unsteady beginning with the very high pressure associated with the initial blast wave and subsequent reflected waves within the cavity. Following each pressure wave, the pressure signal drops to a very low value and can even be negative at high Q_C/E. Part of the oscillations are due to mechanical resonance of the sensor at 310 kHz as illustrated in the previous section. Natural pressure wave reflections occur at lower frequencies (≈100-250 kHz) depending primarily on cavity dimensions. Because the purpose of this efficiency analysis is to improve modeling accuracy in a 1-D model utilizing a volume-averaged cavity pressure, there is a need to apply a low-pass filter to the high-frequency oscillations.

The PCB output is linear up to one fifth the resonance frequency ($\approx$ 310 kHz) based on an FFT analysis of the pressure signals. Therefore, each pressure signal was decomposed into frequency components. Only components less than 60 kHz were used to provide a volume-averaged peak pressure estimate. The pressure signal in the time domain is converted to the frequency domains using the equations

$$a_0 = \frac{1}{T}\sum_{t=0}^{T} P(t)dt, \tag{4.1}$$

$$a_n = \frac{2}{T}\sum_{t=0}^{T} P(t)\cos(n\omega_0 t)dt, \tag{4.2}$$

and

$$b_n = \frac{2}{T}\sum_{t=0}^{T} P(t)\sin(n\omega_0 t)dt, \tag{4.3}$$

where $\omega_0 = 2\pi f_{sampling}$ ($f_{sampling}$ =250 MHz). Selecting the frequency components up to 60 kHz,

$$P(t) = a_0 + \sum_{n=1}^{n_{max}} a_n\cos(n\omega_0 t) + b_n\sin(n\omega_0 t) \tag{4.4}$$

is used to reconstruct the filtered pressure in the time domain. The maximum value of the resulting filtered pressure signal is used to determine the pressure-based efficiency. The mode corresponding to the cutoff frequency is given by

$$n_{max} = 2\pi\frac{\omega_0}{\omega_c}. \tag{4.5}$$

Figure 4.18 shows several comparative plots demonstrating the effect of filtering on the pressure signals. Specifically, Figure 4.18(a) shows the effect of filtering the ensemble averaged pressure signal. For both tape and no-tape test configurations, the filtered pressure signal contains far fewer oscillations than the unfiltered

pressure signal. Also noteworthy is that the maximum values of the filtered pressure signals are very similar. The maximum value is used to quantify pressure-based efficiency as discussed in the following section. The equation used to calculate the energy required to raise the cavity pressure to the maximum value (which will be derived in Section 4.6) is compared to the stored capacitor energy to provide an estimation of the pressure-based efficiency. The no-tape test configuration provides an estimate of 47.0% efficiency and the tape configuration provides an estimate of 50.4% efficiency. This small variation in efficiency estimate represents the uncertainty associated with using the tape to protect the pressure sensor face of 3.4%.

Figure 4.18(b) demonstrates the effect of applying the filtering technique described above. The filtered and unfiltered FFT results track almost exactly up to the cutoff frequency at 60 kHz. Beyond the cutoff frequency, the FFT of the filtered signal is nearly zero. This plot comparison clearly demonstrates the effectiveness of the low-pass filter.

After presenting the effect of filtering the low Q_C/E case, one may wonder if the filtering presents non-physical oscillations that would affect the efficiency prediction. To show that the oscillations actually do not significantly contribute to the peak pressure measurement, a high Q_C/E case ($Q_C/E = 18.0$) is presented in Figure 4.18(c) where the ensemble averaged pressure signal is filtered. Here the filtered signal clearly represents an averaged pressure signal. Again, both the tape and no-tape signals are presented to show that the tape still does not affect the peak pressure measurement at the beginning of the pressure rise. However, beyond the initial pressure rise, there is a slight difference between the tape and no-tape configuration

that lasts the remainder of the pressure signal. This difference is indicative of the long term temperature effects on the pressure sensor due to the high-temperature SparkJet cavity conditions. Also demonstrated in this figure is the visible reduction in pressure oscillations in the tape configuration due to the successful suppression of the pressure sensor resonance. Based on these test configuration comparisons, all testing was performed with tape covering the pressure sensor.

4.6 Efficiency

The arc discharge and resultant Joule heating are complex processes that are dependent on circuit design and localization of the arc discharge within the larger cavity. The purpose of this efficiency analysis is to provide an understanding of the SparkJet efficiency, the source of inefficiencies, and methods to improve efficiency starting with a calorically and electrically ideal assumptions. In addition, the results of this efficiency analysis will support on-going Stage 1 modeling to be included in a simplified model of the entire SparkJet cycle.

Efficiency is evaluated by determining the energy associated with the multiple processes involved in Stage 1. To begin, the maximum possible energy is defined as the stored capacitor energy, Q_C, as defined in Equation 2.1. Assuming no losses, this energy deposition can be used to estimate the cavity pressure and temperature rise as was shown in Chapter 3. However, there are several electrical and physical effects which reduce the energy output by the SparkJet actuator. During the conversion of stored capacitor energy to the arc, there are energy losses outside those described by

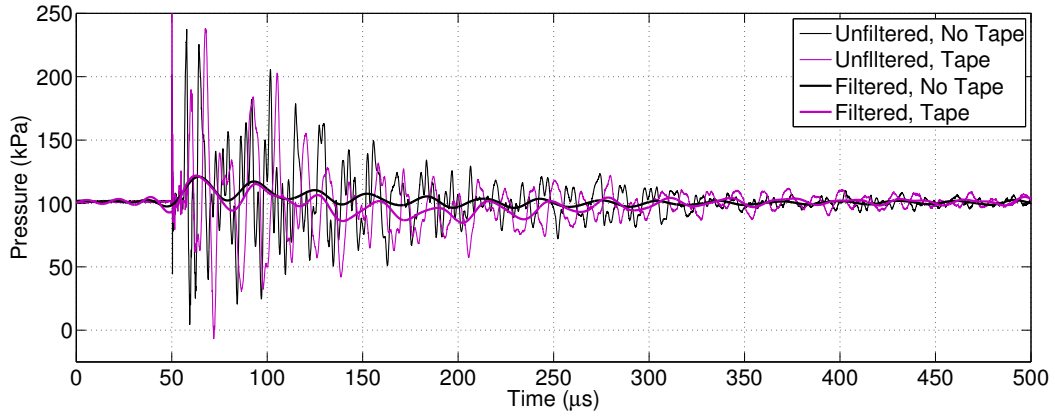

(a) Comparison of the time-dependent unfiltered and filtered pressure at $Q_C/E = 0.35$.

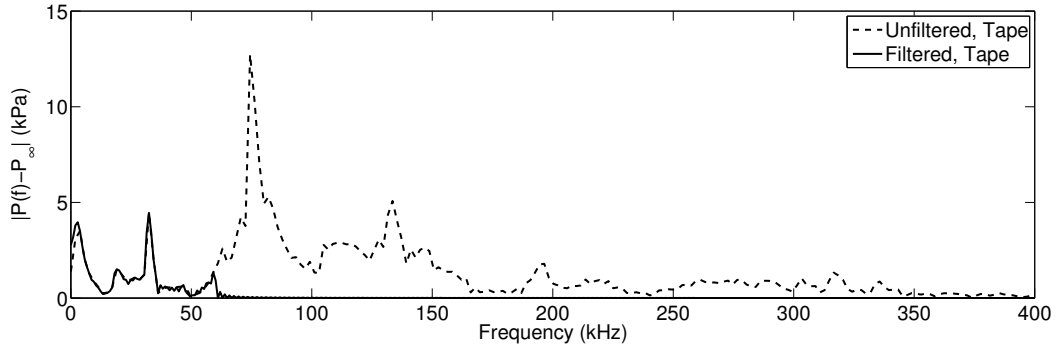

(b) FFT comparison between the unfiltered and filtered pressure.

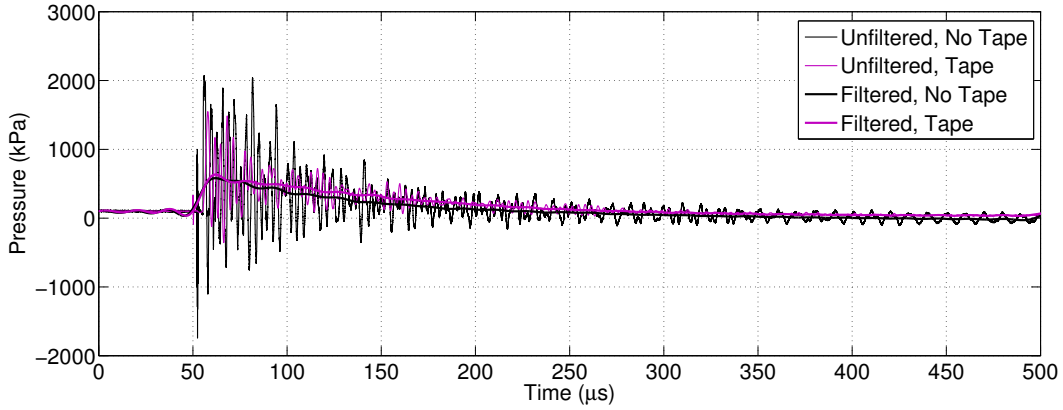

(c) Comparison of the time-dependent unfiltered and filtered pressure at $Q_C/E =$

Figure 4.18: Pressure and FFT data demonstrating the effect of low-pass filtering on the SparkJet internal cavity pressure measurements.

Narayanaswamy [63] which include resistance in the wires leading to the electrode tips, an increasing C_v as the cavity temperature increases, and localized, rather than distributed, energy deposition and heating. These phenomena result in an efficiency, η, less than 1.

The total energy released due to the power drawn by the arc is estimated by

$$Q_A = \int V(t)I(t)dt, \tag{4.6}$$

where V and I are directly measured. The efficiency related to converting stored capacitor energy to arc power is given by

$$\eta_A = Q_A/Q_C. \tag{4.7}$$

Efficiency losses here are related to parasitic resistance and inductance in wires and other circuit components that depend on circuit design.

The heat produced transfers from the arc column to the surrounding air or materials. Some heat is inevitably lost to the electrodes because the heat is released at the electrode tips [56]. The remaining heat, however, is transferred to the cavity air. The energy deposition calculation assumes the energy is added to the entire cavity volume to raise the cavity temperature. This assumption does not take into account the highly spatial effects associated with the arc discharge but provides some insight into the efficiency losses.

In an attempt to incorporate the effects of the high cavity temperatures, C_v is estimated as a function of cavity air temperature resulting in a temperature dependent C_v and a thermally perfect gas assumption. Once the new cavity temperature

is determined, the value of C_v is adjusted according to the simple harmonic oscillator model,

$$C_v(T) = C_{v,p}\left(1 + (\gamma_p - 1)\left[\left(\frac{\theta}{T}\right)^2 \frac{e^{\theta/T}}{\left(e^{\theta/T} - 1\right)^2}\right]\right), \tag{4.8}$$

and assuming a thermally perfect gas [64]. Here, γ_p and $C_{v,p}$ correspond to a calorically perfect gas values and θ is the molecular vibrational energy constant equal to 3055.6 K. At the conclusion of the energy deposition,

$$Q_T = mC_{v,p}(T_2 - T_1) \tag{4.9}$$

uses the final cavity temperature to determine the energy required to raise the cavity temperature assuming the idealized calorically perfect conditions. The efficiency associated with the conversion of stored capacitor energy to thermal energy, η_T, is defined as

$$\eta_T = Q_T/Q_C. \tag{4.10}$$

The additional loss due to a calorically imperfect gas helps explain the efficiency loss between the arc discharge energy and the measured peak cavity pressure presented in Chapter 5.

Finally, the peak pressure measured by the pressure transducer is used to determine the efficiency based on pressure measurements. The energy required to raise the cavity pressure to the measured peak pressure is determined by

$$Q_P = \left(\frac{P_m}{\rho R T_1} - 1\right) E \tag{4.11}$$

assuming the original calorically perfect assumptions. The ratio of Q_P to Q_C is used to calculate the pressure-based efficiency, η_P, defined as

$$\eta_P = Q_P/Q_C. \tag{4.12}$$

The following chapters show the resulting pressure data, arc power measurements and the corresponding efficiency analysis. A discussion of these results also leads to a modification to the Stage 1 modeling.

Chapter 5

Pressure-Based Results and Analysis

Using the experimental setups described in Chapter 4, the SparkJet performance based on cavity pressure, electrode voltage, and arc current is studied. This chapter focuses on the pressure-based results with analysis and discussion. First, a general understanding of the SparkJet cavity pressure as a function of several design parameters is considered. Second, the filtered peak pressure is converted to an efficiency metric as described at the end of Chapter 4. Finally, the time-dependent, filtered pressure results are compared to the 1-D model results.

5.1 Basic Operation

Before presenting the bulk of the experimental results, a look at a single SparkJet data acquisition cycle is considered here for the 600ET and 600PST circuits operated at low frequency (< 1 Hz). Figure 5.1(a) shows the typical output from the 600ET circuit. The dashed line shows the raw pressure transducer output and the solid black line shows the filtered pressure output to filter the transducer resonant frequency above 60 kHz. To observe the arc voltage and current, Figure 5.1(b) shows these signals over a 22 μs time frame. The blue, dash-dot line shows the voltage across the electrodes and the orange, dashed line shows the arc current. Note that the voltage across the actuators is approximately 600 V prior to initiating the

SparkJet. This value is not set to exactly 600 V and, therefore, analysis of each data set involves averaging the voltage over the first 4 μs (1000 samples) to determine the applied voltage across the actuators and, therefore, Q_C. The raw pressure transducer output is initially affected by EMI from the trigger spark as indicated by the negative spike at 50 μs but the signal conditioner prevents the output signal from continuing to be contaminated. While the EMI spike is not related to pressure, it indicates when the trigger spark was initiated. After the EMI spike, the first significant pressure rise provides the time of arrival for the first blast wave from the arc, typically 3-6 μs after the EMI spike. Beyond the first pressure rise, the signal represents the pressure due to the arc acting on the tape layers covering the face of the PCB sensor. The filtered pressure transducer output is the source of the efficiency and Stage 2 analysis in the subsequent sections.

Figure 5.2(a) shows the typical output for the 600PST circuit which is similar plot to Figure 5.1(a) except for one difference. The initial voltage across the electrodes is approximately 600 V, but there is a large rise in the voltage near 50 μs which represents the trigger voltage since both the trigger and capacitor voltages are applied to the anode. In this particular plot, the maximum value of the trigger voltage is not captured (saturated output) in order to maintain measurement resolution of the voltage during Stage 1. Figure 5.2(b) shows a zoomed-in section of Figure 5.2(a) focusing on the output signals during Stage 1. The arc current shown in Figure 5.2(b) represents the typical waveform seen for the 600PST circuit. The arc current data are presented in Chapter 6 with power-based analysis.

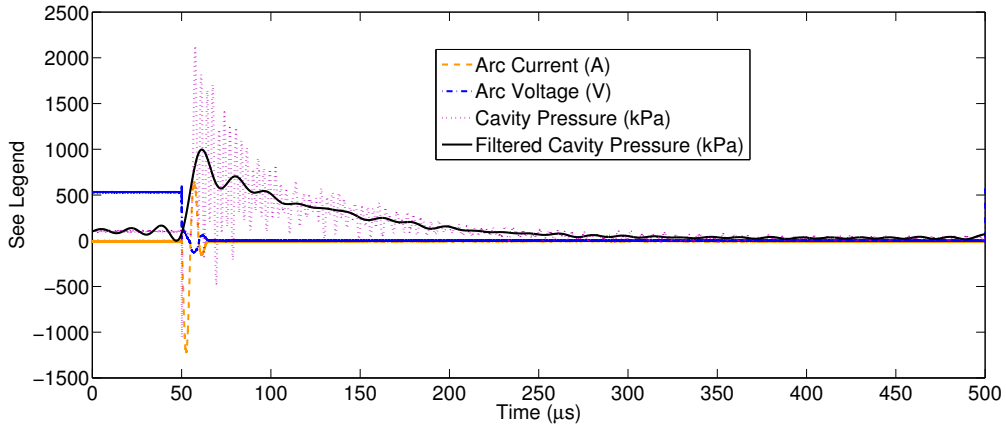

(a)

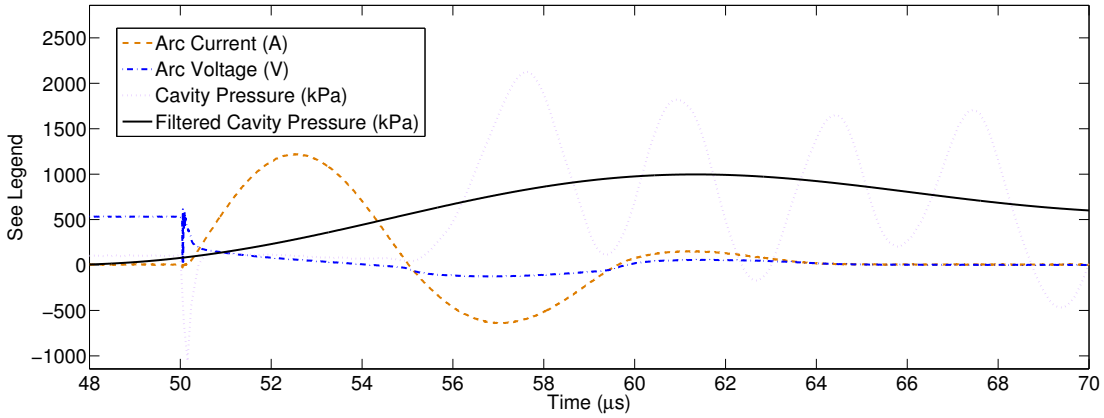

(b)

Figure 5.1: Example of ensemble-averaged data acquisition output for the 600ET setup and SparkJet cavity volume of 84.8 mm^3, orifice diameter of 1.0 mm, and capacitance of 4.28 μF a) over 500 μs and b) over 22 μs. ($f < 1$ Hz)

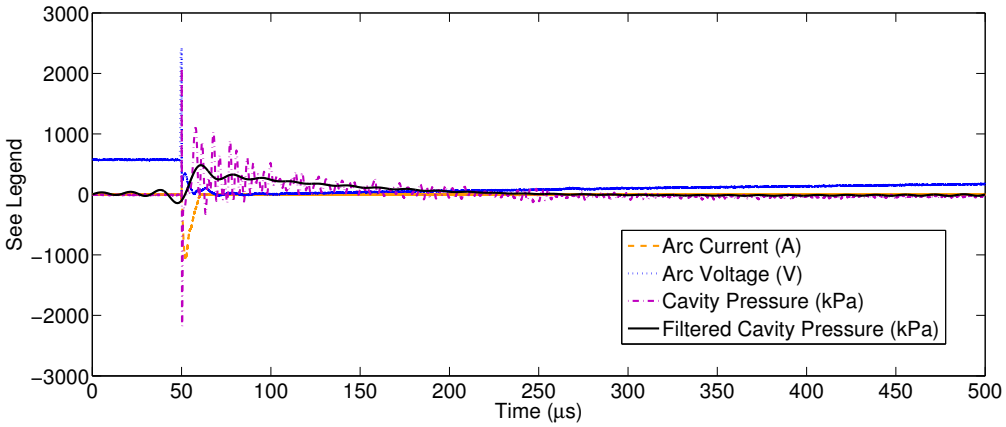

(a)

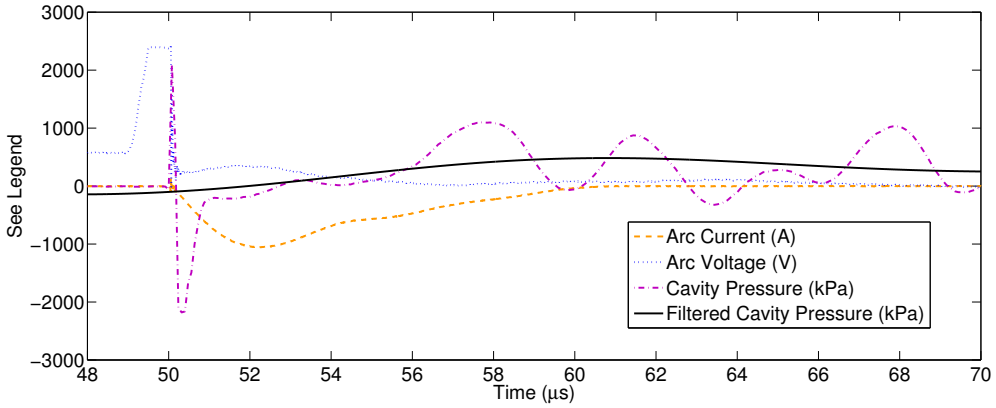

(b)

Figure 5.2: Example of data acquisition output for the 600PST setup and SparkJet cavity volume of 84.8 mm^3, orifice diameter of 1.0 mm, electrode gap of 1.0 mm, and capacitance of 3.72 μF a) over 500 μs and b) over 22 μs. ($f < 1$ Hz)

5.2 Results

As mentioned in Chapter 4, the SparkJet performance was evaluated over a range of cavity volumes, orifice diameters, electrode spacings, and input energy. This section will discuss and demonstrate in detail the effects of varying each of these parameters on the filtered cavity pressure. All results will be based on the 600ET circuit except for the electrode spacing results which are based on the 600PST circuit.

5.2.1 Variation with Input Energy

Using the 600ET circuit, the effect of varying the input energy has been studied. For these tests, the voltage remained near 600 V and the capacitance across the electrodes was varied by adding or removing capacitors. Five capacitors were used that summed to values of $C = 0.95$, 1.79, 2.57, 3.42, and 4.28 μF. Figure 5.3 shows the filtered cavity pressure output as the capacitance increased from 0.95 μF to 4.28 μF for a fixed volume of 84.8 mm^3 and orifice diameter of 1 mm. As capacitance increases, the energy input into the cavity increases and, correspondingly, the cavity pressure response is increased. Each pressure curve shape is very similar to each other and show that the duration of Stage 2 is relatively unaffected by increasing energy input. This trend is consistent with the results presented in Figure 3.17, demonstrating that both modeling and experimental results show increasing input energy does not affect the duration of Stages 2.

Another observation to note in Figure 5.3 is that the long-term pressure

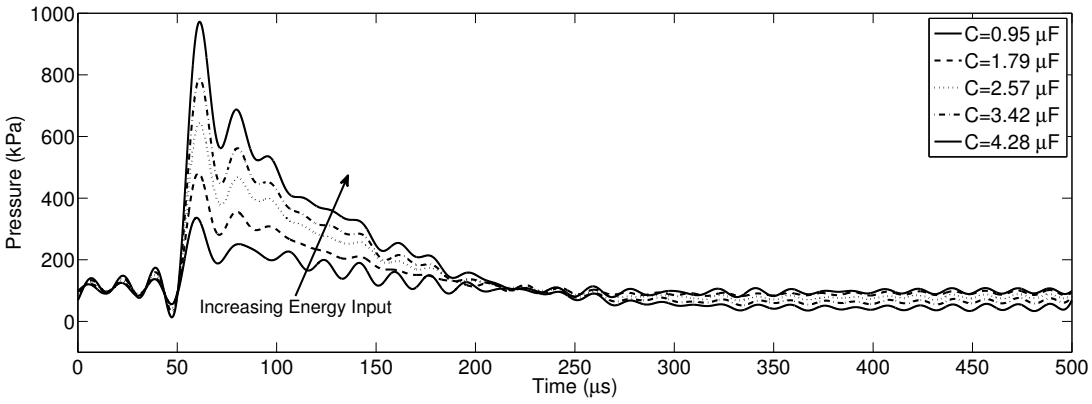

Figure 5.3: Variation in the filtered pressure signal as a function of capacitance for a cavity volume of 84.8 mm^3, orifice diameter of 1.0 mm, and electrode gap of 1.75 mm using the 600ET circuit. ($f < 1$ Hz)

signals vary slightly. The variation is due to the long-term thermal effects on the pressure sensor that are move prevalent as the input energy and, therefore, peak temperature increases. For the lowest capacitance value, the long-term thermal effects are minimal; however, the effects are present for large capacitance values despite the layers of insulating tape on the pressure sensor. While the tape does not completely eliminate the effects of arc heat, the effects are reduced.

As mentioned in Chapter 4, the peak filtered pressure is used to determine the efficiency, η_p, of each arc discharge. Figure 5.4 shows how the efficiency varies as the non-dimensional parameter Q_C/E increases. This figure also shows how efficiency varies for all three cavity volumes tested at a fixed orifice diameter of 1 mm and electrode gap of 1.75 mm. Over a very wide range of Q_C/E values, the efficiency values for all three volumes coalesce to one curve which decreases slowly from 42% to 21% as Q_C/E increases.

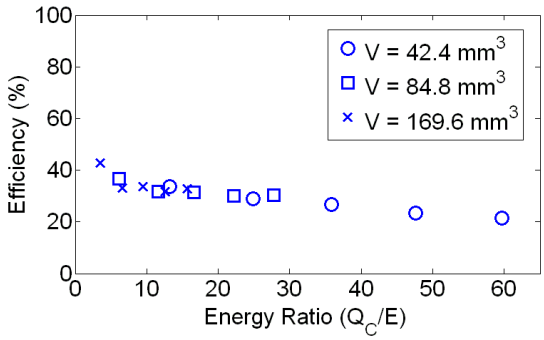

Figure 5.4: Efficiency of the SparkJet actuator as a function of Q_C/E for an orifice diameter of 1 mm, electrode gap of 1.75 mm, and cavity volumes of 42.4 mm^3, 84.8 mm^3, and 169.6 mm^3 using the 600ET circuit.

5.2.2 Variation with Cavity Volume

Using the 600ET circuit, the effect of varying cavity volume on the filtered cavity pressure has been evaluated. For these tests, the orifice diameter remained constant at 1 mm and the input energy was varied over the same range as in the previous section. The electrode gap was also kept constant at 1.75 mm. Figure 5.5 shows the filtered cavity pressure as a function of cavity volume. Since changes to the cavity volume alone affect the energy ratio Q_C/E, test cases of similar Q_C/E values were chosen and fall near 12.5. This figure shows that cavity volume does not have a significant effect on the peak pressure but does have a significant effect on the shape of the pressure signal. In general, increasing cavity volume increases the duration of Stage 2. Again, this trend is consistent with the results shown in the high-frequency modeling section demonstrating that increasing the cavity volume increases the duration of Stage 2 as is evident in Figure 3.18.

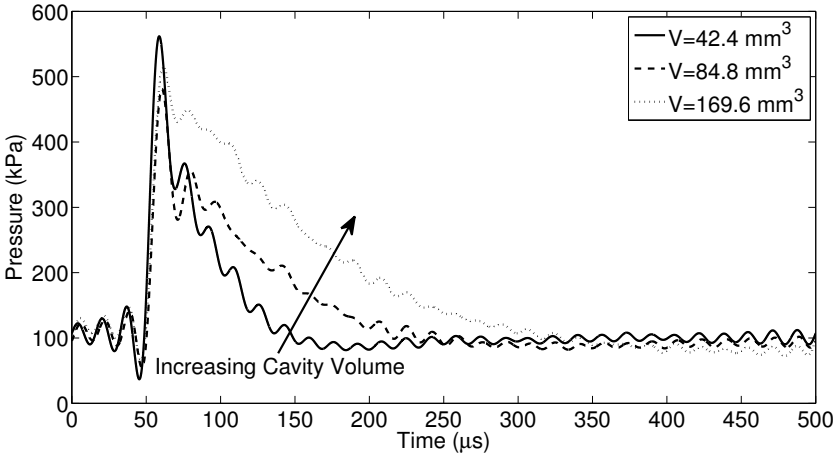

Figure 5.5: Variation in the filtered pressure signal as a function of cavity volume for a Q_C/E value near 12.5, orifice diameter of 1.0 mm, and electrode gap of 1.75 mm using the 600ET circuit. ($f < 1$ Hz)

5.2.3 Variation with Orifice Diameter

Using the 600ET circuit, the effect of varying orifice diameter on the filtered cavity pressure has been evaluated. For these tests, the cavity volume remained constant at 84.8 mm^3 and the input energy was varied over the same range as in the previous sections. The electrode gap was again kept constant at 1.75 mm. Figure 5.6 shows the filtered cavity pressure as a function of orifice diameter for d_o =0.4, 1.0, and 2.0 mm. Similar to the cavity volume results, the orifice diameter primarily affects the shape of the cavity pressure output. At an orifice diameter of 2.0 mm, the cavity pressure decreases quickly to 101 kPa after less than 100 μs. At an orifice diameter of 1.0 mm, the cavity pressure decreases more slowly and reaches 101 kPa after 200 μs. Finally, at an orifice diameter of 0.4 mm, the cavity pressure decreases over the longest duration of the three orifice diameters and reaches 101 kPa after

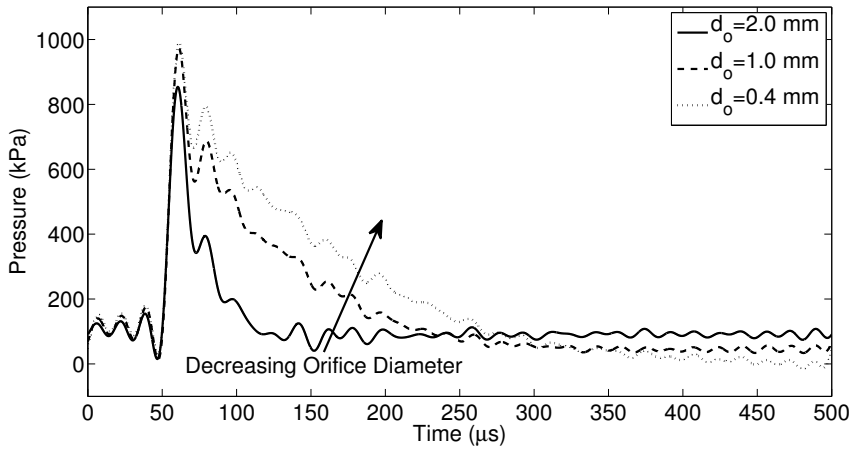

Figure 5.6: Variation in the filtered pressure signal as a function of orifice diameter for a Q_C/E value of 28, cavity volume of 84.8 mm^3, and electrode gap of 1.75 mm using the 600ET circuit. ($f < 1$ Hz)

250 μs. These results are consistent with the thought that the pressurized cavity air takes a longer duration to escape through a small diameter orifice than through a large diameter orifice.

Yet again, these experimental results are consistent with the trends discussed in the 1-D modeling section. Figure 3.16 shows that for a small orifice diameter, the high-frequency performance degrades at a lower frequency than that of a large orifice diameter. This result implies, and the experimental data confirms, that decreasing orifice diameter increases the duration of Stage 2. Variation in orifice diameter does not, however, affect SparkJet efficiency as the orifice diameter has no effect on the peak pressure rise.

5.2.4 Variation with Electrode Gap

While the main goal of introducing the pseudo-series trigger circuit was to increase reliability, an unexpected benefit was the increase to the maximum electrode gap. This benefit was explored experimentally by varying the electrode gap and quantifying the corresponding peak cavity pressure. The SparkJet actuator used to quantify the effect of changing the trigger mechanism on efficiency is identical to that described in Chapter 4 except without a trigger electrode. The SparkJet had a cavity volume of 84.8 mm^3, an orifice diameter of 1 mm and the electrode gap was evaluated at 1.0, 2.0, and 3.0 mm.

Testing demonstrates that increasing the electrode gap also increases the peak cavity pressure during Stage 1. Figure 5.7 shows the internal cavity pressure as a function of time for each electrode gap tested. This plot shows that increasing the electrode gap increases the energy transferred from the arc to the surrounding air during Stage 1. Figure 5.8 summarizes the curves shown in Figure 5.7 over a range of Q_C/E values. This plot shows that efficiency as a function of Q_C/E for various gap sizes follows similar exponentially decreasing trends as shown in Figure 5.4. For the 1 mm gap case, however, trends cannot be determined because all results are within the 3% uncertainty associated with the efficiency measurements. The largest change to the efficiency is seen for Q_C/E near 8 where the efficiency rises from 9% to 30% for a tip distance change from 1.0 mm to 3.0 mm, respectively. The surface area of the arc column between the electrodes is now much larger and interacts with a larger fraction of the surrounding air. With increased efficiency, the same

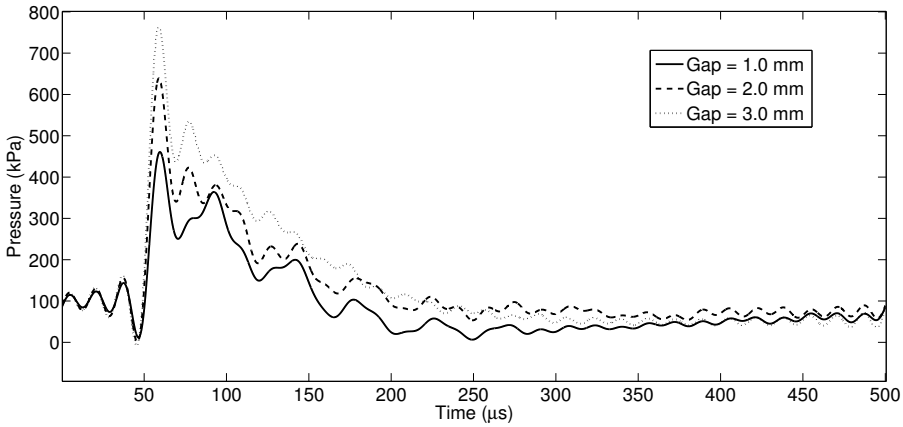

Figure 5.7: Comparison of pressure vs. time for three electrode gaps of 1.0, 2.0, and 3.0 mm given the same cavity volume (84.4 mm^3), orifice diameter (1.0 mm) and Q_C/E of approximately 28. ($f < 1$ Hz)

momentum throughput can be achieved for a lower energy input, Q_C/E.

5.3 Analysis

The previous section presented experimental data which showed the effect of varying cavity volume, orifice diameter, input energy, and electrode gap on the SparkJet cavity pressure. The trends showed that the duration of Stage 2 is dependent on cavity volume and orifice diameter, and independent of input energy and electrode gap. These trends associated with cavity volume, orifice diameter, and input energy were explored in Chapter 3 and the experimental results are consistent with the modeling results. However, the quantitative pressure results are not consistent with the modeling results. For example, as Figure 5.4 showed, the transfer of stored capacitor energy, Q_C, to raising the cavity pressure is inefficient. The efficiency is primarily a function of Q_C/E and the electrode gap. The modeling

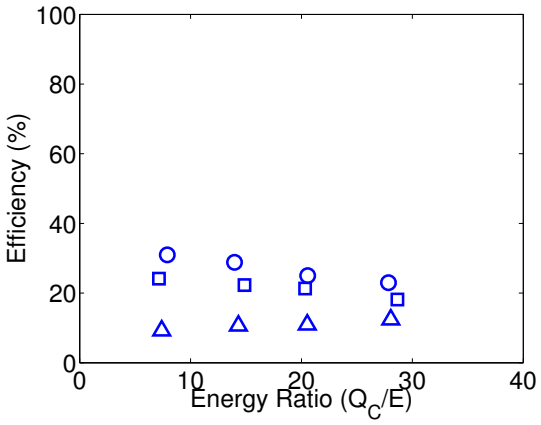

Figure 5.8: Comparison of efficiency vs. Q/E for three electrode gaps of 1.0, 2.0, and 3.0 mm given the same cavity volume (84.8 mm^3) and orifice diameter (1 mm). ($f < 1$ Hz)

results presented in Chapter 3 assumed all stored capacitor energy resulted in increasing the cavity pressure; however, it is clear from the experimental results that inefficiencies need to be incorporated into the model. In addition, the source of the inefficiencies need to be explored.

The experimental results in this chapter show that the method of transferring stored capacitor energy to energy involved in raising the cavity pressure is inefficient. There are several possible sources of inefficiency. First, the assumption that all of the capacitor energy is deposited in the arc ignores losses in circuit wiring and the possibility that the capacitor bank does not fully discharge during Stage 1. If the losses between the capacitor bank and arc are significant, the total energy applied to the cavity air is already lower than estimated. The measured power drawn by the arc is explored further in Chapter 6.

Another source of inefficiency could lie in the method of energy deposition.

The 1-D model assumes that the energy is deposited uniformly over the entire cavity volume. However, the arc discharge, the source of the thermal energy, is a concentrated filament between the electrode tips, which must conduct heat away from the arc into the cavity air. This process is highly spatially and temporally dependent. In addition, the extremely high arc temperature mentioned in the thermal modeling section of Chapter 3 far exceeds the temperature range associated with a calorically perfect gas. Therefore, at locally high cavity air temperatures, a unit of energy input does not raise the cavity temperature as much as that same unit of energy input into a locally low-temperature region of cavity air.

Finally, the protruding tungsten and copper electrodes may cause thermal heat transfer out of the cavity air before the cavity pressure reaches the pressure sensor. The electrode tips are, by nature, closest to the arc discharge and are an immediate avenue for heat transfer. The high thermal conductivity of both tungsten and copper also lead to very rapid heat transfer.

Incorporating the source of the inefficiency into the 1-D model would involve modeling the circuit or modeling the three-dimensionality of the arc energy deposition process. The first method of modeling the inefficiency would be simple except for the varying resistance of the arc throughout the discharge process. The second method is not practical for this 1-D modeling task as the arc energy deposition process is highly three-dimensional. Therefore, the inefficiency is incorporated into the 1-D model based on the experimental results as a coefficient, η, which ranges from

0 to 1.0. Including the pressure based efficiency,

$$P_2 = \rho_2 R T_1 \left(1 + \eta_P \frac{Q_C}{E}\right) \tag{5.1}$$

gives the model peak cavity pressure.

5.4 Comparison to 1-D Model

Direct comparison between the experimental results and the 1-D model are useful to assess the validity of the 1-D model. Comparisons as a function of cavity volume, orifice diameter, and input energy can be made, but cannot be made as a function of electrode gap since electrode gap is not modeled. These comparisons also incorporate the experimentally estimated efficiency.

Figures 5.9(a), 5.9(b) and 5.9(c) all confirm the trends related to the duration of Stage 2 and the dependence on cavity volume, orifice diameter and input energy. However, all of these figures also show that the model significantly over-predicts the duration of Stage 2. Based on the results presented in this chapter, factors such as cavity volume and orifice diameter can affect the duration of Stage 2. Increasing orifice diameter would lead to a shorter Stage 2; however, an effectively larger orifice diameter does not make physical sense. Decreasing the cavity volume would also lead to a shorter Stage 2; however, the amount of decreased effective volume is too significant to be physically possible.

Another possible reason for the over-predicted duration of Stage 2 is an under-prediction of heat transfer. Since the convective heat transfer rate was determined from CFD analysis, it is possible that CFD simulations and, therefore, the 1-D model

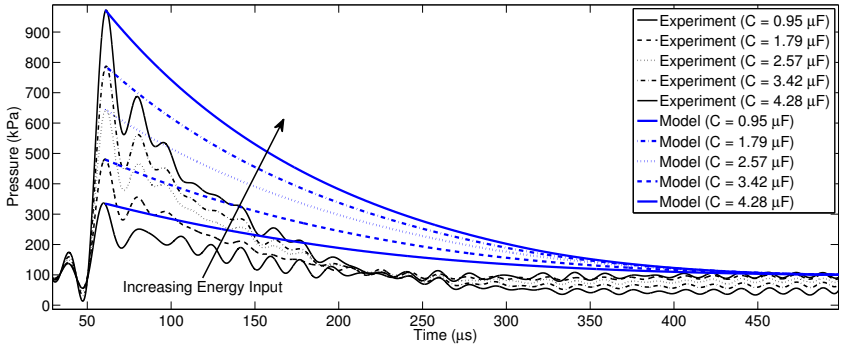

(a)

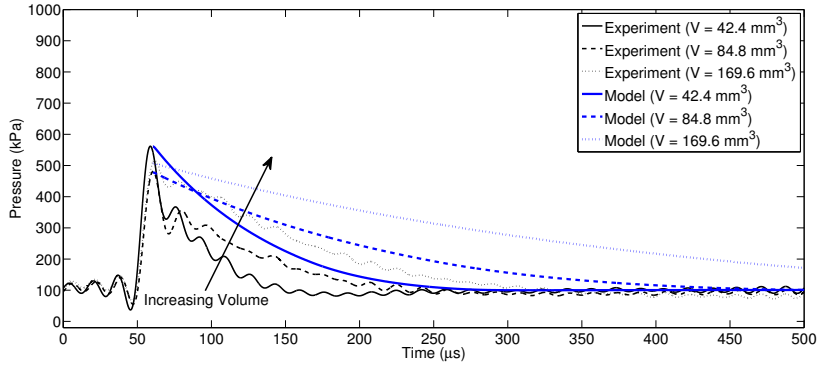

(b)

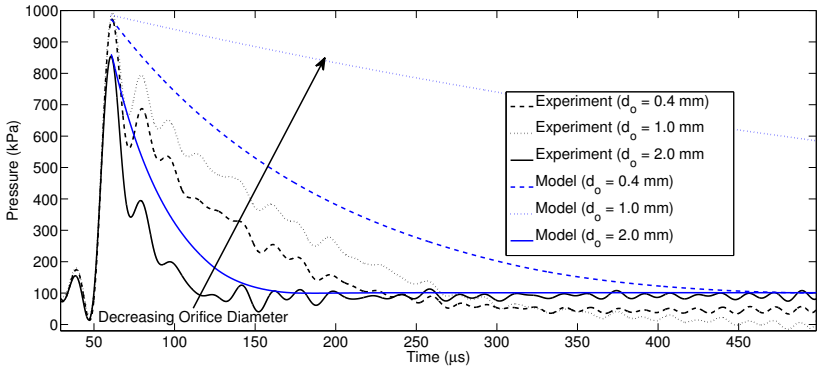

(c)

Figure 5.9: Comparison between experimental and modeled cavity pressure as a function of time as a) input energy, b) cavity volume, and c) orifice diameter are varied.

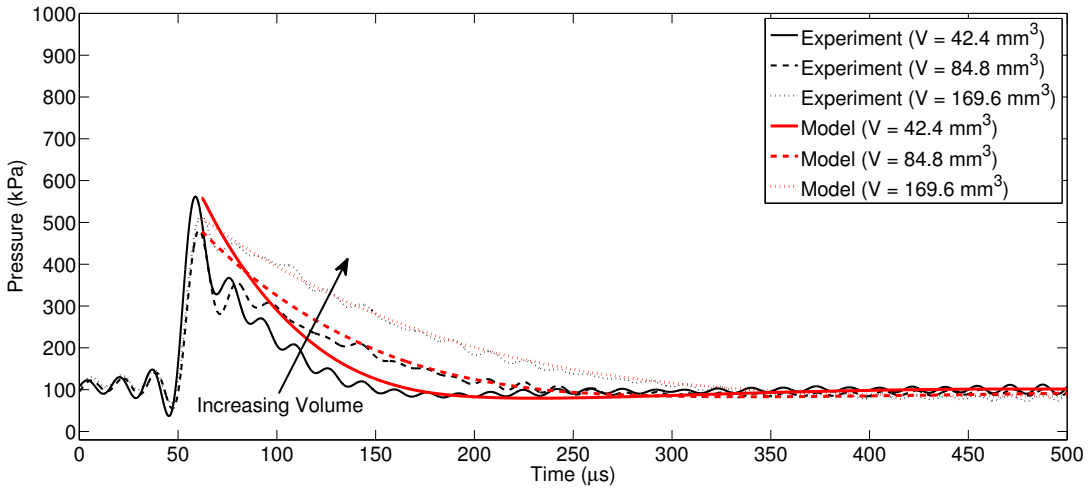

Figure 5.10: Comparison between experimental and modeled cavity pressure as a function of time as cavity volume is varied and the convective heat transfer coefficient is increased to $h_{in} = 6000$ W/m^{2}K.

under-predict the actual convective heat transfer rate. Arbitrary adjustments to the convective heat transfer rate within the 1-D model show that a value of 6000 W/m^{2}K provides improved comparison between the experimental data and the 1-D model. Figure 5.10 shows an example of the effect of increasing h_{in} to 6000 W/m^{2}K. The model and experimental values are in better agreement; however, this figure also highlights a potential issue with the efficiency estimation method. Rather than using the peak pressure to estimate efficiency, a method for averaging the initial peaks would be a better representation of the volume-averaged pressure.

This large change to the convective heat transfer coefficient has prompted some further exploration into the source of the differences. In particular, analytical methods for estimating the convective heat transfer related to entrance flows, such as the flow from the cavity to the orifice, have been investigated. To determine the

analytical equation to use for this estimation, the approximate Reynolds number, Re_D, associated with the flow through the orifice was estimated to be near 13,000 assuming air density is 1.225 kg/m^3, U = 600 m/s, $D = d_o$ = 1 mm, and $\mu \approx 6\times10^{-6}$ kg/ms at elevated temperatures. Therefore, the flow through the orifice is considered laminar. The average Nusselt number, $\overline{Nu}_D$, for laminar flow in a duct of length L can be estimated using

$$\overline{Nu}_D = 3.66 + \frac{0.065\,(D/L)\,Re_D Pr}{1 + 0.04\,[(D/L)\,Re_D Pr]^{2/3}}, \tag{5.2}$$

where Pr is the Prandtl number, which is approximately 0.7 for air [65]. Using Equation 5.2, the average Nusselt number is 66.45. Nusselt number is defined as

$$Nu = \frac{hD}{k} \tag{5.3}$$

where h is the convective heat transfer and k is the convective heat transfer coefficient of air. Rearranging Equation 5.3 to solve for h and assuming the conductivity of air is approximately 0.05 W/m^2, the approximated convective heat transfer coefficient is 3322 W/m^2. This value is much larger than the originally estimated 125 W/m^2 but not quite as large as 6000 W/m^2. Regardless, this analytical check provides some support for increasing the convective heat transfer coefficient used in the model. At the same time, further investigation into the disparity between the model and experimental results is still required.

The over-prediction of the duration of Stage 2 brings the rollover frequencies presented in Chapter 3 and Figures 3.16-3.18 into question. A reduced duration of Stage 2 would lead to an improved high-frequency performance. To demonstrate

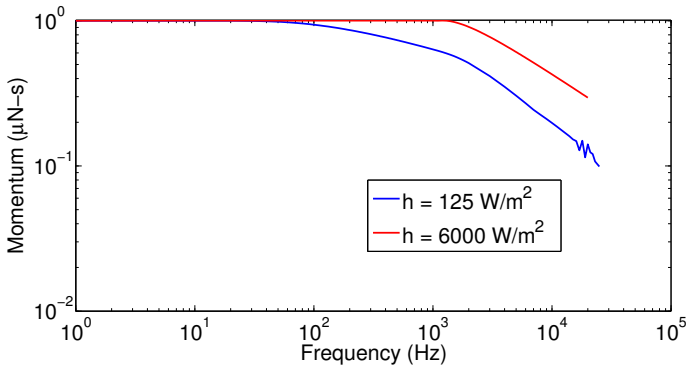

Figure 5.11: Comparison between the modeled normalized, steady-state momentum as a function of actuation frequency for convective heat transfer coefficients of 125 W/m^2 and 6000 W/m^2. ($Q_C = 0.45$ J, $v = 84.8$ mm^3, $d_o = 1$ mm)

the effect of the increased heat transfer rate, Figure 5.11 shows the comparison between the high-frequency performances corresponding to $h_{in} = 125$ W/m^2 (replotted from Figure 3.16) and $h_{in} = 6000$ W/m^2. All other parameters are identical. The comparison plot shows that the rollover frequency increases significantly from approximately 100 Hz to 1000 Hz thereby demonstrating the improved high-frequency performance with an increased convective heat transfer coefficient.

The increased convective heat transfer coefficient is significantly larger than the original value of 125 W/m^{2}K as determined through comparisons to CFD simulations. At the same time, the high-temperature waves that impact the SparkJet cavity walls can easily be significantly higher than the CFD and 1-D model predictions. A larger temperature difference between the air and the wall would lead to larger convective heat transfer, which is essentially the effect of increasing the convective heat transfer rate. Another possible cause is the inability to capture heat loss to the electrodes. The exact cause for the difference in the duration of Stage 2

is unknown; however, incorrect assumptions related to heat transfer (convective or conductive to electrodes) is the most plausible explanation.

5.5 Summary

In this chapter, the SparkJet cavity pressure response to an arc discharge has been experimentally explored. A look at the unfiltered pressure data and the corresponding arc current and voltage show that the initial pressure rise occurs between 3 and 6 μs after the arc discharge begins. The resulting unfiltered pressure signal is highly unsteady due to excitation of the pressure sensor resonant frequency. Therefore, the pressure signal is filtered and the maximum value of the filtered pressure signal is used to estimate efficiency. The filtered pressure signal is also used to understand the effect of cavity volume, orifice diameter, input energy, and electrode gap on the duration of Stage 2.

Stage 2 is affected by cavity volume and orifice diameter but is independent of input energy and electrode gap. The duration of Stage 2 directly affects the ability to maintain high-momentum throughput during Stage 2 when operated at high-frequency. A long Stage 2 results in poor high-frequency performance while a short Stage 2 duration results in good high-frequency performance. The cavity is able to refill with external air during Stage 3 sooner if Stage 2 is short. Therefore, for high-frequency applications, a small cavity volume and large orifice diameter are ideal. The input energy and electrode gap allow the SparkJet designer to control the peak cavity pressure and efficiency of delivering energy to the cavity. However, as

input energy increases, the SparkJet efficiency decreases. Also, as the electrode gap increases, efficiency increases but, based on user experience, reliability also tends to decrease.

Quantitative comparisons between the 1-D model and experimental results show significant differences in the prediction of the duration of Stage 2. The model results predict a much longer Stage 2 duration than is shown in the experimental results. The most plausible explanation for these differences is in the mis-prediction of heat transfer related to non-1-D effects.

The experimental results presented in this chapter showed that pressure-based efficiency was as low as 20%, whereas the model assumes 100% efficiency. The differences between experiment and modeling are considered part of an overall SparkJet inefficiency. Several possible reasons are provided to explain the source of the inefficiency. One of these reasons is the inefficient energy transfer from the capacitors to the arc. The following chapter uses experimental measurement of the arc current and voltage to explore this hypothesis.

Chapter 6

Power-Based Results and Analysis

The results presented in Chapter 5 demonstrated that the experimentally measured pressure-based efficiency was as low as 20% whereas the model assumes 100% efficiency. Initial analysis discussed the role of the power drawn by the arc to explain one of the contributing factors toward the loss in SparkJet efficiency. This chapter looks into measuring and quantifying the power and energy drawn by the arc based on voltage and arc current measurements.

6.1 Arc Power Results

In order to investigate the source of the low pressure-based efficiencies shown in the previous chapter, the power drawn by the arc has been evaluated. Because arc power is independent of parameters such as cavity volume and orifice diameter, these parameters are kept constant for this analysis. Therefore, the arc discharge power was evaluated for a SparkJet with a cavity volume of 84.8 mm^3, orifice diameter of 1 mm, capacitor voltage of approximately 600 V, and five capacitance values ranging from 0.95 μF to 4.28 μF. Corresponding to each capacitance value, Figure 6.1 shows five current, voltage and power waveforms for a constant electrode gap of 1.75 mm. Figure 6.1(a) shows that as capacitance increases, both the current magnitude and period increase. Correspondingly, Figure 6.1(b) shows that as capacitance increases,

the duration of the voltage drop increases such that time derivative of the voltage drop during the arc discharge decreases in magnitude. Evaluating the product of the current and voltage, the power drawn by the arc is shown as a function of time in Figure 6.1(c).

Additionally, the resistance can also be calculated when the voltage and current across the arc are known using Ohm's Law. Figure 6.2 shows the calculated resistance as a function of time for a capacitance of 4.28 μF. Referring to Figure 6.1(c), the power curve for this capacitance level experiences three surges. Also note that Figure 6.2 shows three regions of varying resistance that correspond to the power curve. For each power surge, the resistance exponentially decreases to a small value. Each subsequent region, however, decreases to a slightly higher resistance than the previous region. The increasing resistance indicates that the arc column is decreasing in temperature since arc column resistance is inversely proportional to arc temperature [66]. Referring also to Figure 6.1(b), the spikes present in Figure 6.2 correspond to when the voltage crosses zero.

Figures 6.1(a) and 6.1(b) also show that inductance in the circuit drives the voltage and current to continue to oscillate. To determine if these oscillations correspond to the arc discharge or are artifacts of circuit inductance, a photodetector was placed near the SparkJet. Assuming light production corresponds to the presence of the arc, an increasing trend in the photodetector output during the entire duration of the power waveform indicates the corresponding presence of the arc. To aid in the qualitative comparison, the arc power drawn is correlated to the light output in Figure 6.3. This plot shows that the light output increases significantly during the

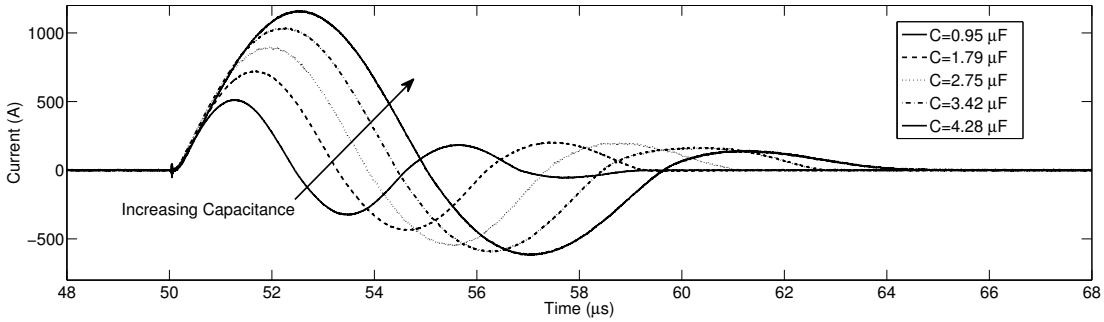

(a) Current Waveforms.

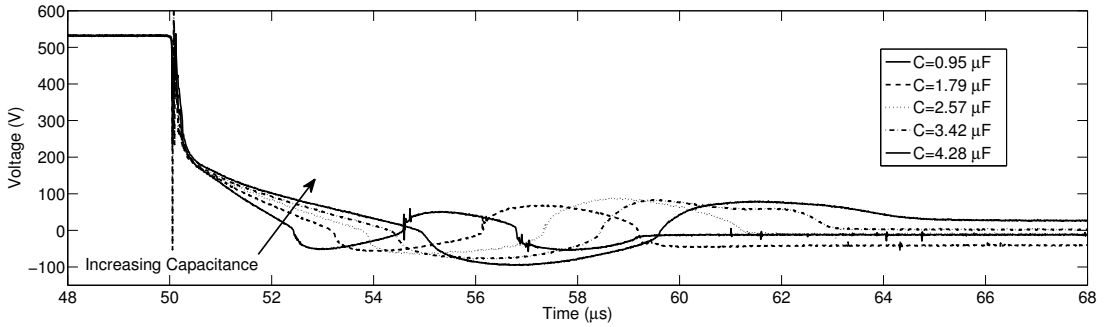

(b) Voltage Waveforms.

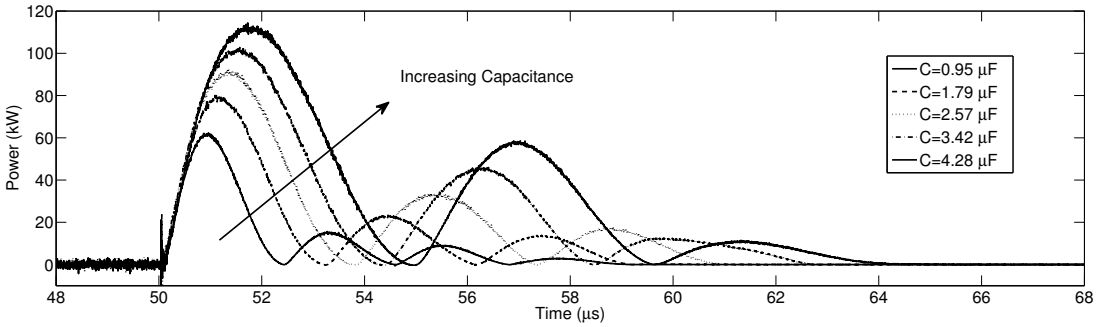

(c) Power Waveforms.

Figure 6.1: Voltage, current, and power waveform curves in distinct groups corresponding to each capacitance change for a cavity volume of 84.8 mm^3 and orifice diameter of 1 mm. ($f < 1$ Hz)

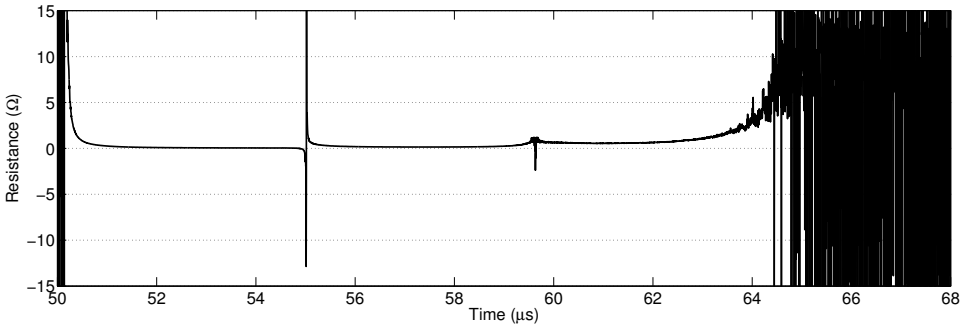

Figure 6.2: Time-dependent variation in arc resistance for a capacitance of 4.28 μF and electrode gap of 1.75 mm. ($f < 1$ Hz)

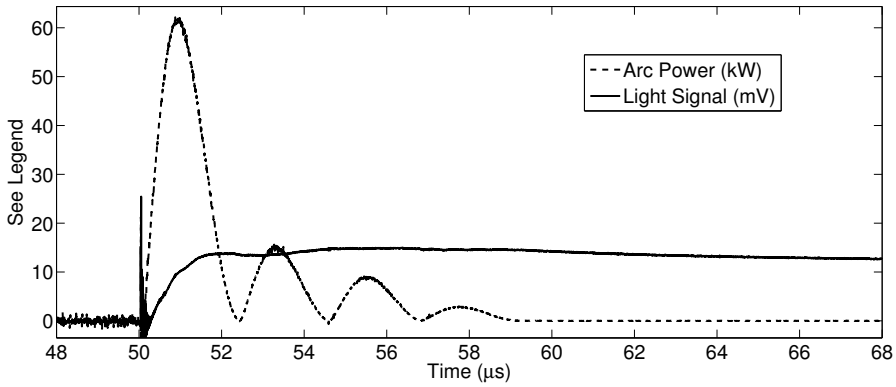

Figure 6.3: Time-dependent variation in arc power and qualitative light generation by the arc for a capacitance of 0.95 μF and electrode gap of 1.75 mm. ($f < 1$ Hz)

first power surge. Beyond the first rise in the light output, the light output does not rise as significantly as the initial increase but it does increase slightly. Only after the power drawn reaches zero does the light output start to continuously decrease. Based on these results, the power drawn after the initial power spike does contribute to the overall arc power.

With an understanding of the voltage, current, and power measurements during the arc discharge process, the energy drawn by the arc is calculated by in-

tegrating the power curve between the initial voltage drop and when the current reaches zero according to Equation 4.6. The energy drawn is divided by the stored capacitor energy, Q_C, to calculate the capacitor to arc power efficiency and the results are shown by the triangles in Figure 6.4. These results show that approximately 80% of the energy stored in the charged capacitor bank is converted to power drawn by the arc. These losses are likely due to the parasitic resistance and inductance corresponding to the 0.46 m of 22 AWG wires leading from the capacitors to the arc. Based on wire resistance tables, this length of wire and wire gauge corresponds to 0.024 Ω. Assuming the arc current also passes through these wires, there is approximately an 8% power loss due to the wires alone. The remaining power loss is likely due to contact resistance of the connectors between the wires and electrodes, incomplete energy transfer from the capacitors, or other sources of parasitic circuit resistance.

For comparison, the pressure-based efficiency for these tests is shown in Figure 6.4 by the squares using the same analysis as described in Chapter 5. These pressure-based efficiencies shows that the conversion of energy stored in the capacitors to the energy required to raise the cavity pressure (assuming calorically perfect gas) is 30-50% efficient. Therefore, the majority of the efficiency loss stems from the efficiency loss from the arc to the cavity air. To explain some of the additional efficiency losses and estimate temperature rise in the cavity, the instantaneous arc discharge and calorically perfect gas assumptions are removed using Equation 4.8.

The third set of points in Figure 6.4 correspond to the estimated efficiency based on the non-instantaneous, thermally perfect energy addition where $Q_C = 0.6$ J

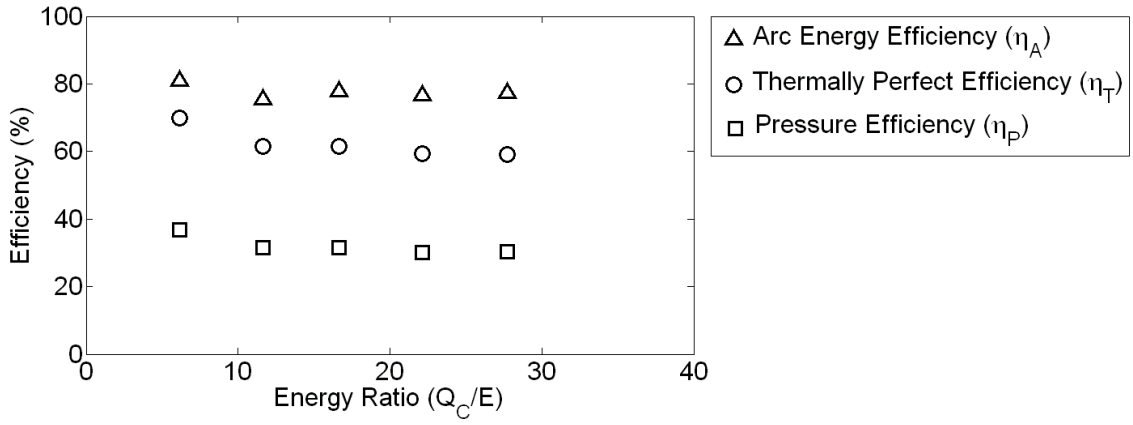

Figure 6.4: Efficiency of the conversion of stored capacitor energy to the arc discharge, calculated cavity temperature, and measured pressure rise as a function of Q_C/E.

($C = 4.28$ μF). The effect of assuming a thermally perfect gas according to Equation 4.8 is shown in Figure 6.5. This figure shows the power drawn by the arc discharge that results in the energy deposition into the cavity. Assuming a non-instantaneous energy deposition into a calorically perfect gas where C_v is constant, the dash-dot curve shows the corresponding temperature variation. For comparison, the non-instantaneous energy deposition into a *thermally* perfect gas where C_v is a function of cavity temperature is shown with the dotted curve. The corresponding variation in the specific heat constant is also shown for reference with the dashed curve. This comparison shows that incorporating a thermally perfect assumption reduces the final cavity temperature, T_2 up to 1500 K. The temperature difference assuming a thermally perfect gas increases as Q_C increases as shown in Figure 6.5(b). The efficiency based on these calculations is shown in Figure 6.4 with the circles. Based on this analysis, the removal of the calorically perfect assumption accounts

for approximately 10-25% of the pressure-based efficiency losses.

The remaining pressure-based efficiency losses are most likely due to heat loss to the electrodes. Roth et al. [56] measured heat loss to electrodes due to arc discharges in a variety of gases and for a range of electrode spacings and electrode diameters. While none of Roth's tests were in air, the thermal diffusivity of Argon, one of the gases tested, is very similar to that of air. Similar to the SparkJet experiments, Roth also tested heat loss for electrodes of a diameter of 1 mm and electrode gap of 2 mm in Argon pressurized at 101 kPa. The results showed that approximately 50% of the heat generated by the arc discharge was lost to the electrodes. This electrode heat loss is quite significant but, based on the results presented by Roth, can be significantly reduced by increasing the electrode gap. The following section explores this method of reducing heat loss.

6.2 Pseudo-Series Trigger Results

To explore the effect of varying the electrode gap on power drawn by the arc, the 600PST circuit was used with a SparkJet actuator of a cavity volume of 84.8 mm^3 and orifice diameter of 1 mm. The effect of the electrode gap was evaluated at 1 mm, 2 mm and 3 mm. In the previous chapter, the pressure based results showed that the peak pressure increases with increased electrode gap. In this section, the increase in peak pressure is supported by arc power measurements. Figure 6.6 shows the power drawn by the arc for $Q_C = 0.61$ J. While the differences in the power curves are not significant, the area under the power curve for the 1 mm electrode gap configuration

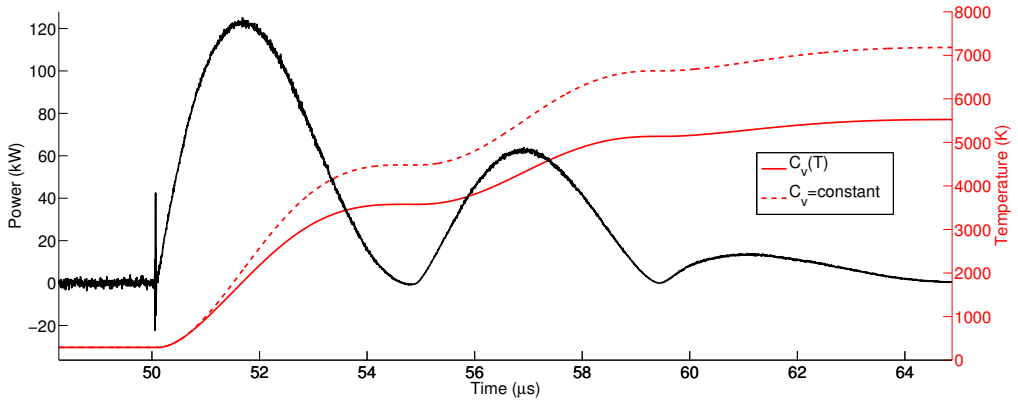

(a)

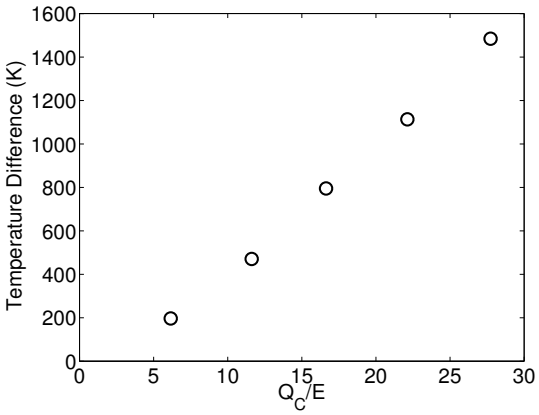

(b)

Figure 6.5: Comparison of the time dependent temperature and specific heat coefficient (C_v) assuming a calorically and thermally perfect gas as a function of arc discharge current and voltage for (a) a single value of $Q_C/E = 27.8$ and (b) the final temperature difference over a range of Q_C/E values. ($f < 1$ Hz and gap of 1.75 mm)

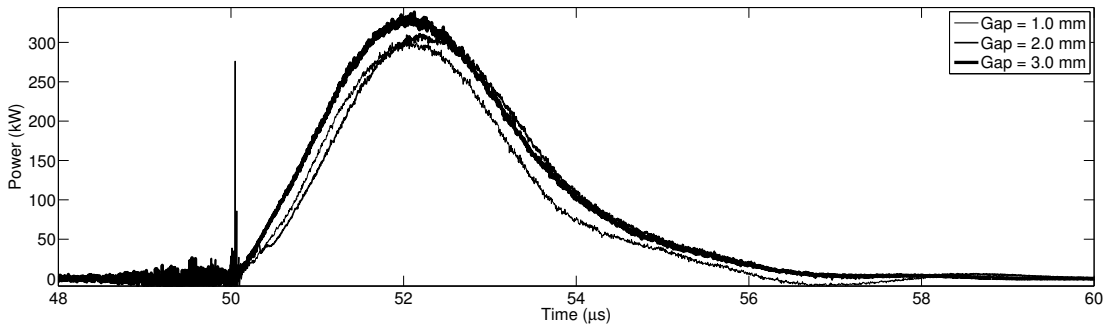

Figure 6.6: Power drawn by the arc for an electrode gap of 1 mm, 2 mm and 3 mm. ($f < 1$ Hz, $Q_C = 0.61$ J)

is visibly less than the area under the curve for 3 mm. Therefore, the reduced arc energy is likely the source of the decrease in efficiency as the electrode gap decreases.

6.3 Summary

Through this experimental analysis of the arc power, the source of efficiency losses during Stage 1 of the SparkJet cycle are better understood. The results presented in this chapter show that arc power increases as a function of capacitance and electrode gap. These results also show that removing the 1-D modeling assumptions of an instantaneous energy deposition and calorically perfect gas accounts for some of these efficiency losses. However, to capture these effects, time-dependent current and voltage information are required. This information can be acquired experimentally; however, in the interest of building a self-contained 1-D model, the entire SparkJet circuit could be modeled. The primary challenge associated with modeling the circuit, however, is modeling the time-dependent variation in arc re-

sistance. As shown in Figure 6.2, this resistance is complex and challenging to simulate. Therefore, it is recommended that the power drawn be experimentally obtained and applied to the model for varying input energy and electrode gap.

With an understanding of the losses, the SparkJet design can be improved to minimize losses. For example, the wires leading from the capacitor bank to the electrode gap should be shortened and of a larger gauge. Also, the circuit should be designed to promote larger electrode gaps to, not only reduce heat loss to the electrodes but, enlarge the arc channel to disperse heat from the arc to the surrounding air more quickly. Another advantage of increasing the electrode gap is the reduced electric field between the electrode tips such that the arc resistance relative to the parasitic wire resistance is increased; therefore, the relative power drawn by the arc is higher than the power drawn by the wires.

Chapter 7

Conclusions and Future Work

This final chapter summarizes the wide variety of results and conclusions presented in this dissertation. The original goal of this work was to address the hypothesis that the complexities of the SparkJet actuator can be modeled using 1-D analysis. The primary benefit of developing such a model is the ability to analyze several SparkJet designs faster than generating CFD simulations. Several aspects of this research have demonstrated that the SparkJet can, indeed, be simplified by a 1-D model. However, the model has difficulty capturing aspects related to the arc discharge and heat transfer beyond empirically-based coefficients. Defining these aspects is an area considered for future work.

7.1 Summary of Results

This dissertation has provided a significant contribution to the state of the art pertaining to 1-D model development and experimental results to understand design factors that affect SparkJet performance. The first contribution from this dissertation was the development of the 1-D SparkJet model to rapidly generate SparkJet performance information for a variety of design variations. Using the Navier-Stokes equations, this model was developed under several assumptions. These assumptions include inviscid flow, time-dependent 1-D representation of the cavity pressure, tem-

perature, density, and jet velocity, a calorically perfect gas, and instantaneous energy deposition. Additionally, a thermal model, based on a lumped circuit-element representation, has also been developed, which incorporates convective and conductive heat transfer.

Through comparison with a CFD simulation, the assumptions of inviscid flow and 1-D cavity pressure, temperature, density and jet velocity were well supported. The CFD simulation was also used to estimate the convective heat transfer coefficient. During the initial 200 μs, the CFD results captured unsteadiness within the cavity whereas the 1-D model did not. However, beyond the first 200 μs, the 1-D model and CFD results align quite well. Agreement in the later portion of the SparkJet cycle is important for modeling high-frequency actuation.

Supported by the comparison to CFD results, the model was exercised to explore SparkJet high-frequency performance and evaluate the effect of increasing actuation frequency on SparkJet momentum throughput as a function of several design parameters. The high-frequency evaluations showed that high-frequency performance is primarily affected by cavity volume and orifice diameter. For example, the model shows that a typical SparkJet design (1 mm orifice diameter, 84.8 mm^3 cavity volume and 0.5 J energy input) operated over a range of frequencies from 1 Hz to 10 kHz shows a decrease in peak momentum corresponding to an actuation cutoff frequency of 800 Hz. By halving the orifice diameter to 0.5 mm, the cutoff frequency was near 300 Hz and by doubling the orifice diameter to 2.0 mm, the cutoff frequency is near 2.5 kHz. As cavity volume increases, high-frequency performance decreases; as orifice diameter increases, high-frequency performance increases. The

effect of input energy on high-frequency performance was also considered but modeling results showed that input energy does not have an effect on the cutoff frequency.

To support aspects of the 1-D model related to Stage 1 (arc discharge), experimental measurements of cavity pressure and arc power were acquired. These results not only provided insight into Stage 1, but also Stage 2 (jet flow). Regarding Stage 1, results showed that the experimentally measured peak pressure is significantly (60-80%) lower than assumed in the 1-D model. This discrepancy signifies inefficiencies associated with transferring capacitor energy to the cavity air. The efficiency is a function of both input energy and electrode gap, which decreases slightly as input energy increases and increases moderately as electrode gap increases.

Regarding Stage 2, the experimentally observed trends pertaining to the duration of Stage 2 and, therefore, high-frequency performance are the same as was seen in the modeling results. The modeled dependence on orifice diameter, cavity volume, and input energy were confirmed by experimental results. However, the quantitative duration of Stage 2 is not well modeled such that the model overpredicts the duration of Stage 2. Consideration of several aspects of the 1-D model lead to the thought that inaccurate representation of heat transfer stemming from the convective heat transfer coefficient itself, underestimation of the cavity temperature, or heat loss to the electrodes is the source of the difference in the duration of Stage 2.

To follow up with Stage 1 inefficiencies observed via cavity pressure measurements, the arc power was also analyzed as a function of input energy and electrode gap. These results show that 20% of the stored capacitor energy is lost to parasitic

resistance in circuit components and wires connecting the capacitor bank to the SparkJet. To further analyze efficiency losses, the initial Stage 1 modeling assumptions of an instantaneous and calorically perfect energy deposition were removed. Time-dependent calculations of the corresponding cavity temperature rise showed that an additional 10-25% of the energy losses can be attributed to the extremely high temperatures reached in the cavity. The remaining energy loss is likely due to heat lost to the electrodes. Efficiency as a function of electrode gap was also explored using the pseudo-series triggered circuit which was also designed for improved reliability. Using a maximum trigger voltage of 12 kV, an electrode gap increase from 1.0 mm to 3.0 mm increases the efficiency from 9% to 30%. In summary, the efficiency losses are due primarily to circuit losses, extremely high cavity air temperatures, and heat lost to electrodes.

This dissertation work has presented the development of a 1-D model to simulate the complexities associated with the SparkJet actuator. Through comparison to high-fidelity CFD and experimental results, this 1-D model is well-supported. However, these comparisons have also highlighted some deficiencies in the model which should be addressed in future work.

7.2 Future Work

The area of characterizing the SparkJet actuator and demonstrating the actuator performance in a high-speed flow environment has been explored only over the last 10 years. Due to the high-voltage and high-current nature of the actuator, this

exploration has been slow and there are several avenues for future work.

Related to this dissertation work, shortcomings in the 1-D model related to modeling the arc discharge and heat transfer are of immediate interest for future work. Once these modeling aspects are addressed, the 1-D model can more accurately predict high-frequency performance rather than only modeling trends. Several other areas of future work have been conceived based on the results presented in this dissertation. For example, confidence in the high-frequency modeling, above 100 Hz, would be better supported with experimental high-frequency tests or CFD designed to model sequential SparkJet cycles. Also, the 1-D model comparison exploited differences between the estimation and measurement of the duration of Stage 2. However, future work could be performed to link the duration of Stage 2 to the rollover frequency since Stage 2 measurements are easier to obtain than Stage 3 measurements. Additionally, exploring the possibilities of designing the SparkJet device to take advantage of hydraulic amplification would also be an interesting area for future work. Similarly, exploring the effect of the ratio of the orifice and cavity cross-sectional areas on the jet momentum with attention to orifice edge effects and jet vortex generation. Finally, the high-temperature gas dynamics discussed may also indicate the possibility of non-equilibrium gas effects such that a significant portion of the arc energy is converted to vibrational molecular energy rendering it unusable by the cavity air. Further exploration into the effects of ionized gas phenomena could be beneficial for Stage 1 modeling and estimating inefficiencies.

In the interest of evaluating the SparkJet interaction with a flowfield, expanding the 1-D model to represent actuator performance in the presence of an external

flow would be a valuable tool for design the SparkJet for a particular flow application. To support this model expansion, experimental data to measure the SparkJet cavity pressure and arc power measurements while interacting with an external flow would also be beneficial. Applying the SparkJet actuator to a realistic installation would likely involve a large array of SparkJet actuators. Further expansion of the model to include effects of coupling with nearby SparkJet plumes would help illustrate the effect of actuator orifice spacing and phasing regions of the actuator array to beneficially manipulate an external flowfield.

Finally, the flight conditions of a vehicle poised to benefit from an array of SparkJet actuators would likely operate at high-altitude where low pressures and temperatures exist. Therefore, an evaluation of the actuator performance under tactical conditions would be beneficial. This evaluation could be accomplished using the 1-D model. However, to capture the effects of low-density air on SparkJet reliability and circuit requirements would require experimental evaluation. Also related to testing under tactical conditions is exploration of the effects of environmental challenges such as the presence of dirt, ice, or water on actuator performance and reliability.

Appendix

This appendix contains the MATLAB code used to define and run the 1-D model of the SparkJet cycle. The primary routine is called run_sparkjet_thermal.m and uses the ode45 solver to solve the equations derived in Chapter 3, which are contained in sparkjet_thermal.m. The design parameters for the SparkJet actuator are defined in parameters.m.

```
%*************************************************************
%This is the main function the one-dimensional analytical model,
%which utilizes one of MATLAB's built in ODE solvers (ode45)
%based on explicit Runge-Kutta. See MATLAB %help on ode45 for
%more information. The ODE solver finds the time history of
%cavity pressure, density, and temperature; the velocity of the
%air moving through the orifice of a SparkJet; and the wall
%internal wall temperature.
%
%INPUTS:
%This program only requires access to parameters.m as an input
%and sparkjet_thermal.m for the ode45 solver.
%
%OUTPUTS:
%This program outputs the time-dependent cavity pressure,
%temperature, and density and orifice velocity and momentum.
```

```
%
%Written by Sarah Haack Popkin
%Original version: 11 Dec 2010
%*****************************************************************
clear
clc
close all
format compact

global Ao V Cv Patm vo R Tatm RM Re Rair rhoatm Q eff CM Rout

% Load SparkJet design parameters
[Ao, V, Cv, Patm, vo, R, Tatm, RM, Re, Rair, rhoatm, Q, eff,...
CM, Rout]=parameters;

%Actuation frequency (Hz)
f=1000;
%Initialize steady state power vector
E_ss=zeros(length(f),1);
M_ss=zeros(length(f),1);
%Define Initial Conditions
for k=1:length(f)
```

```
%Define Initial Conditions
rho0=rhoatm;            %Initial density
m=rho0*V;               %Calculate mass inside cavity
U0=1e-5;                %Initial Velocity
T0=Tatm+eff*Q/(m*Cv);   %Initial Temperature
P0=rho0*R*T0;           %Initial Pressure
Tw=Tatm;                %Initial Wall Temperature


freq=f(k);
events=ceil(freq/100);  %Number of times Stage 1 occurs
T=[];                   %Initialize T vector
Y=[];                   %Initialize Y vector
Emax=zeros(events,1);   %Initialize peak power vector
Mmax=zeros(events,1);   %Initialize peak momentum vector
for i=1:events
    %Run ODE solver with (redefined) initial conditions
    options = odeset('RelTol',1e-6,'AbsTol',...
     [1e-6 1e-6 1e-6 1e-6]);
    [t,y]=ode45(@sparkjet_thermal,...
     [(i-1)*(1/freq+1e-9) i*1/freq],[rho0 U0 P0 Tw],options);
    %Build time and variable vectors
    Y(length(Y)+1:length(Y)+length(t),1:4)=y;
    T(length(T)+1:length(T)+length(t),1)=t;
```

```
%Redefine initial conditions for Stage 1 as the final
%conditions in Stage 3
rho0=y(end,1);
T0=y(end,3)/(rho0*R)+eff*Q/(rho0*V*Cv);
P0=rho0*R*T0;
U0=y(end,2);
Tw=y(end,4);
%Find the maximum output power (E/s) during a cycle
Emax(i)=max(y(:,1).*y(:,2)*Ao);
Mmax(i)=max(y(:,1)*vo.*y(:,2));
%Save the max power from the first shot as the reference
%power for a frequency of 1 Hz
if i==1
    Emax1=Emax(i);
    Mmax1=Mmax(i);
elseif abs(Emax(i)-Emax(i-1))<1e-8
    %Save max power once steady state conditions are
    %reached as the state power
    E_ss(k)=(Emax(i)+Emax(i-1))/2;
    M_ss(k)=(Mmax(i)+Mmax(i-1))/2;
    break %Stop if steady state conditions have been achieved
else
```

```
            %Save max power once steady state conditions are
            %reached as the state power
            E_ss(k)=(Emax(i)+Emax(i-1))/2;
            M_ss(k)=(Mmax(i)+Mmax(i-1))/2;
        end
    end
end

P=Y(:,3);       %Pressure
rho=Y(:,1);     %Density
U=Y(:,2);       %Velocity
T=T*1e6;        %Temperature
Mom=rho*vo.*U;  %Momentum

%Append power value for f = 1 Hz actuation
E_ss=[Emax1; E_ss];
M_ss=[Mmax1; M_ss]/Mmax1;
f=[1;f];

%Plot normalized steady-state momentum as a function of frequency
figure
loglog(f,M_ss,'LineWidth',2)
xlabel('Frequency (Hz)','FontSize',24)
```

```
ylabel('Momentum (\muN-s)','FontSize',24)
set(gca,'FontSize',24)

% Plot time history of density, orifice velocity, pressure (kPa)
figure
plot(T,Y(:,1)*1000,'--g','LineWidth',3)
hold on
plot(T,Y(:,2),'--m','LineWidth',3)
plot(T,Y(:,3)/1000,'--b','LineWidth',2)
plot(T,Y(:,3)./(Y(:,1)*R),'--r','LineWidth',3)
xlabel('Time (\mus)','FontSize',24)
ylabel('See Legend','FontSize',24)
set(gca,'FontSize',24)
legend('1-D Density (g/m^3)','1-D Velocity (m/s)',...
'1-D Pressure (kPa)','1-D Temperature (K)')

function dy = sparkjet_thermal(t,y)
%*****************************************************************
%This function defines system of ODEs as given in Chapter 3.
%This is also where the temperature and heat transfer are defined.
The change in boundary conditions are also determined here.
%
%INPUTS
```

```
%           t   -   time (sec)
%           y   -   4x1 vector containing the values of density,
%     velocity, pressure, and wall temperature,
% respectively, with respect to time.
%
%OUTPUTS
%           dy  -   4x1 vector containing the changes in density,
%     velocity, pressure, and wall temperature,
% respectively, with respect to time.
%
% Written by Sarah Haack Popkin
% Original date 11 Dec 2010
%*********************************************************************

global Ao V Cv Patm vo R Tatm RM Re Rair rhoatm CM Rout

dy=zeros(4,1);
%Algebraic Equations
T = y(3)/(y(1)*R);  %Ideal Gas Law

%Simple harmonic oscillator model for thermally perfect gas
Cvt=Cv*(1+(1.4-1)*((5500/1.8/T)^2*exp(5500/1.8/T)/...
(exp(5500/1.8/T)-1)^2));
```

```
%Define pressure boundary condition at orifice between choked and
%unchoked flow
if y(3)>1.893*Patm
    Pe=y(3)/1.893;
elseif y(3)<=1.893*Patm
    Pe=Patm;
end

% Convective heat transfer equation for air only
qdot=(1/Rair*(y(4)-T))/(y(1)*V); %J/(s*kg)

%Differential Equations
if y(2)>0 %Stage 2 Discharge
    %Mass
    dy(1) = -y(1)*y(2)*Ao/V;
    %Momentum
    dy(2) = 1/y(1)*(((y(3)-Pe)*Ao-y(1)*abs(y(2))*y(2)*Ao)/vo-...
     y(2)*dy(1));
    %Energy
    dy(3) = (qdot*y(1)*V-((y(3)-Pe)+y(1)*(Cvt*T+(y(2)^2)/2))*...
     y(2)*Ao-vo* (2*y(1)*y(2)*dy(2) + y(2)^2*dy(1)) ) /...
     (Cvt*V/R);
```

```
elseif y(2)<0 %Stage 3 Refresh

    %Mass

    dy(1) = -rhoatm*y(2)*Ao/V;

    %Momentum

    dy(2) = 1/rhoatm*(((y(3)-Patm)*Ao-rhoatm*abs(y(2))*y(2)*Ao)...

    /vo-y(2)*dy(1));

    %Energy

    dy(3) = (qdot*y(1)*V-((y(3)-Patm)+rhoatm*(Cv*Tatm+(y(2)^2)/2))*...

        y(2)*Ao-vo*(2*rhoatm*y(2)*dy(2)+y(2)^2*dy(1)) )/(Cvt*V/R);

end

%Wall Temperature

dy(4) = 1/CM*((y(4)-Tatm)/(Rout+1/(1/RM+1/Re))-(T-y(4))/Rair);


function [Ao, V, Cv, Patm, vo, R, Tatm, RM, Re, Rair, rhoatm, Q,...

eff, CM, Rout]=parameters

%*********************************************************************

%This function defines the design parameters for the SparkJet.

%

%INPUTS (NA)

%

%OUTPUTS

%           Ao      -   Orifice Area (m^2)

%           V       -   Cavity volume (m^3)
```

```
%           Cv      -   Specific heat of air
%           Patm    -   Atmospheric Pressure (Pa)
%           vo      -   Orifice Volume (m^3)
%           R       -   Specific gas constant for air (J/kg*K)
%           Tatm    -   Atmospheric Temperature (K)
%           RM      -   Thermal Resistance of Macor
%           Re      -   Thermal Resistance of electrodes
%           Rair    -   Thermal Resistance of air inside SparkJet
% cavity
%           rhoatm  -   Atmospheric Density (kg/m^3)
%           Q       -   Capacitor Energy (J)
%           eff     -   Heat transfer efficiency
%           CM      -   Macor Capacitance
%           Rout    -   Thermal Resistance of air outside SparkJet
% cavity
%
% Written by Sarah Haack Popkin
% Original date 11 Dec 2010
%*****************************************************************


R=287.05;               %Specific gas constant for air in J/kg*K
Cp=1004;                %Specific heat of air for constant pressure
Cv=Cp-R;                %Specific heat of air for constant volume
```

```
V=8.484e-8;              %Cavity volume

Tatm=288;                %External flow temperature

Patm=101325;             %External flow pressure

rhoatm=Patm/(Tatm*R);    %External flow density using ideal gas law


Vc=600;                                %Capacitor voltage

C=0.9e-6;                              %Capacitance

eff=1;                                 %Efficiency

%Stage 1 Parameters for Energy Deposition

Q=1/2*C*Vc^2;                          %Energy discharged by spark


%Material properties and geometry


%Electrodes

Dw=0.001;                              %Electrode diameter

rw=Dw/2;                               %Electrode radius

Swc=pi*rw^2;                           %Electrode cross-sectional area


%Orifice

no=1;                                  %Number of Orifices

ro=0.001/2;                            %Orifice radius (m)

Ao=no*pi*ro^2;                         %Orifice area

ho=0.0005;                             %Orifice height
```

```
vo=Ao*ho;                               %Throat volume


%Cavity
hc=(4*V/pi)^(1/3);                      %Cavity height
Acc=pi*(hc/2)^2;                        %Cavity cross-sectional area
dc=hc;                                  %Cavity Diameter
Am=2*Acc+pi*dc*hc-Ao;                   %Cavity internal area


%Outer SparkJet Dimensions
Hout=0.00855;                           %Outer height (m)
Dout=0.01275;                           %Outer diameter (m)
VM=pi*(Dout/2)^2*Hout-V;                %Volume of Macor (m^3)
Aout=2*pi*(Dout/2)^2+2*pi*Dout*Hout;%Outer surface area of Macor (m^3)


%Resistance
%Cavity Air
hin=125;                %Convective heat transfer coefficient(W/m^2*K)
Rair=1/(hin*Am);        %Thermal resistance of air
hout=25;                %Convective heat transfer coefficient(W/m^2*K)
Rout=1/(hout*Aout);     %Convective thermal resistance on outside of
                        %SparkJet walls


%Macor
```

```
k_M=1.46;                          %Thermal conductivity of Macor

Rw=1/(2*pi*hc*k_M)*log(Dout/dc);   %Thermal resistance of Macor Wall

Rb=(Hout-hc)/2/(Acc*k_M);          %Thermal resistance of Macor bottom

Rt=(Hout-hc)/2/((Acc-Ao)*k_M);     %Thermal resistance of Macor top

RM=1/(1/Rw+1/Rb+1/Rt);             %Thermal resistance of Macor

rhoM=2520;                         %Density of Macor (kg/m^3)

C_m=794.95;                        %Specific heat of Macor (J/kg*K)

CM=VM*rhoM*C_m;                    %Capacitance of Macor


%Electrodes

k_e=173;                           %Thermal conductivity of Tungsten

Re=(Hout-hc)/(k_e*Swc);            %Thermal resistance of electrodes
```

Bibliography

[1] Pearcey, H. H., "Some Effects of Shock-induced Separation of Turbulent Boundary Layers in Transonic Flow past Airfoils," Tech. Rep. 3108, Ministry of Aviation, 1959.

[2] Schlichting, H. and Gersten, K., *Boundary Layer Theory, 8th ed.*, Springer, 2000.

[3] Stolz, S., Schlatter, P., and Kleiser, L., "Large-Eddy Simulations of Subharmonic Transition in a Supersonic Boundary Layer," *AIAA Journal*, Vol. 45, No. 5, May 2007.

[4] Rossiter, J., *Wind-tunnel Experiments on the Flow Over Rectangular Cavities at Subsonic and Transonic Speeds*, H.M. Stationery Office, 1967.

[5] Force, U. S. A., "F-22A Raptor," http://www.af.mil/shared/media/photodb/photos/070713-F-0986R-007.jpg, 2007, Online accessed March 2013.

[6] Heller, H. H., Holmes, G., and Covert, E. E., "Flow-Induced Pressure Oscillations in Shallow Cavities," Tech. rep., Air Force Flight Dynamics Laboratory, December 1970, AFFDL-TR-70-104.

[7] Zaman, K. B. M. Q., "Effect of Initial Boundary-Layer State on Subsonic Jet Noise," *AIAA Journal*, Vol. 50, No. 8, 2012.

[8] Viswanathan, K., "Investigation of Noise Source Mechanisms in Subsonic Jets," *AIAA Journal*, Vol. 46, No. 8, August 2008.

[9] Narayanan, S., Barber, T. J., and Polak, D. R., "High Subsonic Jet Experiments: Turbulence and Noise Generation Studies," *AIAA Journal*, Vol. 40, No. 3, March 2002.

[10] Andre, B., Castelain, T., and Bailly, C., "Broadband Shock-Associated Noise in Screeching and Non-Schreeching Underexpanded Supersonic Jets," *AIAA Journal*, Vol. 51, No. 3, March 2013.

[11] Viswanathan, K., Alkislar, M. B., and Czech, M. J., "Characterisitics of the Shock Noise Component of Jet Noise," *AIAA Journal*, Vol. 48, No. 1, January 2010.

[12] Alvi, F. S., Shih, C., Elavarasan, R., Garg, G., and Krothapalli, A., "Control of Supersonic Impinging Jet Flows Using Supersonic Microjets," *AIAA Journal*, Vol. 41, No. 7, July 2003.

[13] Rybalko, M., Babinsky, H., and Loth, E., "Vortex Generators for a Normal Shock/Boundary-Layer Interaction with a Downstream Diffuser," *Journal of Propulsion and Power*, Vol. 28, No. 1, January-February 2012.

[14] Rasheed, A., Hornung, H. G., Federov, A. V., and Malmuth, N. D., "Experiments on Passive Hypervelocity Boundary-Layer Control using an Ultrasonically Absorptive Surface," *AIAA Journal*, Vol. 40, No. 3, March 2002.

[15] Schmit, R. F., Semmelmayer, F., Haverkamp, M., and Grove, J. E., "Examining Passive Flow Control Devices with High Speed Shadowgraph Images around a Mach 1.5 Cavity Flow Field," 6th AIAA Flow Control Conference, June 2012, AIAA 2012-3139.

[16] Chen, F. and Beeler, G. B., "Virtual Shaping of a Two-Dimensional NACA 0015 Airfoil using Synthetic Jet Actuator," 1st AIAA Flow Control Conference, June 2002, AIAA 2002-3273.

[17] Deb, D., Tao, G., Burkholder, J. O., and Smith, D. R., "Adaptive Compensation Control of Synthetic Jet Actuator Arrays for Airfoil Virtual Shaping," *Journal of Aircraft*, Vol. 44, No. 2, March-April 2007.

[18] Shneider, M. N., Macheret, S. O., Zaidi, S. H., Girgis, I., and Miles, R. B., "Virtual Shapes in Supersonic Flow Control with Energy Addition," *Journal of Propulsion and Power*, Vol. 24, No. 5, September-October 2008.

[19] Kumar, R., Botu, A., Ali, Y., Alvi, F. S., and Venkatakrishnan, L., "Virtual Shock Shaping Using Microjet Arrays," 48th AIAA Aerospace Sciences Meeting, January 2010, AIAA 2010-0103.

[20] Zhuang, N., Alvi, F. S., Alkislar, M. B., and Shih, C., "Supersonic Cavity Flows and Their Control," *AIAA Journal*, Vol. 44, No. 9, September 2006.

[21] Bower, W., Kibens, V., Cary, A., Alvi, F., Raman, G., Annaswamy, A., and Malmuth, N., "High-Frequency Excitation Active Flow Control for High-Speed Weapon Release (HIFEX)," 2nd AIAA Flow Control Conference, June-July 2004, AIAA 2004-2513.

[22] Shouman, K., Suplisson, A., Grove, J., and Bower, W., "Supersonic Store Separation at the Holloman High Speed Test Track," Society of Experimental Test Pilots, 2007.

[23] Glezer, A. and Amitay, M., "Synthetic Jets," *Annual Review of Fluid Mechanics*, Vol. 34, January 2002, pp. 503–529.

[24] Topoloski, M., Arora, N., Ali, M., Solomon, J., and Alvi, F., "Experiments on Resonance Enhanced Pulsed Microjet Actuators in Supersonic Crossflow," 6th AIAA Flow Control Conference, June 2012, AIAA 2012-2813.

[25] Strickland, G., Solomon, J., Gustavsson, J., and Alvi, F., "Implementing Resonant Enhanced Pulsed Micro-Actuators for the Control of Supersonic Impinging Jets," 50th AIAA Aerospace Sciences Meeting, January 2012, AIAA 2012-0065.

[26] Solomon, J., Hong, S., Wiley, A., Kumar, R., Annaswamy, A., and Alvi, F., "Control of Supersonic Resonant Flows Using High Bandwidth Micro-Actuators," 15th AIAA/CEAS Aeroacoustics Conference, May 2009, AIAA 2009-3247.

[27] Solomon, J. T., Foster, C., and Alvi, F., "Design and Characterization of High-Bandwidth, Resonance Enhanced Pulsed Microactuators: A Parametric Study," *AIAA Journal*, Vol. 51, No. 2, February 2013.

[28] Crittenden, T. M., Woo, G. T. K., and Glezer, A., "Combustion Powered Actuators for Separation Control," 6th AIAA Flow Control Conference, June 2012, AIAA 2012-3135.

[29] Brzozowski, D. P., Woo, G. T. K., Culp, J. R., and Glezer, A., "Transient Separation Control Using Pulse-Combustion Actuation," *AIAA Journal*, Vol. 48, No. 11, November 2010.

[30] Woo, G. T. K., Glezer, A., Bain, J., Sankar, L., and Crittenden, T. M., "Rotorcraft Fuselage Drag Reduction using Combustion Powered Actuators," 49th AIAA Aerospace Sciences Meeting, January 2011, AIAA 2011-0034.

[31] Corke, T., Enloe, C., and Wilkinson, S., "Dielectric Barrier Discharge Plasma Actuators for Flow Control," *Annual Review of Fluid Mechanics*, Vol. 42, 2010, pp. 505–529.

[32] Roupassov, D., Nikipelov, A., Nudnova, M., and Starikovskii, A., "Flow Separation Control by Plasma Actuator with Nanosecond Pulsed-Periodic Discharge," *AIAA Journal*, Vol. 47, No. 1, January 2009.

[33] Samimy, M., Adamovich, I., Webb, B., Kastner, J., Hileman, J., Keshav, S., and Palm, P., "Development and Application of Localized Arc Filament Plasma Actuators for Jet Flow and Noise Control," 42nd AIAA Aerospace Sciences Meeting, January 2004, AIAA 2004-0184.

[34] Hahn, C., Kearney-Fischer, M., and Samimy, M., "Effects of Ring Groove and Duty Cycle on Plasma Actuator Performance in High Speed Jets," 49th AIAA Aerospace Sciences Meeting, January 2011, AIAA 2011-0977.

[35] Samimy, M., Kim, J., Kastner, J., Adamovich, I., and Utkin, Y., "Active Control of a Mach 0.9 Jet for Noise Mitigation Using Plasma Actuators," *AIAA Journal*, Vol. 45, No. 4, April 2007.

[36] Samimy, M., Kearney-Fischer, M., Kim, J., and Sinha, A., "High-Speed and High-Reynolds-Number Jet Control Using Localized Arc Filament Plasma Actuators," *Journal of Propulsion and Power*, Vol. 28, No. 2, March-April 2012.

[37] Caraballo, E., Webb, N., Little, J., Kim, J., and Samimy, M., "Supersonic Inlet Flow Control Using Plasma Actuators," 47th AIAA Aerospace Sciences Meeting, January 2009, AIAA 2009-0925.

[38] Braun, E., *Electromagnetic Flow Control: A Review and Experimental Development and Testing of a Compact Actuator*, Master's thesis, The University of Texas at Arlington, November 2008.

[39] Nishihara, M., Jiang, N., Rich, J., Lempert, W., I., A., and Gogineni, S., "Low-temperature supersonic boundary layer control using repetitively pulsed magnetohydrodynamic forcing," *Physics of Fluids*, 2005.

[40] Grossman, K. R., Cybyk, B. Z., and VanWie, D. M., "SparkJet Actuators for Flow Control," 41st Aerospace Sciences Meeting and Exhibit, 6-9 January 2003, AIAA 2003-0057.

[41] Reedy, T. M., Kale, N. V., Dutton, J. C., and Elliott, G. S., "Experimental Characterization of a Pulsed Plasma Jet," 50th AIAA Aerospace Sciences Meeting, January 2012, AIAA 2012-0904.

[42] Foster, C. H., Solomon, J. T., and Alvi, F. S., "Visual Study of Resonance Dominated Microjet Flows using Laser-Based Micro-Schlieren," 49th AIAA Aerospace Sciences Meeting, January 2011, AIAA 2011-0766.

[43] Caruana, D., Barricau, P., Hardy, P., Cambronne, J. P., and Belinger, A., "The "Plasma Synthetic Jet" Actuator. Aero-thermodynamic Characterization and first Flow Control Applications," 47th AIAA Aerospace Sciences Meeting, January 2009, AIAA 2009-1307.

[44] Anderson, K. V. and Knight, D. D., "Plasma Jet for Flight Control," *AIAA Journal*, Vol. 50, No. 9, September 2012.

[45] Cybyk, B. Z., Wilkerson, J. T., and Grossman, K. R., "Performance Characteristics of the SparkJet Flow Control Actuator," 2nd AIAA Flow Control Conference, June 2004, AIAA 2004-2131.

[46] Taylor, T. M. and Cybyk, B. Z., "High-Fidelity Modeling of Micro-Scale Flow-Control Devices with Applications to the Macro-Scale Environment," 15th AIAA International Space Planes and Sypersonic Systems and Technologies Conference, April 2008, AIAA 2008-2608.

[47] Anderson, K. and Knight, D., "Characterization of Single Pulse of Plasma Jet," 50th AIAA Aerospace Sciences Meeting, January 2012, AIAA 2012-0188.

[48] Quint, G., Rogier, F., and Dufour, G., "Numerical Modeling of the Electric Arc Created Inside the Cavity of the PSJ Actuator," 20th AIAA Computational Fluid Dynamics Conference, June 2011, AIAA 2011-3394.

[49] Cybyk, B. Z., Simon, D. H., Land III, H. B., Chen, J., and Katz, J., "Experimental Characterization of Supersonic Flow Control Actuator," 44th AIAA Aerospace Sciences Meeting, January 2006, AIAA 2006-0478.

[50] Haack, S. J., Land III, H. B., Cybyk, B. Z., Ko, H. S., and Katz, J., "Characterization of a High-Speed Flow Control Actuator Using Digital Speckle Tomography and PIV," 4th AIAA Flow Control Conference, June 2008, AIAA 2008-3759.

[51] Narayanaswamy, V., *Investigation of a pulsed-plasma jet for separation shock boundary layer interaction control*, Ph.D. thesis, University of Texas at Austin, August 2010.

[52] Ostman, R. J., Herges, T. G., Dutton, J. C., and Elliott, G. S., "Effect on High-Speed Boundary-Layer Characteristics from Plasma Actuators," 51st AIAA Aerospace Sciences Meeting, January 2013, AIAA 2013-0527.

[53] Hardy, P., Barricau, P., Belinger, A., Caruana, D., Cambronne, J., and Gleyzes, C., "Plasma Synthetic Jet for Flow Control," 40th AIAA Fluid Dynamics Conference, June 2010, AIAA 2010-5103.

[54] Golbabaei-Asl, M., Knight, D., Anderson, K., and Wilkinson, S., "SparkJet Efficiency," 51st AIAA Aerospace Sciences Meeting, January 2013, AIAA 2013-0928.

[55] Haack, S., Taylor, T., Emhoff, J., and Cybyk, B., "Development of an Analytical SparkJet Model," 5th AIAA Flow Control Conference, June 2010, AIAA 2010-4979.

[56] Roth, W., Guest, P. G., von Elbe, G., and Lewis, B., "Heat Generation by Electric Sparks and Rate of Heat Loss to the Spark Electrodes," *The Journal of Chemical Physics*, Vol. 19, No. 12, December 1951.

[57] John D. Anderson, J., *Fundamentals of Aerodynamics, 3rd ed.*, McGraw Hill, 2001.

[58] Raizer, Y. P., *Gas Discharge Physics*, Springer-Verlag, 1st ed., 1991.

[59] Ekici, O., Ezekoye, O. A., Hall, M. J., and Matthews, R. D., "Thermal and Flow Fields Modeling of Fast Spark Discharges in Air," *Journal of Fluids Engineering*, Vol. 129, 2007, pp. 55–65.

[60] Haack, S. J. and Foster, C. H., "Experimental Estimation of SparkJet Efficiency," 42nd AIAA Plasmadynamics and Lasers Conference, June 2011, AIAA 2011-3997.

[61] Laboratories, A. K., "Trigger Transformers," http://amglo.com/trigger_transformers.html, 2013, Online accessed July 2013.

[62] Optoelectronics, P. E., "High Performance Flash and Arc Lamps," http://laser-caltech.web.cern.ch/laser-caltech/report/Flash%20lamp%20Eg&G.pdf, 2013, Online accessed July 2013.

[63] Narayanaswamy, V., Laxminarayan, R., and Clemens, N., "Characterization of a High-Frequency Pulsed-Plasma Jet Actuator for Supersonic Flow Control," *AIAA Journal*, Vol. 48, No. 2, 2010, pp. 297–305.

[64] Staff, A. R., "Equations, Tables, and Charts for Compressible Flow," Tech. Rep. 1135, National Advisory Committee for Aeronautics, 1953.

[65] Edwards, D. K., Denny, V. E., and Mills, A. F., *Transfer Processes*, Hemisphere, 2nd ed., 1979.

[66] Bourlos, M. I., Fauchais, P., and Pfender, E., *Thermal Plasmas: Fundamentals and Applications*, Plenum Press, 1994.